UNIVERSIDAD AUTONOMA DE MADRID

Facultad de Ciencias

Departamento de Física de Materiales

# Optical Study of Semiconductor Nanostructures: from material properties to quantum optics

## PhD Thesis

**EVA Mª GALLARDO VELASCO**

Dissertation submitted for the degree of Doctor of Philosophy
at Universidad Autónoma de Madrid

Madrid, 2010

UNIVERSIDAD AUTONOMA DE MADRID

Facultad de Ciencias

Departamento de Física de Materiales

# Optical Study of Semiconductor Nanostructures: from material properties to quantum optics

## PhD Thesis

Presentada por:

Eva Mª Gallardo Velasco

Licenciada en Ciencias Físicas

Director:

José Manuel Calleja Pardo

Catedrático de Universidad

Madrid, 2010

*A mis padres*

*"La alegría está en la lucha, en el esfuerzo, en el sufrimiento que supone la lucha, y no en la victoria misma."*

Mahatma Gandhi

# Agradecimientos

Después de tanto tiempo de esfuerzo y dedicación, llega el grato momento de agradecer a todos aquellos que de un modo u otro han contribuido a que este trabajo haya sido posible.

En primer lugar, me gustaría expresar mi más sincero agradecimiento al Prof. José Manuel Calleja por haber sido mi director de Tesis, por haberme guiado y enseñado tanto durante este largo tiempo, y también por su paciencia y sus consejos en mis momentos de dudas, que no fueron pocos.

También me gustaría agradecer a los Profesores Herko van der Meulen, Luis Viña y Carlos Tejedor por toda su ayuda y enseñanza durante el desarrollo de mi Tesis. Muchas gracias igualmente a mis compañeros de laboratorio: Sne, Dipankar y Ania, que se convertieron en mucho más que eso y de los que también he aprendido mucho.

He de dar las gracias también a todos los co-autores que han participado en el trabajo presentado en esta Tesis: a Luis Javier Martínez y Pablo Aitor Postigo del Instituto de Microelectrónica de Madrid (CSIC) y a Javier Grandal, Miguel Ángel Sánchez García y Enrique Calleja del Instituto de Sistemas Optoelectrónicos y Microelectrónica (ISOM) de la Universidad Politécnica de Madrid, junto con todos sus colaboradores, que han aportado sus muestras y han ayudado significativamente al desarrollo de este trabajo con fructíferas discusiones. Gracias también al Dr. Fernando Agulló-Rueda por su colaboración en las medidas Raman.

I also would like to thank the groups I had the opportunity to visit and to collaborate with: to Richard Noetzel from Eindhoven University of Technology and to Achim Trampert and Esperanza Luna from Paul Drude Institute in Berlin.

Muchas gracias también a todas las personas que han ido pasando por el departamento y con las he compartido muy buenos momentos: Lola, Javi, Olga, Iván, Susana, Juancho, José Luis, Carlos, Alberto, Dario, Daniele, Guilherme, Jorge, Marta, Emma, Mariano, Maysoun, Nina, … También a David, por esas conversaciones durante las comidas en las que me intentaba solucionar la vida.

A todas mis compañeras y amigas balonmaneras (aunque en femenino, para no perder la costumbre también incluye a algunos chicos), con las que he aprendido lo importante que es el trabajo en equipo y a las que les agradezco el apoyo y la amistad que me han dado siempre. Debo una especial mención para Irene, Patri y Vero, que algunas llevan

ahí literalmente toda una vida, porque espero que sepan lo mucho que significan para mí.

Resulta difícil expresar con palabras el especial agradecimiento que le debo a Carlos. Quería darte las gracias por todo el apoyo y amor que me has demostrado todo este tiempo. Por quererme, por ayudarme, por tu compañía, por mantener mi ilusión, por hacerme creer en mí, en definitiva, por estar ahí siempre. Sin ti este camino no sería lo mismo.

Finalmente, me gustaría expresar mi más profunda gratitud a mi familia. A mis padres, a los cuales les debo lo que soy, que con su ejemplo me enseñaron a valorar las cosas importantes de la vida y a comprender que todo esfuerzo tiene su recompensa. A mis hermanos, Alex, Mayte, Rubén y Virginia, por demostrarme siempre todo su cariño y cuidarme como los hermanos mayores modelo que son. A mis cuñados, Carlos, Yoli, Esther y Luis, con los que siempre he podido contar. Debo hacer una alusión especial a Carlos, y también un poquito a Alex, que durante este tiempo me han ayudado a llevar mejor los madrugones. A mis sobrinos, Rubén, Alejandro, Aitana, Carolina, Alba, Álvaro, Adriana, Pablo, Rodrigo, Quique y el pequeño Diego, porque cada día me sacan una sonrisa. A todos, muchas gracias, porque hacéis que me sienta orgullosa de mi familia.

# Introducción y Objetivos

El desarrollo de sistemas semiconductores de baja dimensionalidad en los últimos años ha sido de gran importancia para el avance de la ciencia así como para las aplicaciones en las nuevas tecnologías. Gracias a estos sistemas se ha avanzado notablemente en los ámbitos de la interacción luz-materia y del procesado de información cuántica. Entre las aplicaciones más interesantes de estos sistemas se encuentran la fabricación de láseres, detectores y fuentes de fotones individuales.

Unos de estos sistemas de baja dimensionalidad más ampliamente estudiado son los llamados *puntos cuánticos* (PCs), en los que el confinamiento en las tres direcciones del espacio los hace comportarse como átomos en muchos aspectos. Su principal característica es la cuantización de los estados electrónicos en un sistema de niveles discretos [1-3]. Como resultado de dicha cuantización, este tipo de confinamiento se caracteriza por líneas de emisión estrechas y largos tiempos de relajación. Por esta razón, se han convertido en elementos esenciales para el desarrollo de fuentes de fotones individuales y de los llamados *qubits*, que constituyen los elementos básicos para el manejo de información cuántica. La mayor parte de los estudios se han concentrado en PCs de In(Ga)As rodeados de una red GaAs. La demostración de emisión de fotones individuales en otros sistemas de baja dimensionalidad como los *anillos cuánticos* [4] ha abierto las puertas a nuevas posibilidades en el diseño de este tipo de fuentes. Estas estructuras, además de tener un esquema de niveles electrónicos análogo al de los PCs, presentan nuevas propiedades consecuencia de su forma anular, como efectos Aharonov-Bohm en forma de corrientes oscilatorias constantes [5, 6], que los convierte en sistemas muy interesantes.

Para obtener fuentes de luz eficientes, los PCs habitualmente se sitúan embebidos en microcavidades ópticas. De este modo, estos sistemas se han convertido en elementos fundamentales en la investigación de le Electrodinámica Cuántica en cavidades de estado sólido, que estudia la interacción entre un emisor de fotones y el campo electromagnético de la cavidad [7-11]. Esta interacción luz-materia presenta diferentes ventajas de cara a las posibles aplicaciones dependiendo de la intensidad del acoplamiento [12]. En régimen de acoplamiento débil, se puede obtener un aumento significativo del ritmo de emisión espontánea del PC (efecto Purcell) cuando se sintonizan los modos de la cavidad (MCs) dentro y fuera de resonancia con el emisor [13, 14]. En el régimen de acoplamiento fuerte, la emisión espontánea, que es

usualmente un proceso irreversible, pasa a ser un intercambio reversible de energía entre el emisor y el MC [15]. En los últimos años se ha demostrado experimentalmente el acoplamiento fuerte en sistemas PC-cavidad [15-17]. Los estados enlazados luz-materia de estos sistemas pueden proporcionar la base (*qubits*) para las futuras aplicaciones en el procesado de información cuántica, que requiere interacciones rápidas y de larga distancia entre diferentes *qubits*. La posibilidad de acoplar dos o más *qubits* mediante la misma microcavidad óptica constituye la operación básica en la transmisión de información cuántica. La física de dos qubits no acoplados directamente pero acoplados al mismo MC ha sido descrita ya teoréticamente [18, 19]. Sin embargo, los principales problemas se encuentran en la obtención experimental de esta interacción entre PCs. Se han propuesto algunos sistemas basados en la fabricación selectiva de la microcavidad alrededor de los PCs de interés [20, 21]. Un paso más hacia las aplicaciones se podría obtener con la fabricación de dos o más microcavidades acopladas entre sí que presenten MC acoplados y deslocalizados sobre toda la estructura [22, 23].

Recientemente, los PCs también se han propuesto como fuentes de pares de fotones enlazados debido a la emisión en cascada de los dos fotones que resultan de la recombinación de los estados biexcitón y excitón [24]. Sin embargo, su eficiencia está limitada por el desdoblamiento de estructura fina de estas transiciones debido a las asimetrías en los PCs, que provocan la separación espectral de las dos transiciones lineal y perpendicularmente polarizadas del excitón [25]. El control de la polarización de los fotones emitidos resulta entonces una tarea fundamental para la fabricación a demanda de fuentes de fotones individuales y enlazados. Por ejemplo, en criptografía cuántica [26] o en computación cuántica en óptica lineal [27], la polarización es a menudo usada para codificar la información de los *qubits*. De este modo, los PCs embebidos en microcavidades ópticas resultan adecuados también para el estudio de la influencia que tiene el MC en la polarización de la emisión del PC [28-31].

Otros materiales que han despertado mucho interés en los últimos años son los semiconductores basados en nitruros del grupo III. Los compuestos de (Al, Ga, In)N y sus aleaciones ternarias proporcionan un rango continuo de energía desde el infrarrojo cercano del InN, cuya energía del *gap* (ancho de banda prohibida) es de 0.7 eV, hasta el ultravioleta profundo del AlN (energía del *gap* de 6.2 eV), a diferencia de los dispositivos basados en GaAs que operan a longitudes de onda largas del rango del espectro visible. Su amplio rango de energía y su *gap* directo hacen de los nitruros candidatos ideales para la fabricación de dispositivos optoelectrónicos de alta temperatura. Entre ellos, el InN es el menos conocido debido a la dificultad de crecimiento de estructuras de alta calidad [32-34], por lo que su estudio despierta un gran interés. Una de sus propiedades más interesantes es la presencia de una capa de acumulación de electrones en la superficie, incluso en muestras no dopadas, que ha

impedido hasta hace poco la determinación del *gap* de energía del InN [35]. Esta acumulación de electrones ha sido observada en superficies polares y no polares del InN [36] y su origen es aún objeto de debate. Como esta propiedad del InN constituye principalmente una desventaja de cara a las futuras aplicaciones, un conocimiento más profundo de su origen y propiedades permitirá establecer posibles métodos para controlarla.

Los sistemas de baja dimensionalidad basados en los nitruros del grupo III también son interesantes por sus posibles aplicaciones. En particular, las nanocolumnas (NCs) verticalmente alineadas pueden ser crecidas mediante epitaxia de haces moleculares asistida por plasma en condiciones ricas en N [32-34, 37]. La morfología columnar favorece la relajación lateral minimizando así la tensión y los defectos estructurales en comparación con el material en volumen. De este modo, la alta calidad cristalina de las muestras de NCs las convierte en candidatos perfectos para el estudio de las propiedades fundamentales del InN, así como para la fabricación de dispositivos de mayor calidad. Además, la alta relación superficie/volumen de estas nanoestructuras da lugar a una alta eficiencia en la extracción de luz, que de nuevo va a favor de su uso en dispositivos optoelectrónicos. Recientemente, se han obtenido estructuras ordenadas de NCs de GaN mediante la técnica de crecimiento en área selectiva [38]. Además, la posibilidad de fabricar NCs con una estructura periódica [39] dará lugar al desarrollo de cavidades en forma de micropilares sin necesidad de litografía. En particular, ya se han fabricado diodos emisores de luz (LEDs) basados en NCs con discos cuánticos de InGaN en GaN [40].

En esta Tesis se investigan las propiedades ópticas de dos sistemas basados en nanoestructuras semiconductoras: anillos cuánticos de InAs/GaAs embebidos en microcavidades de cristal fotónico y nanocolumnas de InN. Para ello se han usado diferentes técnicas experimentales como fotoluminiscencia (PL), excitación de la fotoluminiscencia (PLE), correlación de fotones y espectroscopía Raman. En relación a los anillos cuánticos de InAs, los objetivos de este trabajo son el estudio de la emisión de anillos individuales, sus propiedades como emisores de fotones individuales y la interacción luz-materia en los sistemas anillo-cavidad. En lo que respecta a las NCs de InN, la investigación se ha centrado en la capa de acumulación de electrones en las superficies no polares de las mismas.

La Tesis está organizada de la siguiente manera:

El Capítulo 2 proporciona una amplia introducción sobre las propiedades fundamentales de las nanoestructuras investigadas en este trabajo, el sistema anillo cuántico de InAs/GaAs-cavidad (sección 2.1) y las nanocolumnas de InN (sección 2.2).

La descripción incluye también una visión general sobre el trabajo ya hecho en estas áreas.

El Capítulo 3 describe las técnicas experimentales usadas para la investigación de ambos sistemas, así como los detalles de los montajes experimentales.

Los dos siguientes capítulos están dedicados a los principales resultados experimentales obtenidos en este trabajo:

El Capítulo 4 se centra en el estudio de las propiedades ópticas de los anillos cuánticos de InAs/GaAs embebidos en un microcavidad de cristal fotónico. En primer lugar, se ha demostrado la emisión de fotones individuales en estos anillos mediante medidas de correlación de fotones. Después, se ha investigado el acoplamiento entre anillo y cavidad por medio de medidas de PL y PL resuelta en tiempo. Por último, se ha demostrado el acoplamiento mediado por la cavidad entre dos anillos cuánticos espacialmente distantes con medidas de PLE.

El Capítulo 5 presenta resultados obtenidos mediante espectroscopía Raman de las propiedades vibracionales de NCs de InN crecidas con diferentes orientaciones. La investigación se ha centrado en el acoplamiento del fonón longitudinal óptico con el plasmón en las capas superficiales de acumulación de electrones. La estructura de esta capa de acumulación se ha investigado también mediante microscopía electrónica de transmisión de alta resolución (HR-TEM).

Finalmente, las principales conclusiones de esta Tesis se recogen en el Capítulo 6.

# Conclusiones

Las conclusiones generales de este trabajo se presentan a continuación. Están clasificadas en dos grupos, correspondientes a los dos sistemas físicos investigados.

**1. Anillos cuánticos de InAs/GaAs embebidos en una microcavidad de cristal fotónico**

1.1. Se ha demostrado la emisión de fotones individuales en anillos cuánticos de InAs mediante medidas, con excitación continua, de autocorrelación y correlación cruzada de las transiciones del excitón (X) y biexcitón (XX). A tiempo de retardo nulo, se han encontrado valores por debajo de 0.5 en las funciones de autocorrelación del X y del XX. La correlación cruzada indica emisión secuencial de fotones desde el estado del biexcitón al del excitón y de éste al estado fundamental.

1.2. Para intensidades de emisión similares, las funciones de correlación de segundo orden presentan tiempos de subida característicos más largos para la emisión del excitón que para la del biexcitón. A alta potencia de excitación, se espera que la probabilidad de emitir dos fotones consecutivos desde el XX con un tiempo de retardo corto sea mayor que desde el X, como resultado del rápido tiempo de recarga.

1.3. Se ha demostrado el acoplamiento individual de dos anillos cuánticos, separados 1.4 μm, con el modo de resonancia de una microcavidad de cristal fotónico del tipo H1 *calzone* mediante el aumento de la intensidad de emisión y la disminución en el tiempo de vida (efecto Purcell) de los anillos cuando disminuye la diferencia entre las energías de emisión de anillo y MC (*detuning*). El acoplamiento simultáneo de ambos anillos a la misma cavidad ha sido probado por la observación del efecto Purcell en ambos anillos a la vez. Se han estimado valores de 30 μeV para las fuerzas de acoplamiento individuales a partir de la modificación observada en el ritmo de emisión espontánea. Se ha determinado el régimen de acoplamiento débil en ambos casos al comparar estos valores con las anchuras de línea de los anillos y del MC.

1.4. Se ha presentado evidencia experimental del control del ángulo de la polarización lineal en la emisión de uno de los anillos cuánticos acoplado a la

cavidad al variar el *detuning*. La polarización lineal rota de manera continua desde casi perpendicular a *detuning* grande, a paralela a la del MC a cero *detuning*. Además, el ángulo de polarización de la emisión del anillo con respecto a la polarización del MC cambia su signo para *detuning* negativo, lo que es explicado cualitativamente en términos de hibridación de los estados del anillo y la cavidad. Este resultado confirma que la mezcla de estados en régimen de acoplamiento débil puede demostrarse a través de la polarización de los fotones emitidos.

1.5. Se ha encontrado un comportamiento diferente para otro anillo cuántico, que mantiene su polarización lineal paralela a la del MC para todos los valores del *detuning*. La diferencia entre estos comportamientos parece deberse a la posición exacta de cada anillo con respecto al centro de la cavidad y a las orientaciones intrínsecas de sus dipolos.

1.6. Mediante medidas de PLE, se ha demostrado un acoplamiento efectivo entre los dos anillos mencionados en los puntos anteriores mediado por el MC. La interacción se ha probado por el aumento en la intensidad de emisión de cada anillo cuando se excita resonantemente en el estado excitado del otro. Se ha obtenido un valor aproximado de 2 μeV para la fuerza de acoplamiento entre los dos anillos.

1.7. El mecanismo más probable de interacción entre los dos anillos implica un acoplamiento coherente de sus estados *s* mediado por la cavidad, pues las dos contribuciones a la emisión de cada anillo (excitando en su estado *p* o en el estado *p* del otro) saturan de una manera similar al aumentar la potencia de excitación.

## 2. Nanocolumnas de InN

2.1. Nanocolumnas de InN crecidas dobre diferentes sustratos (Si(111), Si(001) y GaN $(11\bar{2}0)$ ) y con diferentes orientaciones han sido caracterizadas mediante el esparcimiento inelástico de la luz. Su alta calidad cristalina se ha probado en todos los casos por el estrecho modo $E_2$ observado.

2.2. La dependencia de las intensidades de los distintos modos Raman con las configuraciones utilizadas se explica asumiendo que la luz en el interior de las NCs se propaga prácticamente perpendicular a la dirección de crecimiento incluso cuando la dirección nominal de esparcimiento se elige paralela a la misma. Para ello se han comparado los modos de vibración observados en los espectros Raman de muestras compactas con los observados en muestras de NCs.

2.3. Se ha demostrado la presencia de una capa de acumulación de electrones en las superficies laterales no polares de las NCs de InN crecidas sobre sustratos de silicio por la aparición del modo $L^-$, el modo acoplado fonón $E_1$(LO)-plasmón. La

concentración de electrones se puede estimar a partir de la frecuencia del modo acoplado $L^-$.

2.4. Se ha observado que la intensidad del modo $L^-$, que se origina en la capa superficial, comparada con la del fonón no acoplado $E_1$(LO), que viene de la parte interna de las NCs, aumenta como la cuarta potencia de la energía de excitación. Este resultado evidencia el intenso esparcimiento elástico que se produce en la muestras de NCs.

2.5. El cociente de intensidades $L^-/E_1$(LO) también depende del diámetro promedio de las NCs. Dicho cociente decrece cuando el diámetro de las NCs aumenta para una longitud de onda de excitación de 632.8 nm. Sin embargo, se observa la tendencia opuesta cuando se excita con 514.5 o 457.9 nm. Estas diferentes dependencias se pueden explicar cualitativamente mediante la competencia de dos efectos, la proporción entre superficie y volumen y el esparcimiento elástico dependiente de la longitud de onda.

2.6. Se ha desarrollado un nuevo método de preparación de muestras para HR-TEM para la toma de imágenes en vista planar de las muestras de NCs. Se ha observado una capa de $In_2O_3$ de unos pocos nanometros de grosor alrededor de las NCs de InN crecidas sobre sustratos de silicio. La densidad superficial de electrones se ve afectada por esta capa.

2.7. La concentración de electrones en la superficie de las NCs varía al realizar un ataque químico. Mediante la inmersión de las NCs de InN en ácido HCl, la capa de $In_2O_3$ se elimina y la densidad de electrones aumenta como resultado de la mayor curvatura de las bandas en las superficies de InN que en las de $In_2O_3$. La posterior oxidación de la superficie da lugar de nuevo a la disminución de la concentración de electrones.

2.8. Los principales ejes cristalográficos de las NCs de InN crecidas sobre sustratos plano *a* de GaN han sido determinados mediante los espectros Raman dependientes de la polarización, confirmándose en las NCs la misma orientación que en el sustrato.

# Contents

# Abbreviations

| | |
|---|---|
| APD | avalanche photodiode |
| AFM | atomic force microscopy |
| BS | beamsplitter |
| BZ | Brillouin zone |
| CB(M) | conduction band (minimum) |
| CCD | charged-coupled device |
| CM | cavity mode |
| cQED | cavity Quantum Electrodynamics |
| EAL | electron accumulation layer |
| *e-h* | electron-hole |
| FSS | fine structure splitting |
| FWHM | full width at half maximum |
| HBT | Hanbury-Brown and Twiss |
| HR-TEM | high-resolution transmission electron microscopy |
| IRF | instrumental response function |
| LO | longitudinal optical |
| LT | low temperature |
| MBE | molecular beam epitaxy |
| MCA | multichannel analyzer |
| NC | nanocolumn |
| PC | photonic crystal |
| PL | photoluminescence |
| PLE | excitation photoluminescence |
| PV-TEM | plan-view transmission electron microscopy |
| PZ | piezoelectric |
| RT | room temperature |
| QD | quantum dot |

| | |
|---|---|
| QR | quantum ring |
| SAED | selected area electron diffraction |
| SE | spontaneous emission |
| SEM | scanning electron microscopy |
| SNR | signal to noise ratio |
| SPE | single photon emission/emitter |
| TAC | time-to-amplitude converter |
| TCSPC | time-correlated single-photon counting |
| TEM | transmission electron microscopy |
| TO | transverse optical |
| VB(M) | valence band (maximum) |
| WL | wetting layer |
| X | exciton |
| XX | biexciton |
| $X^+$ | positive trion |
| $X^-$ | negative trion |
| X-TEM | cross-sectional transmission electron microscopy |
| ZPL | zero phonon line |

# List of Figures

# List of Tables

# Chapter 1

# Introduction and Objectives

The recent development of low-dimensional semiconductor systems has been of great importance in the advancement of science as well as in the new technologic applications. They have allowed significant progress of knowledge in the fields of light-matter interaction and quantum information manipulation. The fabrication of lasers, detectors and single photon sources are among the most interesting applications based on these systems.

One of these low-dimensional systems most widely investigated are the so-called *quantum dots* (QDs), where the spatial confinement in the three space directions makes them behave in many ways like atoms. Their main characteristic is the quantization of the electronic states in a discrete level set, as in atomic physics [1-3]. As a result of this quantization, narrow emission lines and long relaxation times are fingerprints of 3D confinement. For this reason they have become essential elements for the development of single photon sources and qubits, which are essential components for quantum information handling. Most of the studies have concentrated on In(Ga)As QDs surrounded by a GaAs matrix. The demonstration of single photon emission also in other zero-dimensional systems as *quantum rings* (QRs) [4] has opened new possibilities in the design of single photon sources. Apart from their analogous electronic level scheme to QDs, they present new properties, consequence of their ring-like shape, as Aharonov-Bohm effects in the form of oscillatory persistent currents [5, 6], which make them very interesting systems.

In order to achieve an efficient light source, the QDs are usually embedded in optical microcavities. These systems are the fundamental elements in the investigation of solid-state *cavity Quantum Electrodynamics* (cQED), which studies the interaction between the emitter and the electromagnetic field of the cavity [7-11]. This light-matter interaction presents different advantages depending on the strength of the coupling in

view of the possible applications [12]. In the weak coupling regime, a significant enhancement of the spontaneous emission rate of the QD (Purcell effect) can be obtained by tuning the discrete *cavity modes* (CMs) in and out of resonance with the emitter [13, 14]. In the strong coupling regime, the usual irreversible spontaneous emission changes to a reversible energy exchange between the emitter and the cavity mode [15]. Strong coupling has been experimentally demonstrated in the past years in QD-cavity systems [15-17]. The entangled light-matter states in these systems can provide the basis (*qubits*) for future applications in quantum information processing, in which fast and long distance interactions between semiconductor qubits are needed. The possibility of coupling two or more qubits through the same optical microcavity constitutes the basic operation of the quantum information transmission. The physics of two qubits with no direct coupling but coupled to the same CM has already been described theoretically [18, 19]. However, the main problem is found in the experimental realization of this QD-QD interaction. Some proposals have been given based on the deterministic location of the QDs inside the cavity [20, 21]. Further implementation could be obtained by the fabrication of two or more coupled microcavities which exhibit delocalized coupled-CMs over the whole array [22, 23].

Recently, semiconductor QDs have emerged also as attractive sources of entangled photon pairs through the cascade emission of two photons as a result of the recombination from the biexciton and exciton states [24]. However, their efficiency is limited by the fine structure splitting of exciton transitions due to the QD asymmetry, which spectrally separates the orthogonally linearly polarized exciton and biexciton transitions [25]. The control of the polarization of the emitted photons is then essential for the implementation of the "on demand" single and entangled photon sources. For example, in quantum cryptography [26] or linear optics quantum computing [27], polarization is often used to encode the qubit information. In this way, QDs embedded in optical microcavities have become very interesting systems also due to the demonstrated influence of the cavity mode in the polarization of the QD emission [28-31].

Other materials that have attracted much attention in the last few years are the group-III-nitride-based semiconductors. The (Al, Ga, In)N compounds and their ternary alloys provide a continuous energy range from the near infrared of the InN band gap (0.7 eV) to the deep ultraviolet of AlN (6.2 eV), in contrast to GaAs-based devices which are restricted to the long-wavelength part of the visible spectral range. Their wide energy range and their direct bandgap character make them ideal candidates for efficient optoelectronic devices operating at high temperatures. Among them, InN is the worst known compound due to the difficulty in growing high quality crystals [32-34], so that its study is of great interest. One of its most interesting properties is the presence of an

*electron accumulation layer* (EAL) at the surface, even in undoped samples, which has prevented until recently the determination of the InN bandgap energy [35]. This EAL has been observed in polar and non-polar InN surfaces [36] and its origin is still object of debate. As this InN property constitutes mainly a disadvantage in view of the future applications, a deeper knowledge of its origin and properties is desirable in order to establish possible methods to control it.

The low-dimensional systems based on group-III nitrides are also of great interest due to their potential applications. In particular, the vertically self-aligned group-III nitride *nanocolumns* (NCs) have been successfully grown by plasma-assisted molecular beam epitaxy (MBE) under N-rich conditions [32-34, 37]. The columnar morphology favours the lateral elastic relaxation which minimizes the strain and structural defects in comparison to bulk crystals. Therefore, the high quality of columnar samples makes them perfect candidates for the fabrication of superior devices and for the study of InN fundamental properties. Besides, the large surface-to-volume ratio of these nanostructures results in a high light-extraction efficiency which favours their use in optoelectronic devices. Recently, ordered arrays of GaN NCs have been obtained by the selective-area growth technique [38]. Moreover, the possibility to fabricate the NCs with a periodic structure [39] has triggered the development of micro-pillar cavities without etching. In fact, InGaN/GaN NC light emitting diodes (LEDs) with InGaN multiple quantum disks have already been fabricated [40].

The scope of this Thesis is the investigation of the optical properties of two systems based on semiconductor nanostructures: InAs/GaAs quantum rings embedded in photonic crystal microcavities and InN nanocolumns. For this purpose, different experimental techniques have been used, in particular photoluminescence (PL) spectroscopy and its excitation (PLE), photon correlation measurements and Raman scattering. Regarding the InAs QRs, the aims of this work are the study of the emission of single QRs, their properties as single photon emitters and the light-matter interaction in the QR-CM systems. In relation to the InN NCs, the investigation has been focused on the electron accumulation at the lateral non-polar surfaces of the NCs.

This Thesis is organized as follows:

Chapter 2 provides a broad introduction to the fundamental properties of the semiconductor nanostructures investigated in this work, InAs/GaAs quantum ring-cavity system (Section 2.1) and InN nanocolumns (Section 2.2). The descriptions include also an overview of the work already done in these areas.

Chapter 3 describes the experimental techniques used for the investigation of both QR-cavity system and InN NCs, as well as the details of the experimental setups.

The following two chapters are dedicated to the main experimental results of this work and their analysis:

Chapter 4 is devoted to the study of the optical properties of InAs/GaAs QRs embedded in a PC microcavity. First, the QRs are demonstrated to have characteristics of single photon emitters by photon correlation measurements. Then, QR-cavity coupling is investigated by photoluminescence and time resolved measurements. Furthermore, the coupling, mediated by the cavity, between two distant QRs is demonstrated by photoluminescence excitation spectroscopy.

Chapter 5 presents results on the vibrational properties of InN NCs grown with different orientations obtained by Raman scattering. The investigation has been focused on the longitudinal optical (LO) phonon-plasmon coupling in surface electron accumulation layers. The structure of this accumulation layer has been investigated also by high resolution-transmission electron microscopy (HR-TEM).

Finally, the main conclusions of this Thesis are collected in Chapter 6.

# Chapter 2

# General Properties and State of the Art

The understanding of the experimental results presented in this Thesis requires the basic knowledge of the fundamental properties of the studied systems and the work done previously. The aim of this chapter is to provide an introduction of the different topics and systems studied in this Thesis. In Section 2.1 we will focus on the light-matter interaction in a quantum dot-cavity system, while the description of the InN nanocolumn properties will be given in Section 2.2.

## 2.1. Quantum dots in an optical cavity: solid state cavity Quantum Electrodynamics

Solid state cavity Quantum Electrodynamics effects can be studied in a single self-assembled quantum dot (QD) coupled to a resonant mode of an optical microcavity. The purpose of this section is to give an introduction to the basic properties of the systems involved and to present an overview of the work already done in this topic. It will start in Sections 2.1.1 and 2.1.2 with the description of the emitter part (self-assembled QDs) and the cavity part (photonic crystal microcavities). Section 2.1.3 will be focused on the light-matter interaction on microcavities. Finally, in Section 2.1.4 a brief description of the physics of two single QDs coupled to the same cavity mode is given.

### 2.1.1. Zero-dimensional nanostructures

Quantum dots are quasi-zero dimensional semiconductor structures where the wavefunction of the electrons is confined in the three dimensions due to the potential energy barriers created at the QD boundaries [1, 2]. As a result of the strong confinement imposed in all three spatial dimensions, QDs are, to some extent, similar to

atoms and therefore are frequently referred to as *artificial atoms*. What makes them especially attractive is the possibility of controlling their energy level structure through their size and shape.

Among the various fabrication techniques of QDs, the most common is the *Stranski-Krastanow* method [41]. It makes use of the growth technique called molecular beam epitaxy (MBE) which is based on the deposition on a substrate of crystalline atomic layers of different materials. When a material is grown onto a substrate with different lattice constant only the first monolayers crystallize in the epitaxial form, i.e. strained layers with the lattice constant equal to that of the substrate. When a critical thickness is exceeded, the accumulated strain in the layer leads to the formation of islands with similar sizes and shapes randomly distributed over a thin layer of the same material called the *wetting layer* (WL). The QDs grown by this procedure are named *self-assembled QDs*. The lattice mismatch between InAs and GaAs, the materials used in this Thesis, is 7%. For further applications, the QDs are usually capped with the same material as the substrate. The average size and shape of these QDs mainly depend on the strain between the different layers, the growth temperature and the deposition rate. The self-assembled QDs are typically lens-shaped with lateral size of ~30 nm and height of ~5 nm. The simplicity of the procedure, the size and shape homogeneity of the QDs and their defect-free character are among the greatest advantages of the Stranski-Krastanow method.

Carrier confinement inside the QD results when the bandgap of the barrier material (substrate and capping layer) is larger than that of the QD, as it is shown in Figure 2.1. If

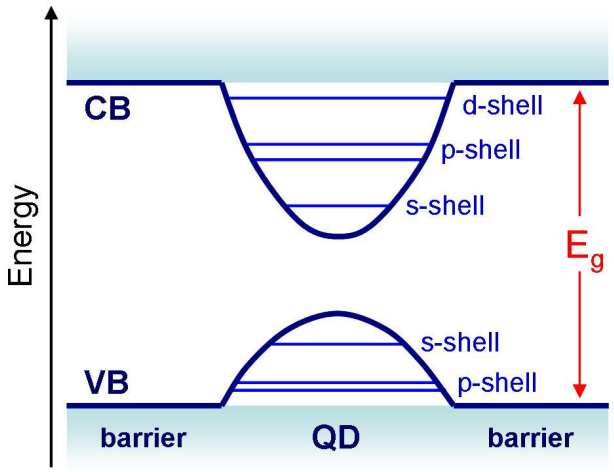


**Figure 2.1.** Confinement potential scheme of a QD showing the variation of the valence (VB) and conduction (CB) band energies and the quantized levels in the dot region.

the QD size is comparable with the de Broglie wavelength, electron and hole levels are fully quantized giving rise to narrow optical transitions, as in atoms. These quantized states can be classified by their total angular moment in atom-like shells also named *s, p, d,* … [42]. The electrons and holes occupy the confined electronic shells in numbers according with the Pauli's exclusion principle. The number of confined states inside the QD and their energy distribution depend on the confinement potential, i.e. on the size, shape, strain and composition of the QD [43], so that in general they change from dot to dot.

**Neutral QD states**

In the ground state of a neutral (undoped) QD, all the single particle valence band (VB) states are filled, while all the conduction band (CB) states are empty. When light of the proper energy is absorbed, one electron can be excited across the bandgap leaving a hole in the VB state. Together, electron and hole form an *exciton* (X) due to the spatial confinement and the Coulomb interaction. In a first approximation, only heavy holes are involved in the optical transitions, as heavy and light hole subbands are no longer degenerate and light holes will decay very efficiently into heavy hole states [25]. Thus, the lowest energy state of the QD with one exciton consists of four substates coming from the combination of the electron states ($J = \pm 1/2$) and the hole states ($J = \pm 3/2$). Two of these states have total angular momentum $M = \pm 1$ and are optically accessible by circularly polarized light, so they are called *bright exciton* states. The other two have total angular momentum $M = \pm 2$ and are forbidden by quantum selection rules in the dipole approximation, so they are called *dark exciton* states.

In this picture, the four states with $M = \pm 1, \pm 2$ should be degenerate. However, due to asymmetries in the QD shape and Coulomb interactions between the carriers, this degeneracy is lifted. The electron-hole exchange interaction splits this quartet into the radiative doublet $|\pm 1\rangle$ and two non-radiative states formed by the symmetric and antisymmetric combinations of $|\pm 2\rangle$ states [25]. The anisotropic confinement potential also mix the $M = \pm 1$ states. Then, the four resulting states are given by:

$$\begin{aligned} |X_{x,y}\rangle &= \frac{1}{\sqrt{2}}\left(|+1\rangle \pm |-1\rangle\right) \\ |DX_{\pm}\rangle &= \frac{1}{\sqrt{2}}\left(|+2\rangle \pm |-2\rangle\right) \end{aligned} \tag{2.1}$$

where X (DX) denotes bright (dark) exciton states. With this mixture of states, the optical decay from the X states results in two emission lines of orthogonal linear polarizations ($\Pi_{x,y}$), split by the *fine structure splitting* (FSS), the energy difference

between both states. The FFS has values of the order 0-500 μeV depending on the individual properties of each QD.

For enough power of the excitation light source, a second electron-hole pair can be formed in the QD. This two-exciton state is known as *biexciton* (XX). The lowest energy state of the XX is a singlet in which both electrons and holes fill the *s*-shell in the conduction and valence band respectively. The XX state usually presents a binding energy ($E_B$) that shifts the XX line with respect to the X line. Consequently, if the QD is in the XX state, it can emit two photons of different energy. The first photon originates in the transition from the XX to the X state and the second one in the transition from the X to the ground state, leading to a cascade emission. The relative position of both lines is determined by the combination of two effects, the direct Coulomb interaction and the correlation between the different electron and hole levels [44]. The former depends on the relative size and shape of the wavefunctions in the QD and it shifts the XX transition to energy higher than the X one (antibinding). The correlation effect is governed by the number of bound electron and hole states in the QD potential, which depend on the QD size. Then, the combination of both effects leads to the experimental observation of a transition from a binding ($E_{XX} < E_X$) to an antibinding ($E_{XX} > E_X$) XX as the X transition energy increases, i.e. the QD size decreases [44, 45]. Due to the character of the final states in the XX transition, the XX emission is also split into two lines with orthogonal linear polarizations separated by the FSS. The level scheme of a neutral QD with the X and XX transitions and their optical properties is shown in Figure 2.2. More than two excitons can be created in the QD by successively filling the consecutive shells (*p, d,…*).

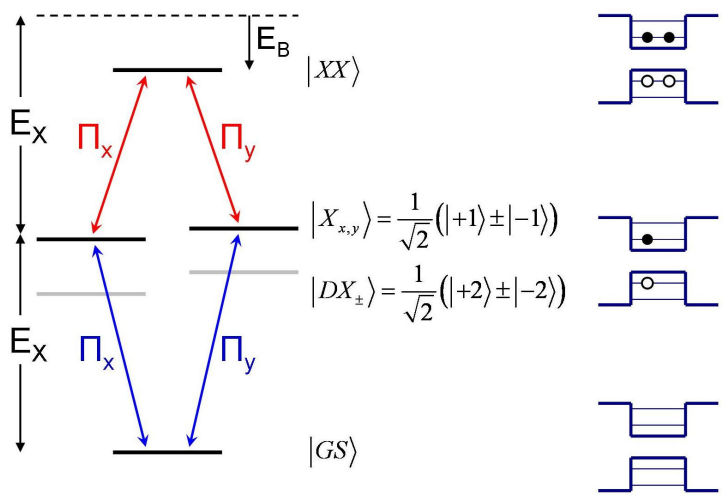


**Figure 2.2.** Neutral QD level scheme showing the X and XX transitions. On the right, single particle representation of the different states.

In photoluminescence (PL) measurements (see Chapter 3), X and XX transitions can be distinguished by the different dependence of their PL intensities on the excitation power. Ideally, below saturation conditions, the X line shows a linear power-dependence while XX one presents a quadratic one [46].

**Charged QD states**

If an electron or a hole is present in a QD, the QD level structure changes due to the Coulomb interaction of the photocreated carriers with the present charge. The ground state of a QD charged with an electron (hole) has spin $|J| = 1/2$ ($3/2$) and is doubly degenerate. This QD can be excited forming a negative charged exciton state having two electrons and one hole ($X^-$) or a positive charged exciton state having one electron and two holes ($X^+$). This state is known as *trion*. The trion state is also doubly degenerate and produces unpolarized emission lines. Its power-dependence shows a linear trend as in the case of the X transition. The level scheme of a negatively charged QD is shown in Figure 2.3.

The shifts of positive and negative trions with respect to the neutral X usually depend on the QD shape and size which determines the competition in favour of the electron and hole interaction or of the electron-electron (or hole-hole) repulsion. Calculations based on lens-shaped In(Ga)As/GaAs QDs [47] reveal that for the flatter dots (with height around 10% of the dot base), the $X^-$ line is red-shifted with respect to the neutral X, while the $X^+$ is blueshifted. This situation is reversed as the dot height increases up to values of 30% of the dot base. The former situation, the one of the flatter dots, is the mostly found experimentally in self-assembled QDs [44, 48].

The trion state can be excited again giving rise to a charged biexciton ($XX^{\pm}$) with two electrons and three holes or viceversa. On the other hand, the QD can be doped with more than one electron or hole forming charged excitons like $X^{2\pm}$, $X^{3\pm}$, …

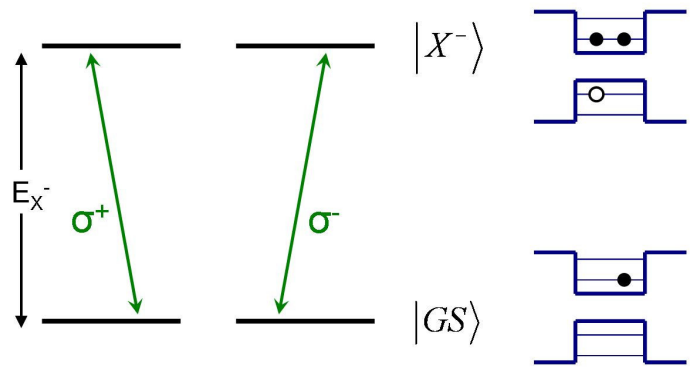


**Figure 2.3.** Negatively charged QD level scheme showing the $X^-$ transition. On the right, single particle representation of the different states.

**Quantum rings**

Depending on the growth conditions different shapes of the 0D-structures can be obtained [49]. Nanostructures which present similar properties to QDs are the so-called *quantum rings* (QRs). Their electronic structure is analogous to QDs, with exciton, biexciton, etc. states [50, 51]. Moreover photon antibunching has been observed in QR nanostructures revealing their potential use in single photon emission devices [4]. However, their ring-like shape also gives rise to new properties which make them very interesting systems. Firstly, they allow better control of the energy levels (hence of their optical properties) than QDs by varying shape parameters such as ring width or outer-to-inner radius ratio [52]. Secondly, they present Aharonov-Bohm effects in the form of oscillatory persistent currents as a result of the electron confinement in submicron rings [5, 6].

The optical properties of InAs/GaAs self-assembled QRs have been studied in this Thesis. The bandgap energies of these materials are $E_g$(InAs) = 0.41 eV and $E_g$(GaAs) = 1.52 eV at low temperature. In the QRs, the emission energy of the ensemble is blueshifted with respect to the energy of the corresponding QDs (~ 1.13 eV) suggesting an increased confinement. The experimental values of the QR ensemble and the WL emission energies, the XX binding energy and the FFS found for the InAs/GaAs QRs studied in this Thesis are shown in Table 2.1.

| $E_{ensemble}$ | $E_{WL}$ | $E_B$ | FSS |
|---|---|---|---|
| 1.316 eV | 1.455 eV | 1-2.5 meV | not resolved |

**Table 2.1.** Experimental values of $E_{ensemble}$, $E_{WL}$, $E_B$ and FSS for InAs/GaAs QRs.

## 2.1.2. Photonic crystal microcavities

Optical microcavities confine the light of resonant frequencies to small volumes for long times. An ideal cavity would confine light indefinitely (without loss) and would have resonant frequencies at precise values. Two main parameters characterize a microcavity: the quality factor (Q) and the modal volume ($V_m$). $V_m$ gives a measure of the spatial confinement of the light within the cavity. Q is determined by the energy loss rate relative to the stored energy. It can be expressed by the ratio between the frequency and the spectral width of the cavity resonance:

$$Q = \omega_c / \Delta\omega_c \tag{2.2}$$

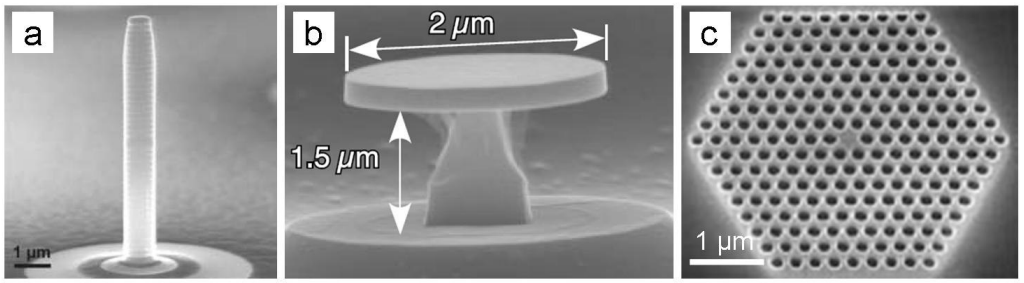


**Figure 2.4.** SEM pictures of the different types of microcavities: (a) Micropillar cavity [16]. (b) Microdisk cavity [54]. (c) PC microcavity [53].

Devices based on solid state optical microcavities are essential for a wide range of applications. One of the most interesting ones is the study of the light-matter interaction. As it will be shown in Section 2.1.3, high Q and small $V_m$ are desirable to enhance the effects of this interaction. Different designs of optical microcavities have been performed in order to achieve these requirements [53].

The most basic example is a *micropillar cavity* (Figure 2.4(a)). They are fabricated by etching a small pillar in a semiconductor structure containing two parallel Bragg reflectors in order to form a one-dimensional cavity. The emitter is located between the two reflectors. The Bragg mirrors provide the vertical confinement while the in-plane confinement is given by the air-dielectric refraction index mismatch. They offer small cavity volume ($V_m \sim 5(\lambda/n)^3$) and high Q factors in the tens of thousands range.

Another cavity design is the *microsdisk cavity* (Figure 2.4(b)). It consists of a small semiconductor disk placed on a small pillar attached to the substrate. The light is strongly confined in high Q and small effective volume whispering gallery modes ($V_m \sim 6(\lambda/n)^3$) [55]. These modes are located along the edge of the disk.

The main drawback of the micropillar and microdisc cavities is that tuning (post-fabrication modifying of the resonant frequencies) can only be performed by changing the refractive index of the whole structure by varying the sample temperature. This problem can be solved by the so-called *photonic crystal microcavities* (Figure 2.4(c)), which are the ones studied in this Thesis and therefore the ones explained in more detail.

A photonic crystal (PC) is a medium with a periodic modulation of the dielectric constant on the scale of the light wavelength with high refractive index contrast [7, 56, 57]. This modulation leads to the formation of an energy band structure for electromagnetic waves propagating in it. It is known as photonic band structure. Thus, the photonic crystal is the optical analog of a crystal where the periodic location of the atoms results in an electronic band structure. In some cases, the photonic band structure

can present a photonic bandgap, a forbidden region which prohibits the propagation of the light with frequency within the gap.

The quantitative study of the propagation of light in a PC requires solving the Maxwell equations with proper boundary conditions. Under the assumptions of linear regime, macroscopic, isotropic and low-loss dielectric mediums ($\varepsilon(\vec{r})$ real) and monochromatic fields, the magnetic field $\vec{H}(\vec{r})$ is given by [56]:

$$\nabla\times\left(\frac{1}{\varepsilon(\vec{r})}\nabla\times\vec{H}(\vec{r})\right)=\left(\frac{\omega}{c}\right)^2\vec{H}(\vec{r}) \tag{2.3}$$

This is the *master equation* for a given periodic dielectric constant $\varepsilon(\vec{r})$. Then $\vec{E}(\vec{r})$ can be obtained from:

$$\nabla\times\vec{H}(\vec{r})-\frac{i\omega}{c}\varepsilon(\vec{r})\vec{E}(\vec{r})=0 \tag{2.4}$$

Usually, the periodicity in the refractive index is created by micro-patterning the material. In our case, this material is a semiconductor heterostructure that includes the emitter. The most widely used example is the 2D-PC slabs which consist of a thin membrane of thickness *d* with a patterned periodic lattice of holes. In that case, the presence of the photonic bandgap results in a strong reflection for all the in-plane $\vec{k}$ vectors. The light is also confined in the third spatial direction due to total internal reflection as a consequence of the difference in the refractive index between the membrane and the surrounding area. In Figure 2.5 a PC slab with a triangular lattice of circular holes and its correspondent photonic band structure are shown.

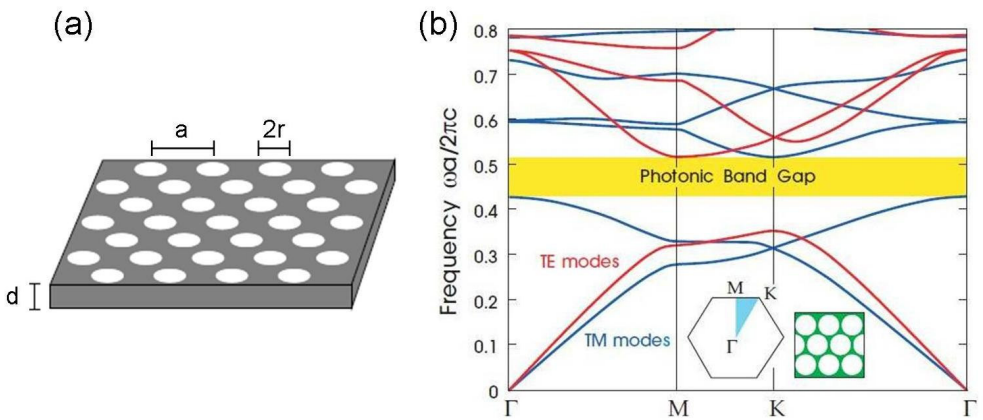


**Figure 2.5.** (a) Illustration of a triangular lattice PC slab. (b) Photonic band structure for light propagation of the PC slab shown in (a) [56].

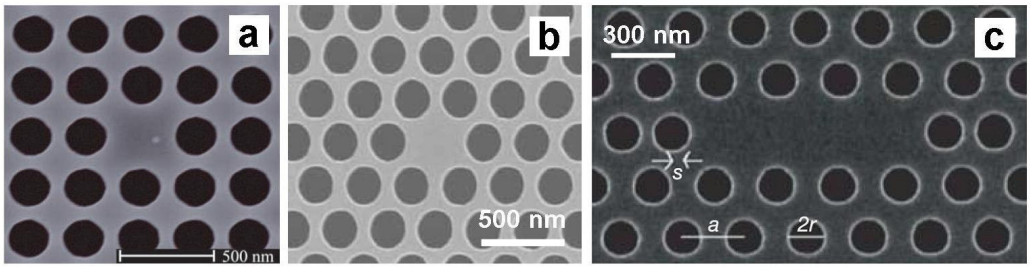


**Figure 2.6.** SEM images of different types of PC microcavities (a) S1 [58]. (b) H1 [59]. (c) L3 [17]. Slight outward displacements of the edge holes occur in (b) and (c).

By introducing a defect in the PC structure, a set of discrete states can appear inside the photonic band gap. These "defect" states lead to the cavity modes. There are many possible defect geometries: different size of the holes, slight local deviations from the periodicity and missing holes. The latter is the most common defect, from which some examples are shown in Figure 2.6. An S1 cavity is formed by a single missing hole in a square lattice (Figure 2.6(a)). Similarly, an H1 cavity is made by a single missing hole in a triangular lattice (Figure 2.6(b)). In a L3 cavity three holes are missing (Figure 2.6(c)). Each geometry has different number of cavity modes with different energies which depend on the lattice constant of the patterned holes (*a*), the radius of the holes (*r*), the index contrast and the thickness of the membrane (*d*). A shift towards lower energy is observed in the mode emissions when the so-called filling factor (*r/a*) is decreased.

The modal volume $V_m$ in PC microcavities is defined as:

$$V_m = \frac{\int \varepsilon(\vec{r})\vec{E}^2(\vec{r})d^3\vec{r}}{\left(\varepsilon(\vec{r})\vec{E}^2(\vec{r})\right)_{\max}} \tag{2.5}$$

and gives values in the order of $\left(\lambda/n\right)^3$, which are considered to be in the limit of the smallest accessible modal volumes [60]. Moreover, extremely high theoretical Q factors can be achieved by introducing some implementations in the basic structure. For example, slight displacements of the air holes at the edges of the cavity decrease the energy loss yielding a significant enhancement of the Q factor with values of several tens of thousands [61].

### 2.1.3. Light-matter interaction in microcavities

Cavity Quantum Electrodynamics (cQED) describes the interaction of an atom-like emitter with confined photons [7-11, 41]. The first studies were done in atomic systems using traps to localize an atom in the field of a cavity mode [62]. Nowadays, enormous

progress has been done in solid state nanostructures which offer permanent positioning of the quantum emitters in the center of the microcavities. In this context, self-assembled QDs immersed in solid state microcavities have been shown to combine efficient emission and small modal volume.

**The Jaynes-Cummings Model**

In an ideal case, a two-level system (the quantum emitter) is resonantly coupled to a lossless cavity mode. After excitation of the emitter a photon is emitted at a given spontaneous rate. The photon is stored in the CM and can be reabsorbed by the quantum emitter. This means that the emission process is reversible and the periodic emission and absorption of the photon is described in terms of Rabi oscillations. The Rabi frequency determines the strength of the emitter-cavity coupling.

In this case, the system is described by the Jaynes-Cummings Hamiltonian [10, 11]:

$$\hat{H} = \hat{H}_0 + \hat{H}_I \tag{2.6}$$

where the first and second terms represent the free and interaction Hamiltonians respectively, and are given by :

$$\hat{H}_0 = \hbar\omega_a \hat{\sigma}_+ \hat{\sigma}_- + \hbar\omega_c \hat{a}^\dagger \hat{a} \tag{2.7}$$

$$\hat{H}_I = \hbar g \left( \hat{\sigma}_+ \hat{a} + \hat{\sigma}_- \hat{a}^\dagger \right) \tag{2.8}$$

Here, $\hbar\omega_a$ and $\hbar\omega_c$ are the atomic transition and the cavity mode energies respectively, $g$ is the atom-photon coupling strength, $\hat{\sigma}_\pm$ are the atomic raising and lowering operators and $\hat{a}$ is the annihilation operator of the electromagnetic field.

The atom-photon coupling strength is defined as the scalar product of the dipole moment of the atom and the local electric field at the atom position in the cavity: $g = \left| \left\langle \vec{p} \cdot \vec{E} \right\rangle \right|$. For the ideal case of the emitter located at the maximum of the electric field distribution of a CM, the coupling strength is given by:

$$g = \frac{p}{\hbar} \sqrt{\frac{\hbar\omega_c}{2\varepsilon_r \varepsilon_0 V_m}} \tag{2.9}$$

where $p$ is the module of the dipole momentum of the transition and $\varepsilon_r$ is the relative dielectric constant of the cavity medium.

The *bare* states of the uncoupled system can be labeled by the state of the atom $\psi$ and the number of photons $n$ ( $n \geq 0$ ) as follows:

$$\Psi = \left| \psi; n \right\rangle \tag{2.10}$$

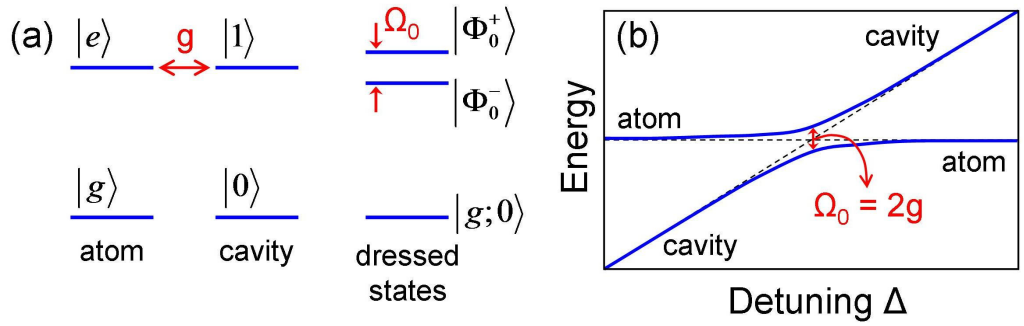


**Figure 2.7.** (a) Formation of the dressed states at resonance for $n = 0$. (b) Schematic illustration of the anticrossing of the atom-cavity system.

In this way, $|e;n\rangle$ denotes the excited state atom and $n$ photons and $|g;n+1\rangle$ represents the ground state atom and $n+1$ photons. Solving the Hamiltonian in each subspace defined by $n$, the eigenstates are given by:

$$\begin{aligned}\Phi_n^+ &= \cos(\phi_n/2)|e;n\rangle + \sin(\phi_n/2)|g;n+1\rangle \\ \Phi_n^- &= -\sin(\phi_n/2)|e;n\rangle + \cos(\phi_n/2)|g;n+1\rangle\end{aligned} \tag{2.11}$$

These are the so-called *dressed states* and the angle $\phi_n$ is defined through:

$$\tan\phi_n = \left(\frac{2g\sqrt{n+1}}{\Delta}\right) \tag{2.12}$$

where $\Delta = \omega_a - \omega_c$. The corresponding eigenvalues are:

$$\omega_n^{\pm} = \left(n+\frac{1}{2}\right)\omega_c \pm \sqrt{\frac{\Delta^2}{4} + g^2(n+1)} \tag{2.13}$$

In the limit of exact resonance ($\omega_a = \omega_c$) the bare states are degenerate but the splitting of the dressed states remains. In this limit, the dressed states and the corresponding eigenvalues are given by:

$$\Phi_n^{\pm} = \frac{1}{\sqrt{2}}\left(|e;n\rangle \pm |g;n+1\rangle\right) \tag{2.14}$$

$$\omega_n^{\pm} = \left(n+\frac{1}{2}\right)\omega_c \pm \sqrt{n+1}\; g \tag{2.15}$$

This situation is illustrated in Figure 2.7(a) for the case $n = 0$. In this case, the spectrum consists of two lines separated by $\hbar\Omega_0 = 2\hbar g$. This is the vacuum Rabi splitting and can be experimentally observed by measuring an anticrossing between the cavity and the atom transition when they are brought into resonance (Figure 2.7(b)).

**Strong coupling regime and weak coupling regime**

In real microcavities, photons are not indefinitely confined, but they leave the cavity after a characteristic time. This photon loss rate is inversely proportional to the quality factor $\kappa = \omega_c / Q$ (notice from equation (2.2) that $\kappa = \Delta\omega_c$). Moreover, the relaxation rate of the atom transition (γ) constitutes a second loss mechanism. Rabi oscillations can be still visible if the coupling rate between the emitter and the CM is larger than the loss rates. In this situation, called *strong coupling* regime, the coupled system is characterized by two eigenstates separated by the vacuum Rabi splitting. On the other hand, if irreversible decay dominates the system, it is said to be in the *weak coupling* regime. In this situation the spontaneous emission of an emitter can be enhanced or inhibited compared to its vacuum level by tuning the emitter in and out of resonance with the CM. Considering this more realistic system, the Hamiltonian can be diagonalized to give the following eigenvalues (with $\omega_\pm$ frecuencies and $\Gamma_\pm$ linewidths) for the dressed states [15]:

$$\omega_\pm + i\Gamma_\pm / 2 = \frac{\omega_c + \omega_a}{2} - i\frac{\kappa+\gamma}{4} \pm \sqrt{g^2 + \frac{1}{4}\left(\Delta - i\frac{\kappa-\gamma}{2}\right)^2} \tag{2.16}$$

where $\Delta = \omega_a - \omega_c$. At resonance they are reduced to:

$$\omega_\pm + i\Gamma_\pm / 2 = \frac{\omega_c + \omega_a}{2} - i\frac{\kappa+\gamma}{4} \pm \sqrt{g^2 - \left(\frac{\kappa-\gamma}{4}\right)^2} \tag{2.17}$$

The distinction between the weak and the strong coupling regimes can be given now from the sign of the expression in the square root in equation (2.17):

$$\begin{aligned} strong\ \ coupling\ \ &\rightarrow\ \ 4g > |\kappa - \gamma| \\ weak\ \ coupling\ \ &\rightarrow\ \ 4g \le |\kappa - \gamma| \end{aligned} \tag{2.18}$$

Since usually the atom transition linewidth is significantly smaller than the CM one, the previous condition can be simplified to:

$$\begin{aligned} strong\ \ coupling\ \ &\rightarrow\ \ 4g > \kappa \\ weak\ \ coupling\ \ &\rightarrow\ \ 4g \le \kappa \end{aligned} \tag{2.19}$$

**Strong coupling regime and vacuum Rabi splitting**

In the strong coupling regime, the spectrum consists of two lines at frequencies $\omega_\pm$ given by equation (2.16). The splitting at resonance between the two dressed states is given by the new vacuum Rabi splitting:

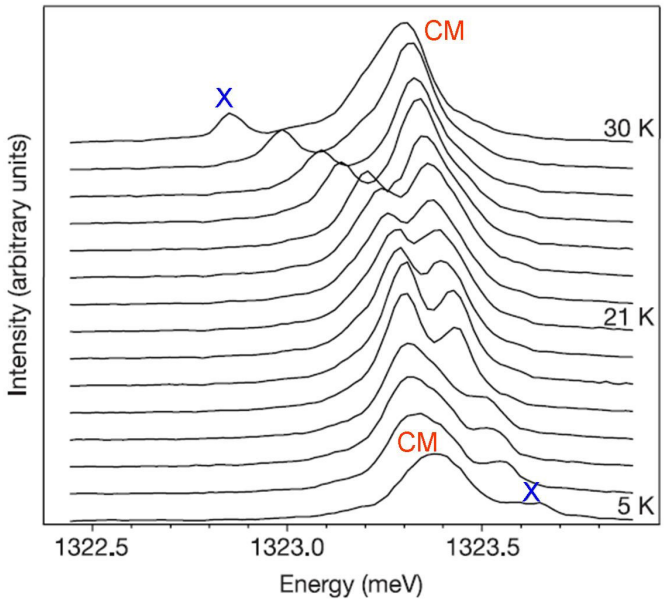


**Figure 2.8.** Temperature-dependent PL spectra of a QD-micropillar cavity system showing a clear anticrossing when X and CM lines are brought into resonance [16].

$$\Omega_R = 2\sqrt{g^2 - \left(\frac{\kappa - \gamma}{4}\right)^2} \tag{2.20}$$

It is smaller than the one obtained for the ideal lossless system ($\Omega_0 = 2g$). It has already been explained that this situation corresponds to a reversible process in which a coherent exchange of energy between the atom and the cavity occur. Strong coupling has been experimentally observed many times in the last years for QD-CM systems [15-17, 63-67]. An example of the anticrossing observed in the strong coupling regime is shown in Figure 2.8 [16].

In practice, self-assembled QDs in solid state cavities cannot be described exactly by a two-level system, because the solid state environment induces a more complicated dynamics. Firstly, the QD is usually excited far above resonance so that emission is preceded by incoherent electron-hole pair relaxation. Secondly, as will be shown below, other surrounding QDs may contribute to the cavity mode emission due to off-resonance coupling. Recent theoretical work performed by *Laussy et al.* [68] has shown that, under QD and cavity incoherent pumping, strong coupling can hold in the absence of a visible anticrossing due to decoherence-induced broadening of the lines. Indeed, they define a new criterion for strong coupling and give a *phase diagram* showing regions of strong coupling in the absence of a visible anticrossing (region 2 in Figure 2.9(a)). By

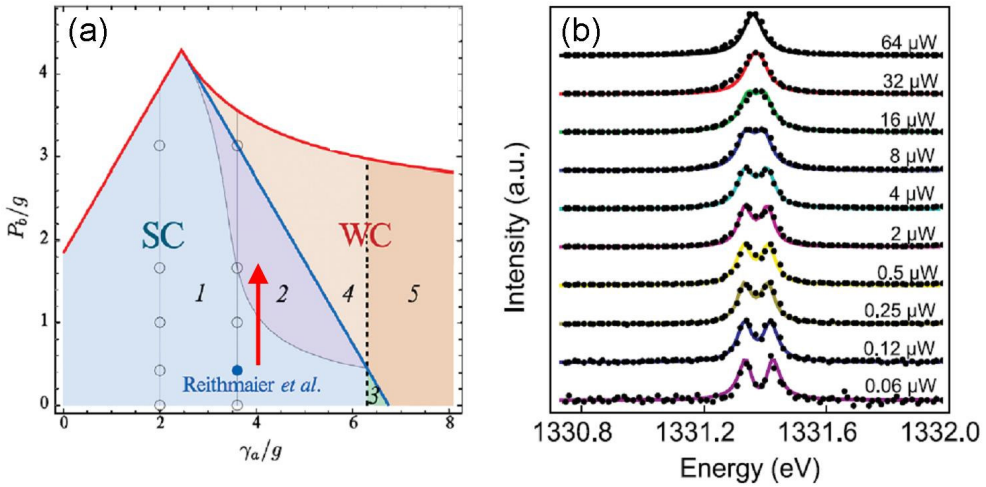


**Figure 2.9.** (a) Phase diagram of strong (blue) and weak (red) coupling regimes in the space of the cavity decay rate ($\gamma_a$) and QD pumping rate ($P_b$) [68]. (b) Emission spectra of a coupled QD-CM system on resonance showing the evolution from a double to a single peak as the excitation power is increased [67]. It would correspond to a phase transition given by the red arrow in (a).

decreasing the QD pumping, a situation with visible Rabi splitting should be recovered. This effect has already been observed experimentally [67, 69], as shown in Figure 2.9(b). *Laucht et al.* [69] also propose an analytical solution including, apart from incoherent pumping, pure dephasing of the exciton of the QD. Their theoretical and experimental results show that strong coupling can be compatible with a single peak by increasing not only the excitation intensity but also the sample temperature.

**Weak coupling regime and Purcell effect**

The weak coupling regime is observed when the loss rates (κ and γ) dominate over the coupling strength ($g$). The *spontaneous emission* (SE) rate of an emitter placed inside a cavity is strongly modified compared to the one without cavity. This problem was first considered by E.M. Purcell in 1946 [13], so it is known as the Purcell effect.

Let us consider a two level emitter (exciton in a QD) weakly coupled to a single resonant mode of a PC cavity. We assume that only one CM is close to the emission frequency of the QD. The total SE rate of the QD at position $\vec{r}_A$, spectrally detuned from the cavity resonance frequency by $\Delta = \omega_X - \omega_{cav}$, can be expressed as the sum of rates into cavity mode and other modes in the PC [14]:

$$\Gamma = \Gamma_{cav} + \Gamma_{PC} \tag{2.21}$$

The SE rate can be calculated by the Fermi's golden rule:

$$\Gamma = \frac{1}{\tau} = \frac{2\pi}{\hbar^2}\left|M\right|^2 D(\omega) \tag{2.22}$$

where *M* is the transition matrix element and *D(ω)* is the density of states.

For a dipole inside a cavity considering a Lorentzian density of states, the SE rate is given by:

$$\Gamma_{cav} = \frac{1}{\tau_{cav}} = \frac{2Qp^2}{\varepsilon_0 \hbar V_m}\left(\frac{\left|\vec{p}\cdot\vec{E}(\vec{r}_A)\right|}{\left|\vec{p}\right|\left|\vec{E}\right|}\right)^2 \frac{\kappa^2}{4\Delta^2+\kappa^2} \tag{2.23}$$

where *p* is the dipole moment. Comparing this expression with the SE rate in the free space (without cavity or PC influence) given by [8]:

$$\Gamma_{free} = \frac{1}{\tau_{free}} = \frac{p^2\omega_X^3}{3\pi\varepsilon_0\hbar c^3} \tag{2.24}$$

we obtain:

$$\frac{\Gamma_{cav}}{\Gamma_{free}} = \frac{\tau_{free}}{\tau_{cav}} = \frac{3Q}{4\pi^2 V_m}\left(\frac{\lambda}{n}\right)^3\left(\frac{\left|\vec{p}\cdot\vec{E}(\vec{r}_A)\right|}{\left|\vec{p}\right|\left|\vec{E}\right|}\right)^2 \frac{\kappa^2}{4\Delta^2+\kappa^2} \tag{2.25}$$

where λ is the free-space wavelength of the light and *n* is the refractive index of the medium inside the cavity. At resonance (Δ = 0) and with the dipole oriented along the field direction, equation (2.25) reduces to:

$$F_P = \frac{3Q}{4\pi^2 V_m}\left(\frac{\lambda}{n}\right)^3 \tag{2.26}$$

This is the Purcell factor that characterizes the effects of the cavity. Thus, if $F_P > 1$ there is an enhancement of the SE rate. On the contrary, if $F_P < 1$ the cavity inhibits the emission.

It is important to notice from equation (2.26) that the figure of merit for achieving large Purcell enhancement is $Q/V_m$, so again high Q-factors and small modal volumes are desirable.

**Coupling mechanism in the off-resonance condition**

In the framework of the Jaynes-Cumming Hamiltonian, when the emitter is strictly monochromatic as compared to the CM line ($\gamma << \kappa$), the CM excitation is only expected to occur in the resonance condition. In this way, emission at the energy of the CM should be essentially negligible outside the QD-CM crossing region [70]. However, strong off-resonance emission of a CM has been reported in most of the studied cases. It

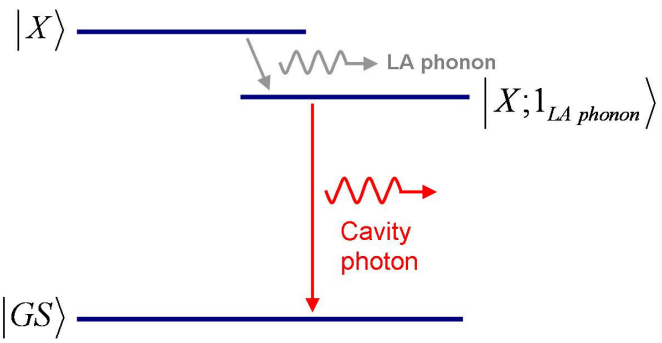


**Figure 2.10.** Scheme of the cavity feeding mediated by LA-phonon emission.

was initially attributed to the presence of a certain number of QDs into the cavity region which gives a significant probability for the CM to be near resonance with some QD transition. Nevertheless, recent research based on the deterministic location of one single QD in the cavity [15, 58, 71] have shown the off-resonance emission of the CM which cannot be explained in these terms. Moreover, in these cases, cross-correlation measurements between the QD and the CM transitions show antibunching, proving that the *cavity feeding* is mediated only by a single QD [15, 64, 72-74]. Indeed, this anticorrelation has been observed at detunings of up to 13 meV [72]. In some cases also clear antibunching is observed in the off-resonance CM auto-correlation function for detunings smaller than 1 meV [64, 73, 74].

All the features exposed above imply the existence of an intrinsic dot-cavity coupling mechanism, whose origin is still under discussion.

Some possible explanations discussed in the literature, as emission from 2D-wetting layer states, crossed 0D-2D transitions and excited state QD transitions, can be excluded as they result in emission at higher energy than the fundamental exciton transition in the dot. In contrast, the out-of-resonance QD-CM coupling has been observed also for CM emission energies lower than the QD one [72].

Another possibility is based on the exciton-phonon coupling derived from the semiconductor solid state environment of the QD. The excitation energy of the QD can be transferred to the CM by absorption or emission of thermally activated longitudinal acoustic (LA) phonons (see scheme in Figure 2.10). This phonon assisted coupling leads to an asymmetry in the QD spontaneous emission decay time with respect to the sign of the detuning [75]. At low temperatures, the phonon assisted scattering rate from exciton to cavity is efficient only for positive detunings ($\omega_{QD} > \omega_{cav}$), associated with phonon emission. As a consequence, a decrease in the decay time of the QD transition for positive detunings compared with the corresponding negative ones is observed. By

increasing the temperature phonon absorption becomes more important due to thermal occupation of the relevant phonon modes and the scattering rate and the QD decay time become more symmetric. Such processes have been shown recently to dominate the non-resonant cavity coupling at small detunings (up to ~3 meV) [74, 75], but are extremely unlikely at large ones [72, 76]. Therefore they cannot explain the far off-resonance cavity feeding.

A new model which ensures the presence of a quasicontinuum of excitonic transitions has been proposed by *Winger et al.* [77]. They found that the emission spectrum of a QD presents, in addition to the discrete lines, a broad spectral background, as a consequence of the hybridization of localized QD states and continuum states of the WL [78]. The part of this background that overlaps with the cavity resonance is then enhanced by the Purcell effect, giving an explanation for the far off-resonance cavity feeding.

**Influence of the CM in the QD polarization**

For many applications the polarization of the photons emitted by the QD is of great importance. This is the case of quantum cryptography where the photon polarization may be used to encode the qubit information [26]. In QDs embedded in optical microcavities, the usually strongly polarized CMs have a strong influence in the polarization of the QD emission.

The enhancement of the spontaneous emission rate due to the Purcell effect (equation (2.25)) affects selectively the photons of the same polarization as the involved CM. This effect has been experimentally observed for both micropillars [28, 29] and photonic crystal microcavities [30, 31].

*Daraei et al.* [28] report results of a single dot emission coupled to an elliptical microcavity pillar with two non-degenerate optical modes with orthogonal linear polarizations. The single dot emission is found to become parallel to that of the spectrally closest CM by measuring the degree of polarization $\rho = \frac{I_X - I_Y}{I_X + I_Y}$, where X and Y corresponds to directions parallel and perpendicular to the long axis of the pillar respectively. Their results are shown in Figure 2.11 where the polarization degree of the QD emission is plotted as a function of the energy at which the emission occurs for different temperatures. The PL spectra at high excitation power are also shown to indicate the position and linewidth of the modes.

Besides, *Oulton et al.* [30] show that QDs coupled to a L3-type photonic crystal microcavity maintain their polarization parallel to the CM even for large detunings. They found a strong polarization in the emission of almost all the QDs that matches the one of the closest CM for different L3-cavities. Figure 2.12(a) shows the Y-polarized PL

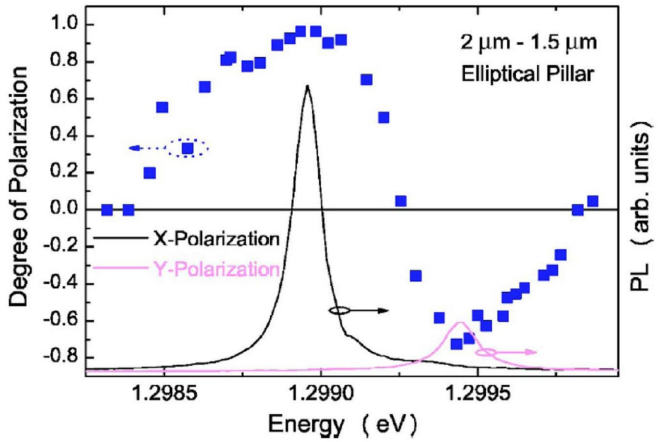


**Figure 2.11.** Variation of the degree of polarization (blue squares) of the emission of a QD coupled to an elliptical micropillar cavity as a function of the QD emission energy for different temperatures [28]. High power PL spectra at X (black line) and Y (pink line) polarizations of the CM emissions are also displayed.

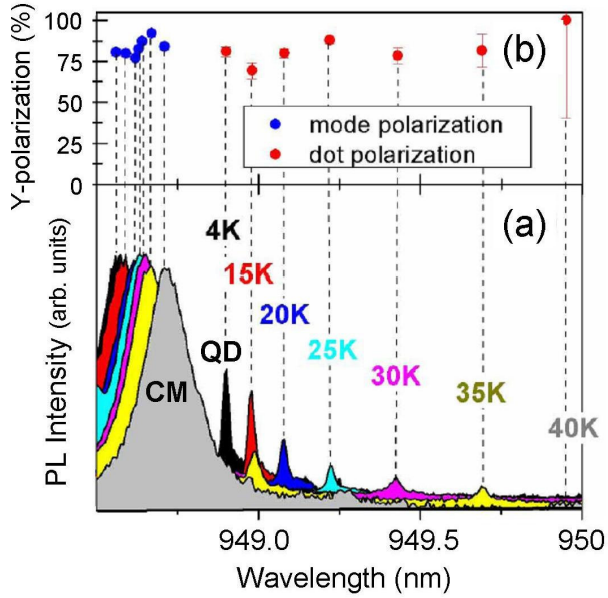


**Figure 2.12.** (a) PL spectra for increasing temperature and for Y-polarization, showing the QD and CM emissions [30]. (b) Percentage of Y-polarization of the CM (blue) and QD (red) in each case.

spectra of a CM and a QD for different temperatures. The QD polarization is found to be almost parallel to the CM one even for large detunings (40K), as shown in Figure 2.12(b).

### 2.1.4. Coherent coupling of semiconductor QDs

Self-assembled QDs embedded in optical microcavities have become an attractive system for solid state cQED due to their potential applications as elementary units for quantum information processing (qubits). Fast and long-distance interactions between semiconductor qubits are required for quantum logic operations. As has been shown in the previous section, strong coupling between a single QD and a resonant mode of a microcavity has been fully demonstrated. The next step goes through achieving coherent interaction among individual QDs. The QD-CM coupling for large detunings, even in the weak coupling regime, opens the possibility to couple two spectrally distinct QDs via the CM. Then, the cavity would act as a vehicle for quantum information that couples qubits with large spatial separation [18].

The physics of two qubits with no direct coupling but both coupled to the same CM with $g_1 \neq g_2 \neq 0$ can be described (by means of a Schrieffer-Wolff transformation) by the following Hamiltonian [79]:

$$\begin{aligned}\hat{H} = \hbar\left(\omega + \frac{2g_1^2}{\Delta_1}\hat{s}_{1,z} + \frac{2g_2^2}{\Delta_2}\hat{s}_{2,z}\right)\hat{a}^\dagger\hat{a} + \hbar\left(\omega_1 + \frac{g_1^2}{\Delta_1}\right)\hat{s}_{1,z} \\ + \hbar\left(\omega_2 + \frac{g_2^2}{\Delta_2}\right)\hat{s}_{2,z} + \frac{\hbar}{2}\left(\frac{g_1^2}{\Delta_1} + \frac{g_2^2}{\Delta_2}\right)\left(\hat{s}_1^+\hat{s}_2^- + \hat{s}_1^-\hat{s}_2^+\right)\end{aligned} \tag{2.27}$$

where $\Delta_i = \omega_i - \omega$ is the detuning of qubit $i = 1,2$ with respect to the CM, $g_i$ is coupling strength between qubit *i* and the CM, $\hat{s}_i^{\pm}$ are raising and lowering operators and $\hat{s}_{i,z} = (1/2)\sigma_{i,z}$ are pseudospin operators with the Pauli matrix $\sigma_{i,z}$ for qubit *i*. The last term of equation (2.27) describe the effective coupling between the two qubits:

$$\hat{H}_{eff} = \frac{\hbar}{2} J\left(\hat{s}_1^+\hat{s}_2^- + \hat{s}_1^-\hat{s}_2^+\right) \tag{2.28}$$

with

$$J = \left(\frac{g_1^2}{\Delta_1} + \frac{g_2^2}{\Delta_2}\right) \tag{2.29}$$

The effective coupling Hamiltonian given in equation (2.28) reminds the one in equation (2.8) that describes the atom-photon interaction. Then, *J* is a measure of the coupling strength between the two qubits. The most important implication of equation (2.28) is that photon emission of one qubit into the cavity and subsequent absorption by the other qubit gives rise to an effective cavity-mediated interqubit coupling.

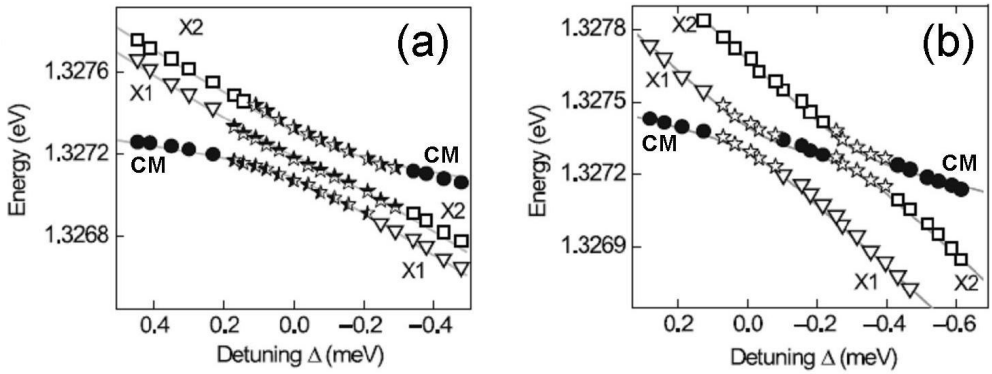


**Figure 2.13.** Peak energies as a function of detuning in a two QDs-CM system [80]. (a) Coherent coupling of X1, X2 and CM states showing a double anticrossing when the three states are brought into resonance. Mixed modes are represented by stars. (b) Two sequential anticrossings are observed if δ is larger than the individual coupling strengths.

Coherent coupling between the X transitions of two different QDs with the CM of a micropillar cavity has been observed by *Reitzenstein et al.* [80]. By changing the sample temperature, the X lines are shifted through resonance with the CM. A triple peak is observed during the double anticrossing as a result of the coherent coupling of the three quantum states (Figure 2.13(a)). This coherent coupling is observed only if the energy difference (δ) between the two X lines is of the order of the individual coupling strengths. If δ is larger than the coupling strengths, a sequential strong coupling appears, as shown in Figure 2.13(b).

The main experimental problems to realize coherent coupling between two self-assembled QDs are the simultaneous spatial and spectral overlapping of their two QDs and the CM. This is especially true in the case of PC microcavities due to their small modal volume. Some schemes of QD-spin coupling have been proposed [20, 21] based on the deterministic location of the QDs in the cavity [58, 71].

In [21], *Imamoğlu et al.* first identify two trion transitions spectrally detuned by less than 3 nm in wavelength from different QD molecules spatially separated by less than 1 μm. Then, they fabricate a PC cavity around the two QD molecules with the appropriate values of hole radius and lattice constant. By suitable choice of the type of the defect (L3, L5, L7, …) almost any spacing between the QDs in the range of 0.5-1 μm results in a high cavity field overlap for both QDs. Even if this situation is achieved, it would be still necessary to tune each trion transition independently into resonance. They propose to make use of the giant Stark shifts (few nanometers) exhibited by indirect transitions of coupled QDs [81] by fabricating independent voltage-gates for each QD molecule.

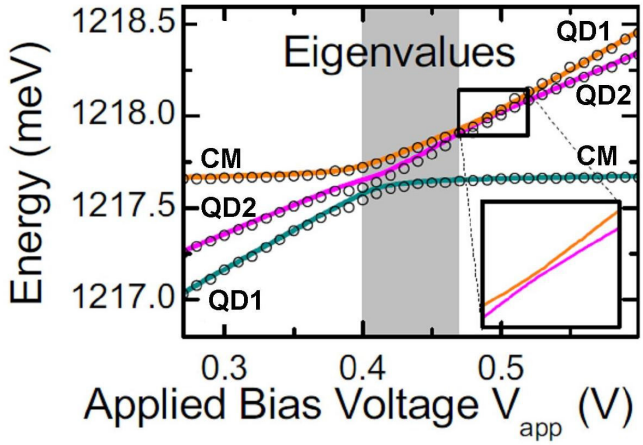


**Figure 2.14.** Emission energies of two QDs and a CM as a function of the applied voltage [83]. A double anticrossing is observed when the three states are brought into resonance. The solid lines are the calculated eigenvalues of the interaction Hamiltonian. Inset: Predicted anticrossing of the two QDs when they are in exact resonance with each other.

Another proposal for independent tuning of QDs in a PC cavity has been given by *Kim et al.* [82]. They demonstrate that, in a sample with two embedded QD layers, it is possible to tune the emission frequencies of one QD layer independently of the other by applying an electric bias to only one of them. Then, by combining this technique with the common tuning methods (temperature changing, thin film deposition (see Section 3.6.3)) it will be feasible to bring two independent QDs into resonance with a CM.

Experimental evidence of simultaneous strong coupling of two QDs to a CM of a PC microcavity has been given recently by *Laucht et al.* in [83]. They bring into resonance with the CM two different QDs by their different Stark shifts. Again, a triple peak is observed during the double anticrossing (Figure 2.14). Their results are well reproduced by calculations. The calculations also predict a small anticrossing between the two QDs when they are tuned into exact resonance with each other but not with the CM (inset in Figure 2.14). The splitting could not be resolved experimentally.

## 2.2. Indium nitride semiconductor structures

The recent discovery of the InN band gap close to 0.7 eV [35] makes this material one of the most interesting for its potential applications in future optoelectronic devices. In InGaN alloys the band gap can be varied in the range of 0.7-3.2 eV while keeping its direct character. Therefore, there is a broad interest in determining the physical properties of this semiconductor. The purpose of this section is to provide a general

overview of the essential properties of InN together with recent important results. Section 2.2.1 gives a brief description of the crystalline structure of InN. The electronic properties are described in Section 2.2.2. Vibrational properties are presented in Section 2.2.3 and a more specific description of the phonon-plasmon coupling is given in Section 2.2.4. Finally, Section 2.2.5 will focus on the general properties of InN nanocolumns.

### 2.2.1. Crystalline structure

Indium nitride (InN), as other group III nitrides, can crystallize in three different structures [84]: *wurtzite* (*α-phase*), *zinc-blende* (*β-phase*) and *rock-salt*. Under ambient conditions, the thermodynamically stable structure of InN is wurtzite. The zinc-blende structure for InN has been stabilized by epitaxial growth of thin films on (011) crystal planes of cubic substrates such as Si, SiC, MgO and GaAs. In this case, wurtzite structure could be likely present at extended defect sites. The rock-salt form is only possible under high pressure and cannot be produced by epitaxial growth. The InN samples studied in this Thesis have wurtzite structure, the one that will be described in detail in this section.

The wurtzite structure, depicted in Figure 2.15(a), consists of two interpenetrating *hexagonal close-packed* (hcp) sublattices, each one with one type of atoms (cations (In) and anions (N)). One sublattice is shifted relative to the other along the *c*-axis by a distance *b*. The wurtzite structure is then defined by three parameters shown in Figure 2.15(a): the edge length of the basal plane hexagon *a*, the height of the hexagonal prism *c* and an internal parameter characterizing the bond length parallel to the *c*-axis $u = b/c$.

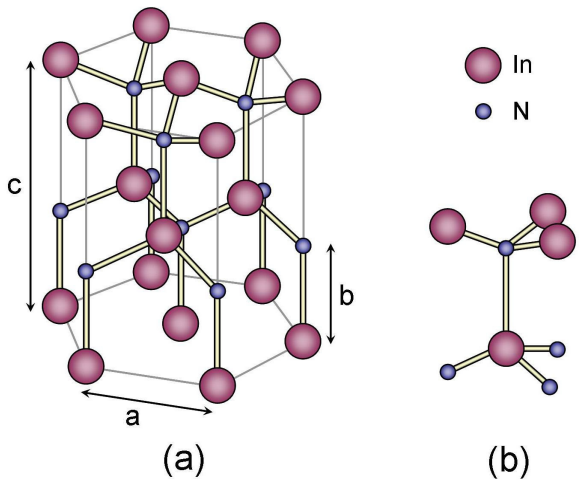


**Figure 2.15.** (a) Wurtzite structure of InN.
(b) Asymmetry between two adjacent planes along *c*-direction.

In an ideal wurtzite structure, the values of the axial ratio and the internal parameter are $c/a = \sqrt{8/3} = 1.633$ and $u = b/c = 3/8 = 0.375$. The experimental lattice constants of wurtzite InN are given in Table 2.2.

The wurtzite unit cell contains 6 atoms of each type with the basis set consisting of two In-N atom pairs. The coordination is tetrahedral with one atom species at each of the corners and the other atom species in the center. The basal plane of this structure is defined by one face of the tetrahedron and the bond perpendicular to this plane defines the *c*-axis. The asymmetry between two adjacent planes along the *c*-axis can be observed in Figure 2.15(b).

The hexagonal structures, as wurtzite, are described by four crystallographic axes (four-index notation) which are shown in Figure 2.16 by their unitary vectors $\vec{a}_1$, $\vec{a}_2$, $\vec{a}_3$ and $\vec{z}$. The *z*-direction is usually chosen parallel to the *c*-axis. A crystalline direction is given by the Miller indexes [*hkil*], where each index refers to each axis. The plane given by (*hkil*) is perpendicular to the direction with the same Miller indexes. The first three axes ($a_1$, $a_2$ and $a_3$) lie on the crystalline plane perpendicular to the *z*-axis, so that the corresponding Miller indexes are not independent, but fulfill the relation $h + k + i = 0$. The main crystallographic directions and planes are shown in Figure 2.16.

| *a* (Å) | *c* (Å ) | *c/a* | *u* |
|---|---|---|---|
| 5.7039 | 3.5365 | 1.627 | 0.377 |
| [35] | [35] | [85] | [85] |

**Table 2.2.** Experimetal parameters of InN wurtzite structure.

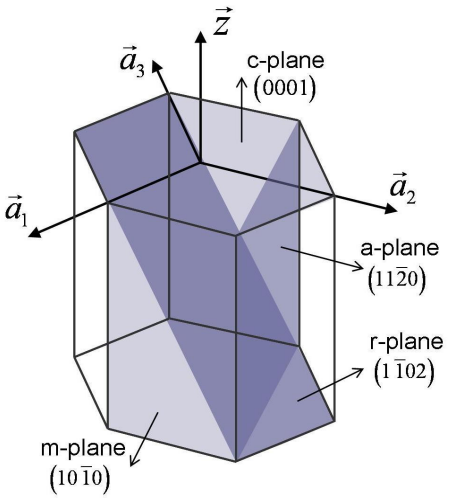


**Figure 2.16.** Main crystallographic axes and planes in the wurtzite structure.

**Surface Polarity**

A surface is said to be polar when it is made only of cations or anions, as the wurtzite basal plane (0001). The typical growth direction of the wurtzite III-nitrides is perpendicular to this plane. It occurs by the stacking of bilayers consisting of alternative planes of metal and nitrogen atoms, as can be observed in Figure 2.17. The symmetry of the wurtzite structure prevents the stacked bilayers from having equivalent atomic arrangements on either side of the bilayer. This concept is referred to as crystal polarity and two different growth directions normal to the basal plane are defined by the polarity convention [86]. The In-face orientation is defined by the one where only single bonds from the In atoms are directed toward the surface along $[0001]$ direction. The opposite direction along $[000\bar{1}]$ consists of three bonds away from the In atom and characterizes the N-face orientation.

It is important to say that polarity is a property of the bulk crystal and not of the surface. In fact, in both cases, In-polarity and N-polarity, the surfaces are terminated by In atoms, since a N-terminated surface may not be thermodynamically stable due to formation and desorption of $N_2$. The polarity strongly influences chemical and physical properties of the material. The realization of the two polarities of InN is especially sensitive to the chosen substrate and the growth technique. Thus, it cannot be predicted in a straightforward way and has to be determined experimentally.

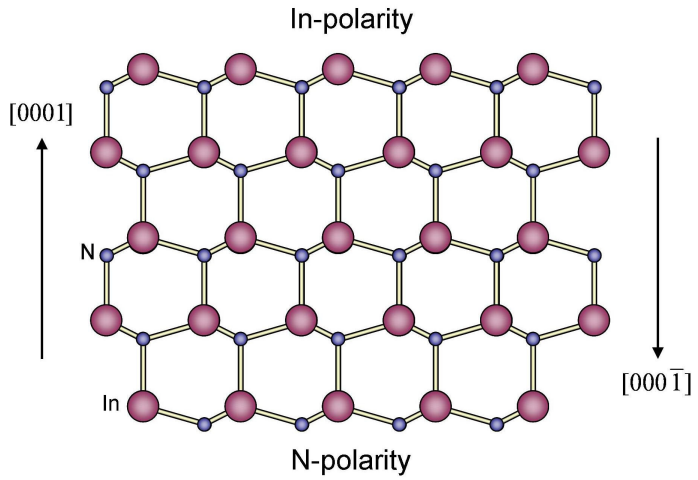


**Figure 2.17.** Atomic arrangement along the *c*-axis showing the two possible polar surfaces of wurtzite InN.

### 2.2.2. Electronic properties

The electric properties of InN have been the object of controversial discussion during the past years. The main discrepancy has been on the determination of its fundamental band gap energy, which was initially established around 1.9 eV [87]. This value has been reduced over the years until a band gap around 0.67 eV [35, 88]. This is the value currently accepted and its determination was not possible until the growth methods of InN epitaxial layers were optimized.

The electric and optical properties of bulk semiconductors are governed by their electronic band structure. The first Brillouin zone for wurtzite structure is depicted in Figure 2.18(a) showing the major symmetry points (Γ, H, K, L, A) and axes (Δ, Σ, U, R, T, P, S, T', S'). The electronic band structure of wurtzite InN calculated using the quasiparticle corrected density functional theory (QPC-DFT) is shown in Figure 2.18(b) [89]. Both valence band maximum (VBM) and conduction band minimum (CBM) occur at the Γ-point leading to a direct energy gap. A direct consequence of the narrow gap of InN is the strong non-parabolicity of the CB near the Γ-point. A simple analytical form of this non-parabolic dispersion can be obtained from the Kane´s two band $\vec{k}\cdot\vec{p}$ model [90]:

$$E_C(k) = E_g + \frac{\hbar k^2}{2m_0} + \frac{1}{2}\left(\sqrt{E_g^2 + 4E_P\frac{\hbar k^2}{2m_0}} - E_g\right) \tag{2.30}$$

where $E_g$ = 0.65 eV is the intrinsic band gap energy, $m_0$ is the electron rest mass and $E_P$ is an energy parameter related to the $\vec{k}\cdot\vec{p}$ matrix element which is typically in the range of 10-15 eV.

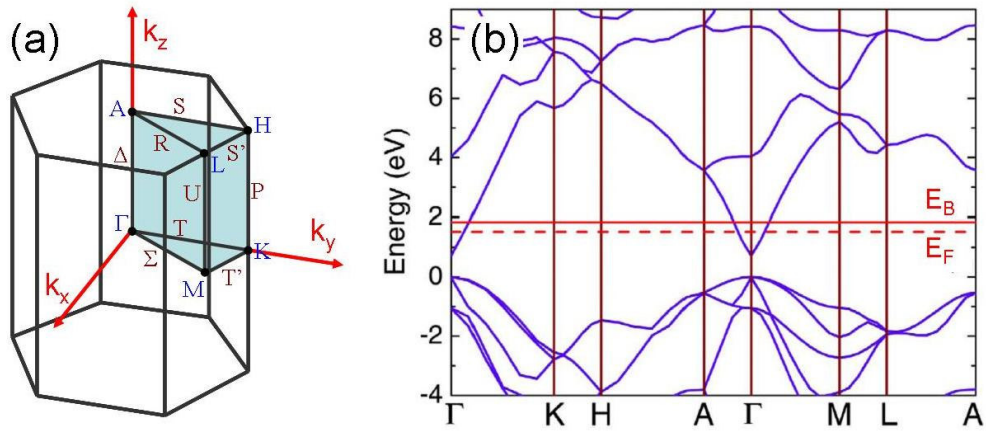


**Figure 2.18.** (a) First Brillouin zone of a *hcp* lattice. (b) QPC-DFT band structure of InN [89].

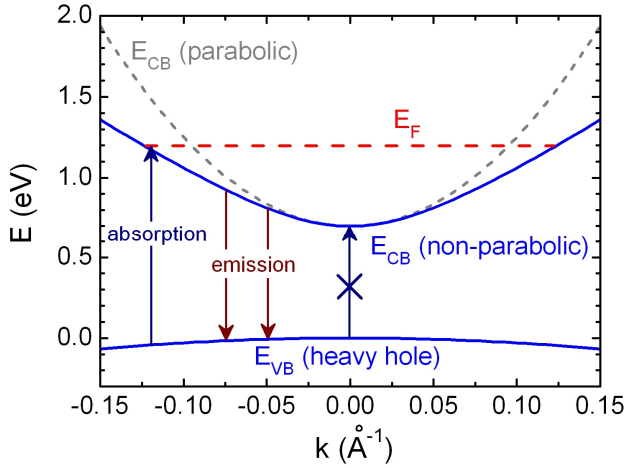


**Figure 2.19.** VB and non-parabolic CB showing the absorption and emission processes.

As shown in equation (2.30), the non-parabolicity is more pronounced for small $E_g$ and/or large $E_P$. At small $\vec{k}$ values (close to the Γ-point), equation (2.30) is simplified into a parabolic band.

InN samples are characterized by the ubiquitous presence of high electron concentrations in a wide range of $10^{17}$-$10^{21}$ $cm^{-3}$, even in not intentionally doped films. Its origin is still under discussion but several candidates have been proposed: unintentional doping, intrinsic defects, dislocations and surface accumulation. This electron concentration shifts the Fermi level into the CB ($E_F$ in Figure 2.18(b)) leading to an onset of the optical absorption which overestimates the fundamental band gap, as it is schematically shown in Figure 2.19 [91]. This phenomenon is known as the Burstein-Moss effect, which is specially pronounced in the case of InN due to the small electron effective mass at the Γ-point. Optical emission below the Fermi level is still possible but significantly broadened. This is the origin of the overestimated band gap of InN in the past years.

**Surface electron accumulation layer**

Another remarkable effect discovered in InN is the presence of an electron accumulation layer (EAL) at its surface, which has been identified by different techniques [92-96]. The existence of the EAL at clean InN surfaces probed by high-resolution electron-energy-loss spectroscopy (HREELS) [94] demonstrates that this effect is an intrinsic property of InN.

The origin of the EAL at InN surfaces can be explained in terms of the electronic band structure [97]. While all other common n-type III-V semiconductors (except InAs)

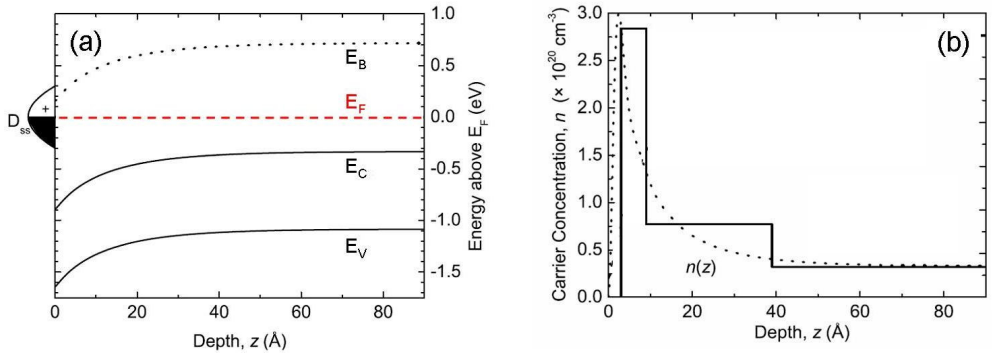


**Figure 2.20.** (a) Conduction and valence band edges ($E_C$ and $E_V$) and the branch point energy ($E_B$) with respect to the Fermi level ($E_F$) in the near surface region of InN (0001) [94]. (b) Calculated charge profile.

have depletion layers at their surfaces, InN presents a surface EAL as a consequence of the low energy of the CBM at the Γ-point compared with the energy at other edge points in the BZ. As a result, the branch-point energy $E_B$, defined as the average midgap energy across the entire BZ ($E_B$ in Figure 2.18(b)), lies above the CBM. The states above the branch-point energy are mainly of CB character (acceptor-type) and the states below it are mainly of VB character (donor-type). Consequently, in InN donor-type surface states exist in the CB. These states can acquire positive charge by emitting their electron into the CB. For the surface states to be neutralized the surface Fermi level must tend toward the branch-point (*pinning*) and the CB and VB bend to generate the space charge required to neutralize the ionized surface states. Then, in the case of positive surface states, CB and VB edges present a downward band bending from the bulk to the surface where the electron accumulation occur. This situation is shown in Figure 2.20(a) for a clean InN (0001) surface, where the CB and VB edges and the branch-point energy with respect to the Fermi level are presented in the near-surface region [94]. The calculated carrier concentration variation is shown in Figure 2.20(b) where a clear enhancement is observed near the surface.

The EAL is a universal feature of InN surfaces as it has been found in wurtzite *c*- and *a*-plane and in zinc-blende surfaces [36]. However, the exact microscopic nature of the surface states, which could vary between different surfaces, is still object of debate. Some proposals have been given as possible origins of the EAL. Based on calculations of the Fermi level pinning in InN, *Segev* and *Van de Walle* [98, 99] suggested the In-In bonds in a surface In adlayer as the responsible of the donor-type surface states. Their calculations show that EAL is intrinsic to polar InN surfaces. It also appears on non-polar ones at high In/N ratio. However, they predict its absence on non-polar InN surfaces at moderate In/N ratios, when the In adlayer is not formed. This has been

experimentally confirmed in *in situ* cleaved *a*-plane InN surfaces [100]. While the as grown *c*-plane and *a*-plane InN surfaces exhibited Fermi level pinning above the CBM, in the cleaved *a*-plane surface it was significantly lower, suggesting the absence of band bending. With these results, it is apparent that the In adlayer on the surface may be a sufficient, but not always necessary, condition for the existence of EAL at InN surfaces. A second alternative that has been recently proposed is found in the *ex situ* oxidized samples. $In_2O_3$ has been shown to exhibit an EAL at its surface [101] as in InN. In this way, the post-growth oxidation of InN samples could lead to the formation of an $In_2O_3$ layer on all kind of surfaces, which would eliminate the In adlayer, becoming then responsible of the EAL even in the non-polar surfaces. Other authors proposed hydrogen as a likely source of donor states in InN [102].

### 2.2.3. Vibrational properties

Properties of interest for device engineering, such as electronic transport, non-radiative electron relaxation processes, etc., can be strongly influenced by phonons. Moreover, the study of the vibrational properties of InN provides information about its crystal structure and quality.

The number of vibrational normal modes (phonons) in a crystal lattice is *3p* for each value of $\vec{k}$, where *p* is the number of ions in the basis [103]. Three of these branches are acoustic and the other 3(*p* - 1) branches are optical. In the case of wurtzite crystals as InN, which have four ions in the unit primitive cell (*p* = 4), there are then 12 vibrational modes or phonons: 3 acoustic and 9 optical.

The wurtzite lattice is one of the simplest structures of uniaxial crystals. It belongs to the space group $C_{6v}^4$ for which the group theory predicts the following lattice phonons [104, 105]:

$$\Gamma_{acoustic} + \Gamma_{optical} = \left(A_1(z) + E_1(x,y)\right) + \left(A_1(z) + 2B_1 + E_1(x,y) + 2E_2\right) \quad (2.31)$$

The letters *x, y, z* describe the phonon polarization direction of the polar modes. The polar modes are longitudinal-optical (LO) when the atoms vibrate in the phonon propagation direction and transverse-optical (TO) when they move in the direction perpendicular to the phonon propagation. While *A* and *B* are one-dimensional irreducible representations, *E* is a two-dimensional one, i.e., $E_1$ and $E_2$ modes are doubly degenerate. Then, considering the phonon propagation along the *c*-axis (*z*-direction), there are two $E_1$(TO) modes (polarized along the *x* and *y* directions), one $A_1$(LO) (polarized along the *z* direction), two $B_1$ (*low* and *high* branches) and four $E_2$ (two for each branch, *low* and *high*).

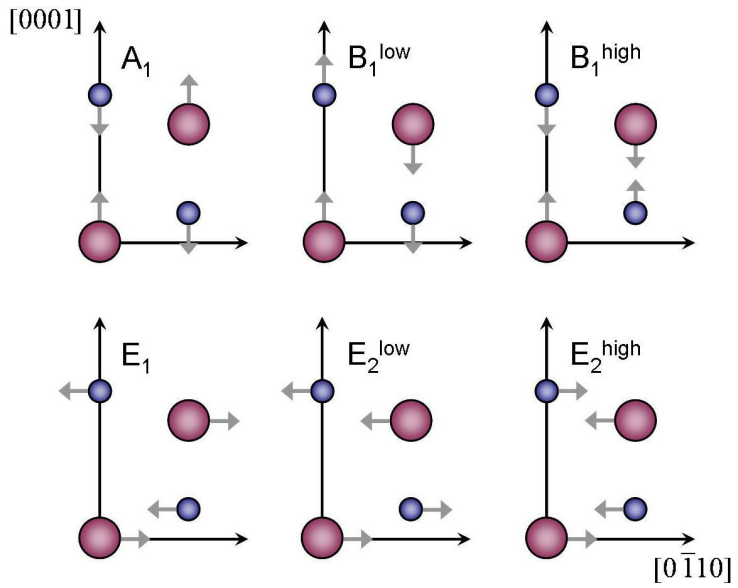


**Figure 2.21.** Atom displacements for the optical modes of the wurtzite structure.

Raman (Section 3.5) and infrared spectroscopy give information about long-wavelength phonons, so that this section will focus on the optical phonon description. The acoustic modes at zero wavevector are just rigid crystal translations. $A_1$ and $E_1$ optical phonons are Raman and infrared active modes, $E_2$ modes are only Raman active and $B_1$ are Raman and infrared inactive (silent modes). The atom displacements for the optical modes are schematically shown in Figure 2.21 [106]. For $A_1$ and $B_1$ symmetries, the atoms move parallel to the *c*-axis, while for $E_1$ and $E_2$ ones, they move perpendicular to it. For $A_1$ and $E_1$ modes, the atoms of the same type move in the same direction. These vibrations produce a net separation of the charge, polarizing the unit cell and creating a long-range electrostatic field. Therefore, $A_1$ and $E_1$ are polar modes.

For an optical phonon which is infrared active (polar phonons: $A_1$ and $E_1$ in InN), the LO and TO components are split in frequency due to the macroscopic electric field associated with the longitudinal phonon (long-range electrostatic field) [104, 107]. Such splitting does not occur for the non-polar modes. In addition, in uniaxial materials a second mechanism has to be considered: the short-range interatomic forces which exhibit the anisotropy of the vibrational force constants. As a result, $A_1$ and $E_1$ modes present different frequencies. Depending on which mechanism dominates, one of the two possible situations shown in Figure 2.22 will occur. For the case of wurtzite materials, the long-range electrostatic forces dominate over the short-range ones and the LO-TO splitting is larger than the $A_1$-$E_1$ splitting (left panel).

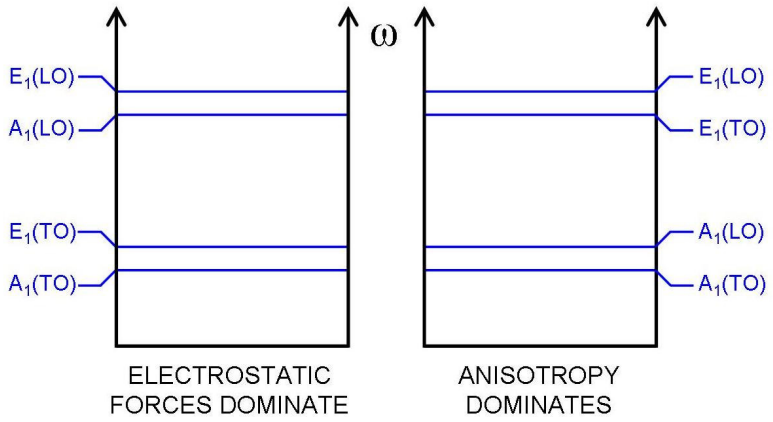


**Figure 2.22.** Schematic level diagram for the two limiting cases: electrostatic forces predominate over the anisotropy in the interatomic forces (left) and viceversa (right).

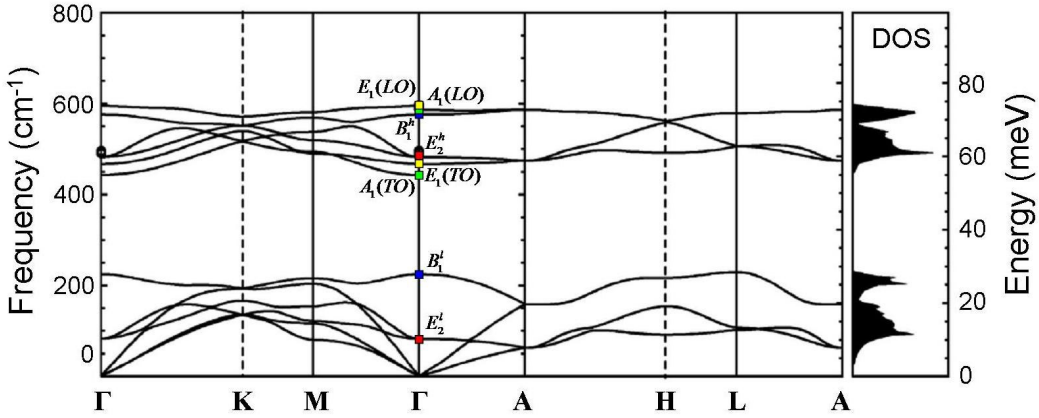


**Figure 2.23.** *Ab initio* phonon dispersion and density of states (DOS) for InN wurtzite structure [108]. The optical phonon modes at the Γ-point are marked by the colour symbols.

Figure 2.23 presents the *ab initio* calculated phonon dispersion curves of InN in the wurtzite structure along several high symmetry lines in the BZ, together with the phonon density of states (DOS) [108]. Each mode is marked in the Γ-point by colour symbols. It can be observed that the acoustic-phonon branches and the low-frequency $B_1$ and $E_2$ optical branches are well separated from the other optical ones. The splittings between the LO and TO modes and between the $A_1$ and $E_1$ symmetries are also observed.

Pure polar phonons are only observed for phonon propagation along the main crystal axes. For other propagation directions, their frequencies exhibit an angular dependence and a mode-mixing may occur [104, 107]. In wurtzite semiconductors, where the electrostatic forces dominate over the anisotropy (left panel in Figure 2.22), a mixing

between $A_1$ and $E_1$ modes may occur while maintaining their pure longitudinal or transverse character, so they are often referred to as quasi-longitudinal and quasi-transverse phonons. Their angular-dependent vibrational frequencies, which are located between the pure $A_1$ and $E_1$ frequencies, are given by:

$$\begin{aligned} \omega_{LO}^2 &= \omega_{A_1(LO)}^2 \cos^2\theta + \omega_{E_1(LO)}^2 \sin^2\theta \\ \omega_{TO}^2 &= \omega_{E_1(TO)}^2 \cos^2\theta + \omega_{A_1(TO)}^2 \sin^2\theta \end{aligned} \tag{2.32}$$

where $\theta$ is the angle between the *c*-axis and the phonon propagation direction and $\omega_{A_1(LO,TO)}$ and $\omega_{E_1(LO,TO)}$ are the frequencies of the pure $A_1$ and $E_1$ modes respectively. For the crystalline structures in which the short-range forces dominate over the long-range ones (right panel in Figure 2.22), the mixing occur between longitudinal and transverse modes with a well-define symmetry. Therefore, they are referred to as quasi-$A_1$ and quasi-$E_1$ phonons.

The frequencies of the pure optical phonons can be experimentally determined by Raman spectroscopy. However, large variations are found in the literature which can be due to the differences in strain, presence of structural defects, etc. Some of the reported frequencies of InN Raman active modes are presented in Table 2.3.

| Ref. | $A_1$(TO) | $A_1$(LO) | $E_1$(TO) | $E_1$(LO) | $E_2^{low}$ | $E_2^{high}$ | $B_1^{low}$ | $B_1^{high}$ |
|---|---|---|---|---|---|---|---|---|
| | experiment | | | | | | | |
| [109] | 447 | 586 | 476 | 593 | 87 | 488 | 220 | 565 |
| [110] | 480 | 580 | 476 | 570 | 87 | 488 | 200 | 540 |
| [111] | 440 | 590 | | | 88 | 490 | | |
| [112] | 445 | 588 | 472 | | | 488 | | |
| [113] | 443 | 590 | 477 | | | 491 | | |
| | calculation | | | | | | | |
| [111] | 443 | 589 | 470 | 605 | 93 | 492 | 202 | 568 |
| [112] | 440 | | 472 | | 104 | 483 | 270 | 530 |
| [108] | 443 | 586 | 467 | 595 | 83 | 483 | 225 | 576 |

**Table 2.3.** Experimental and calculated frequencies ($cm^{-1}$) of optical phonons of wurtzite InN.

### 2.2.4. LO phonon-plasmon coupling

Coupling of the LO phonons to the collective oscillations of the free carriers (plasmons) occurs when an appreciable free-carrier concentration is present in a polar semiconductor [114]. The coupling occurs via the macroscopic longitudinal electric field which is set up by the relative longitudinal displacement of the positive and negative ions and by the longitudinal displacements of the free carriers relative to the static charges of opposite sign.

The dielectric function of polar crystals on the basis of the Drude model (valid for small wavevectors), with both phonon and carrier contributions, is given by [115, 116]:

$$\varepsilon(\omega) = \varepsilon_\infty \left( 1 + \frac{\omega_{LO}^2 - \omega_{TO}^2}{\omega_{TO}^2 - \omega^2 - i\omega\Gamma} - \frac{\omega_p^2}{\omega(\omega + i\gamma)} \right) \tag{2.33}$$

where $\omega_{LO}$, $\omega_{TO}$ and $\omega_p$ are the frequencies of the longitudinal and transverse phonons and the uncoupled plasmon, respectively. $\varepsilon_\infty$ is the optical dielectric constant and $\gamma$ and $\Gamma$ are the plasmon and phonon damping constants respectively. The plasmon frequency is given by [103]:

$$\omega_p = \sqrt{\frac{4\pi n e^2}{m^* \varepsilon_\infty}} \tag{2.34}$$

where $n$ is the carrier concentration, $e$ is the electric charge and $m^*$ is the effective mass of the free-carriers.

The LO-plasmon coupling results in two new modes denoted by $L^\pm$ (upper and lower branches), whose frequencies strongly depend on the free-carrier concentration and can be obtained from the roots of equation (2.33) ($\varepsilon(\omega_\pm) = 0$). In the absence of damping, the $\vec{q} \approx 0$ frequencies of the two coupled modes are given by [114]:

$$\omega_\pm^2 = \frac{1}{2}\left[ \left(\omega_{LO}^2 + \omega_p^2\right) \pm \sqrt{\left(\omega_{LO}^2 + \omega_p^2\right)^2 - 4\omega_{TO}^2\omega_p^2} \right] \tag{2.35}$$

These frequencies are plotted in Figure 2.24 as a function of the carrier concentration for the $E_1$(LO) mode of InN. At low carrier concentration, $L^-$ mode shows plasmon behaviour, while $L^+$ behave like a phonon with its frequency close to that of the uncoupled LO phonon. At high carrier concentration, their character is reversed. $L^-$ exhibits a phonon like behaviour whose frequency approaches that of the uncoupled TO phonon, while $L^+$ shifts to higher frequencies and becomes plasmon-like. This means that the electric field of LO phonon is nearly completely screened by free carriers. A similar trend would be observed for the $A_1$(LO) phonon-plasmon coupled modes.

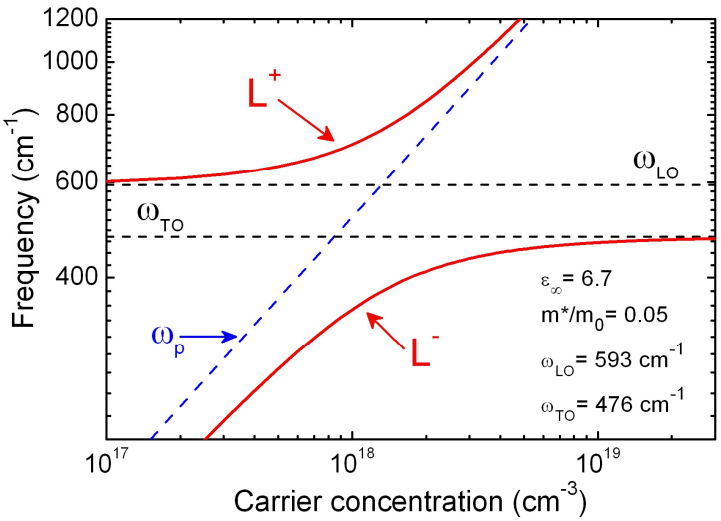


**Figure 2.24.** Carrier concentration dependence of the LO phonon-plasmon coupled modes in wurtzite InN.

These coupled phonon-plasmon modes may be observed by Raman scattering, so providing information about the free-carrier density. They obey the same polarization selection rules as the uncoupled LO phonons [117]. Raman studies have been done in InN films where the lower branch $L^-$ has been observed coexisting with the uncoupled LO phonon [109, 118]. Both branches have been found, for example, in GaN crystals [119].

The situation described above is valid only for small values of the damping constants and vanishing wavevectors. When these conditions are not fulfilled, equation (2.35) is not applicable and the spectra cannot be analyzed in terms of $L^{\pm}$ coupled modes. For a given carrier density, the $L^+$ mode shifts to higher frequencies with increasing wavevector $\vec{q}$ and becomes overdamped when entering the free-particle excitation regime. The $L^-$ mode also shifts to higher frequency and approaches $\omega_{LO}$ within the free-particle excitation spectrum. Consequently, wavevector non-conservation in overdamped plasmas may result in a broad plasmon-related band in the Raman spectra covering the whole dispersion of the $L^-$ mode between $\omega_{LO}$ and $\omega_{TO}$ [120].

### 2.2.5. InN nanocolumns

InN nanocolumns (NCs) grown by molecular beam epitaxy (MBE) have been proven to be defect and strain free, which makes them ideal candidates to study fundamental properties of InN. In particular, they offer the possibility of studying InN properties, as the EAL, on high quality non-polar surfaces. In addition, they are interesting among

group-III nitrides due to their potential applications in optoelectronic devices extending the spectral range to the visible and infrared. In fact, $In_xGa_{1-x}N$ NCs have been grown across the entire compositional range from x = 0 to 1 with tunable emission from the near-ultraviolet to the near-infrared region [121].

**Growth mechanism**

High quality InN layers are difficult to grow due mainly to two factors: the low dissociation temperature of InN and the lack of suitable substrates [86]. The former problem can be avoided by using low temperature crystal growth techniques as MBE. The latter has been partially solved using different types of buffer layers in order to accommodate the lattice mismatch between InN and the available substrates. However, a rather high dislocation density is almost unavoidable. An interesting alternative is found in InN NCs which are found to be defect and strain-free [32, 33].

InN grows in a columnar shape under special conditions of substrate temperature and III/V molecular flux ratio [32-34, 122, 123]. Both parameters are not independent and a slight change in the growth temperature can affect the III/V ratio. The most critical parameter to grow InN is the substrate temperature, which has to be determined before adjusting the III/V ratio. Substrate temperatures above 500ºC for In-polarity and 600ºC for N-polarity [124, 125] lead to the dissociation of the InN layer and the formation of metallic In droplets on the surface. Then, the III/V ratio determines the morphology of the layer. N-rich conditions lead to columnar InN samples (Figure 2.25(a)) while conditions close to stoichiometry lead to compact layers (Figure 2.25(b)). The precise choice of all the involved parameters will determine the density and average diameter of the NCs [126]. The use of AlN buffer layers is found to be essential to improve the crystal quality of the NCs [33, 34]. Although MBE is the most extended technique in the NC fabrication, other methods as catalytic chemical vapour deposition can be employed [127].

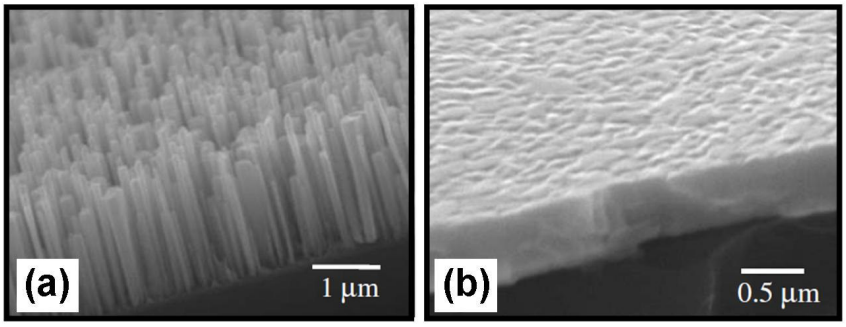


**Figure 2.25.** SEM images of (a) InN NCs and (b) InN compact sample [32].

InN NCs have been grown on different substrates as Si (111) [32, 34, 123], Si (100) [126] and GaN (0001) [125]. In all cases, the NCs were grown along the *c*-axis with a hexagonal cross-section, having non-polar (*m*-plane) sidewalls, as is schematically shown in Figure 2.16. InN NCs grown along the *a*-axis have been recently obtained using *a*-plane GaN substrates [128]. More details about these NCs will be given in Chapter 5. In this section we will focus only on hexagonal InN NCs.

**Raman spectra of InN nanocolumns**

Raman spectroscopy is a powerful tool to evaluate the crystalline quality and to investigate other properties of InN NCs as the EAL at their lateral surfaces [129, 130].

Figure 2.26 shows the Raman spectra recorded in backscattering configuration $z(x,-)\overline{z}$ ($z$ parallel to *c*-axis) for a compact InN layer and a InN NC-sample [131]. Several peaks have been identified as vibrational modes of InN. The narrow $E_2$ mode in both spectra indicates high crystalline quality. The first important difference is found in the LO phonon. While the compact sample shows the allowed $A_1$(LO) phonon, the NC spectrum presents the $E_1$(LO) one, which is a forbidden symmetry in this scattering configuration. The same behaviour has been reported by other authors [130] and for GaN NCs [132]. An explanation was given in terms of light refraction and scattering by the inhomogeneous NC size and height distribution. As a result of the light scattering due to the surface roughness and the high refraction index of InN (2.9), most of the light enters through and scatters from the lateral surfaces of the NCs, perpendicularly to the *c*-axis, even when the illumination is parallel to it. This argument was confirmed by measurements in $x(y,-)\overline{x}$ configuration where the $E_1$(LO) mode appeared in both samples.

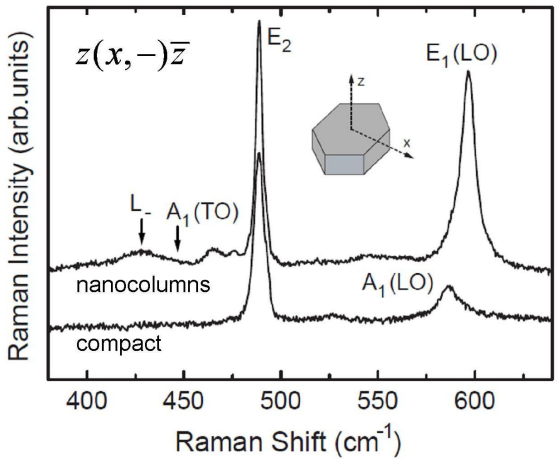


**Figure 2.26.** Room-temperature Raman spectra of a compact layer and a NC sample for backscattering configuration along *c*-axis [131]. The inset shows the scattering directions.

**Surface electron accumulation layer**

The peak observed at 429 $cm^{-1}$ (below $A_1$(TO) frequency) in Figure 2.26 was attributed to the low-energy branch $L^-$ of the LO phonon-plasmon coupled mode. Similar frequencies of this mode have been reported in InN thin films [109, 118] and in NC-samples [123, 130]. The absence of this peak in the compact layer is probably due to its lower specific surface. The observation of the $L^-$ mode confirms the presence of an EAL at the lateral surfaces of the NCs (non-polar surfaces). Therefore, the coupled $L^-$ mode comes from the lateral surfaces of the NCs while the uncoupled $E_1$(LO) arises from the inner part. The electron density calculated from the $L^-$ frequency was around $2.8x10^{18}$ $cm^{-3}$.

Transport measurements have also been performed in single InN NCs [133, 134]. The accumulation of electrons at the lateral non-polar surfaces of InN nanowires was suggested in [133] where a very high conductance was observed in single InN nanowires compared with GaN ones. This effect was explained by the different surface Fermi level pinning leading to surface depletion and accumulation for GaN and InN respectively, as it is illustrated in Figure 2.27. Clearer evidence of the EAL on the sidewalls of InN NCs was reported by *Calleja et al.* [134] showing a linear dependence in the conductivity of single InN NCs as a function on the reciprocal diameter. This indicates a dominant effect of the surface conductivity for small NC diameters.

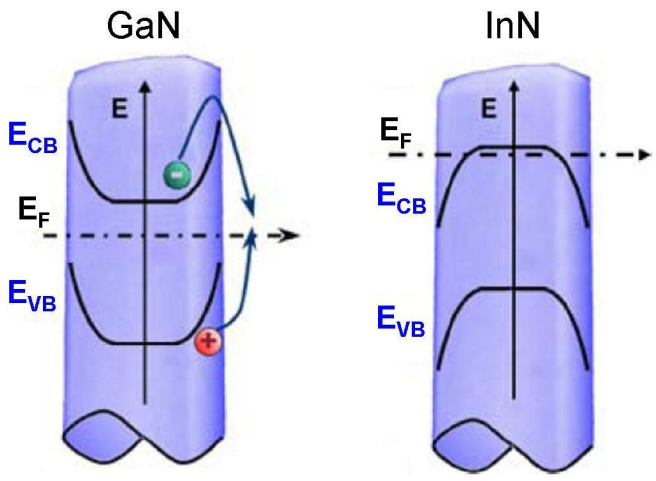


**Figure 2.27.** Band scheme of a single GaN (left) and InN (right) NC.

**Photoluminescence measurements**

The reported low temperature band gap energies for InN NCs go from 0.685 eV to 0.78 eV [123, 129, 130, 135]. In all cases, a stronger Burstein-Moss shift is observed in the NCs emission than in the bulk InN samples studied, which is attributed to the difference in their surface to volume ratios. In some cases, an anomalous blueshift has been observed in the PL emission energy by increasing the sample temperature [123], which can be explained in terms of surface EAL as follows [130]. The probability of radiative recombination is proportional to the spatial overlap of the electron and hole wavefunctions. Therefore, due to the band bending depth profile of the CBM and VBM (see Figure 2.27), three different regions can be identified inside a NC:

(1) the NC core where the photogenerated electrons will move fast to the NC surface.
(2) the most external region, close to the surface, where photogenerated holes will move inwards.
(3) an intermediate region populated by both electrons and photogenerated holes.

Obviously, the last region is the most active from the optical point of view. By increasing the sample temperature, photoholes can spread over a wider region penetrating deeper into the EAL. This should induce a blueshift which compensates or even dominates over the normal redshift due to the temperature dependence of the band gap.

# Chapter 3

# Experimental Techniques

Optical spectroscopy is nowadays a powerful tool for material characterization, as it provides information about their electronic and vibrational properties. It allows the investigation of the light-matter interaction. The fundamental processes which can occur when matter is illuminated are:

**Absorption:** transition from an electronic level to another of higher energy with energy transfer from the radiation to the material.

**Emission or non-radiative relaxation:** transition from a higher energy level to a lower energy one. This transition can occur by emitting radiation or not, which leads to emission or non-radiative relaxation respectively.

**Scattering:** energy and momentum exchange between radiation and matter without absorption and emission of light by the material. If incident and scattered photons have the same energy we talk of elastic scattering (Rayleigh). The opposite case is known as inelastic scattering.

The combination of spectroscopic and microscopic techniques, as *high-resolution transmision electron microscopy* (HR-TEM), leads to a deeper knowledge of the material properties. In this Thesis several experimental methods have been used to determine the optical and structural properties of the studied nanostructures.

This chapter presents an overview of different techniques and the main experimental setups needed to carry them out. The first six sections are dedicated to the optical characterization techniques and their setups and the last one to HR-TEM.

## 3.1. Photoluminescence spectroscopy

The term luminescence includes all type of light emission appearing as a consequence of some input of energy into the sample (excitation of the sample). Depending on the excitation method, we talk of photoluminescence (light absorption), electroluminescence (electric field application), cathodoluminescence (electron bombardment), thermo-luminescence (heating of the sample), etc. Photoluminescence (PL) is the most widely used technique for the investigation of the optical transitions in the band structure of semiconductors.

The basic operation principle of the photoluminescence process [136, 137] is shown in Figure 3.1(a). An incident photon of energy higher than the bandgap can excite an electron from the valence band (VB) to the conduction band (CB), leaving a hole in the VB. Electron and hole (*e-h*) pairs then relax non-radiatively until the lowest available energy state and, finally, they recombine radiatively resulting in photoluminescence emission. Depending on the origin of the involved energy levels mentioned before (band edge, impurities …), different transitions (some illustrated in Figure 3.1(b)) can be observed:

- $E_{BB}$ = *Band-band transition*: from CB to VB
- $E_{FB}$ = *Free-to-bound transition*: from a donor to the VB or from the CB to an acceptor.
- $E_{DA}$ = *Donor-acceptor pair transition*
- $E_{FX}$ = *Free-exciton emission*: radiative annihilation of electrons and holes attracted to each other by the Coulomb interaction to form an exciton. For high-quality semiconductors, the emission of excitonic states lies just below the energy gap.
- $E_{BX}$ = *Bound-exciton emission*: in semiconductors containing donor or acceptor states, excitons can be bound to the impurities via van der Waals interaction which lowers the exciton energy.

More information about those transitions can be found in [136].

In a wide part of this Thesis, we study the photoluminescence of self-assembled InAs/GaAs quantum rings (QRs). In that case, the three-dimensional confinement of the InAs in the GaAs barriers forms an effective attractive potential for the electrons and holes. So that, for defect- and impurity-free semiconductors, the electronic levels in this potential become the lowest available energy states in the non-radiative relaxation process, from which they recombine optically.

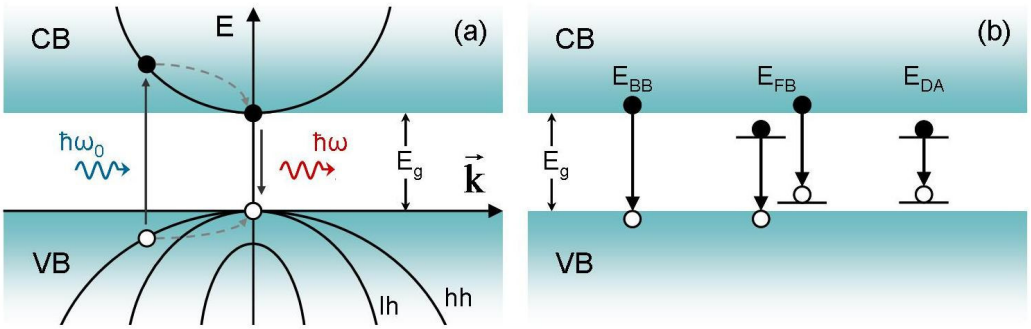


**Figure 3.1.** (a) Photoluminescence operation principle. (b) Schematic diagram of possible radiative transitions in a semiconductor.

## 3.2. Photoluminescence excitation spectroscopy

In photoluminescence, in general, the emitted light corresponds to the lowest energy levels of the sample. So that only partial information can be extracted from this technique. With this in mind, absorption would give a more complete analysis of the sample. However, the study of the light absorbed by certain materials is not possible due to their opacity, which would require the use of very thin samples, or due to the opaque substrates. A versatile technique that is used instead of absorption is the so-called photoluminescence excitation (PLE) spectroscopy [136, 137]. The principle is the following: one records the emission intensity of a certain transition ($\hbar\omega$ in terms of Figure 3.1(a)) while varying the photon energy of the excitation ($\hbar\omega_0$) at a constant incident excitation intensity. The PLE spectra of nanostructures usually exhibit peaks, which indicate that the emission is strongly excited at certain photon energies. These energies correspond to absorption transitions to excited states from where relaxation to the ground state is efficient. Therefore, the PLE spectrum is "somehow" related to the absorption spectrum. In this section, we examine the conditions under which this assumption is valid.

The relation between the emission intensity $I_{em}$ and the excitation intensity $I_{ex}$ is:

$$I_{em} = P_{abs} \, \mathrm{P}_{rel} \, P_{em} I_{ex} \tag{3.1}$$

where $P_{abs}$, $P_{rel}$ and $P_{em}$ denote, respectively, the probability of absorption of the incident photon by the sample, the probability of the *e-h* pair relaxation to the emitting state and the probability of radiative recombination after relaxation. While $P_{em}$ can be assumed to be constant at fixed temperature, $P_{rel}$ depends strongly on the electron-phonon interaction, the main relaxation mechanism in defect-free semiconductors. The equivalence between PLE and absorption relies on the assumption that the

recombination times are much larger than the intraband relaxation ones, i.e., the *e-h* pairs have enough time to relax completely before radiative recombination. This condition can be considered true in high quality semiconductors based on GaAs and related III-V compounds, in which the scattering by phonons occurs on picosecond and subpicosecond time scales, significantly shorter than the radiative lifetime.

## 3.3. Time-correlated single-photon counting

The processes of absorption, non-radiative relaxation and emission shown in Figure 3.1(a) occur in a time domain depending on the material under study. Time-resolved spectroscopy focuses on the time evolution of these processes to obtain information about the dynamics of an optical transition. Time-correlated single-photon counting (TCSPC) is one of the most widely used techniques for time-resolved emission measurements in nano- and sub-nanosecond scales. In this section, general principles of TCSPC are given. More information about this technique can be found in [138-140].

The sample is excited by a pulsed laser source and the PL is collected by a detector working in photon counting mode. Typically one can employ an avalanche photodiode (APD) for the detection of the signal, which delivers electric pulses for individual photons. The basic principle for TCSPC is schematically shown in Figure 3.2. A laser pulse excites the sample at $t=t_0$. The excitation pulse is divided into two beams, one to excite the sample and the other is sent to a second APD where the *start* pulse is generated. The *start* signal is sent to a *time-to-amplitude converter* (TAC). After the *start* pulse, the first photon arriving at the first APD generates a *stop* signal which is sent to the TAC. Thus, the TAC records the time interval $\Delta t$ between the absorption of the photon by the sample at $t=t_0$ and the emission of a photon. Then, after many events collected, the system measures the number of signal pulses in each time-delay interval and storages each result in a histogram describing the PL decay. This last step is done by a *multichannel analyzer* (MCA).

Some clear advantages are found in the TCSPC technique. First of all, it presents a very high time resolution. It is limited by the laser pulse duration and by the response time of the electronic devices. Secondly, very low emission intensity is enough to obtain a decay profile. This is very important because weak excitation pulses can be used to obtain the time resolved spectra of samples that cannot emit many photons after each excitation pulse. In particular, this method allows carrying out studies of lifetimes in single photon emitters. Another advantage of the TCSPC method is its high accuracy due to the photon counting technique, which can give lifetimes with 99% accuracy or better.

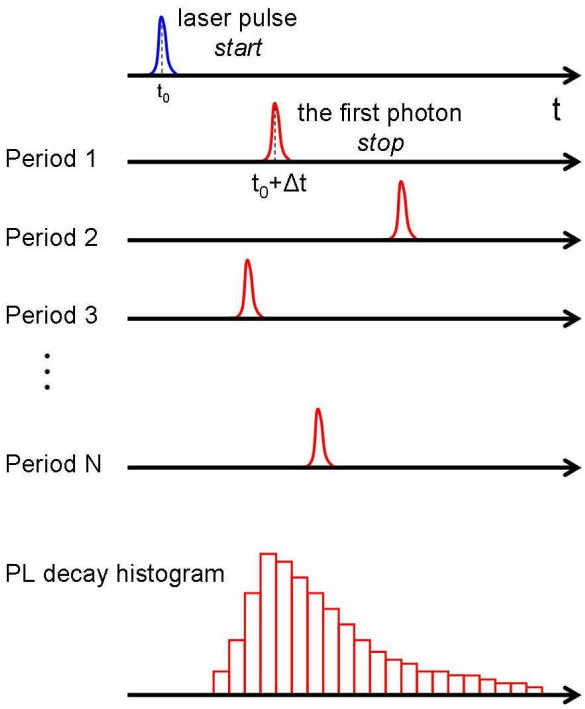


**Figure 3.2.** Basic principle of TCSPC method.

If the PL originates from only one excited state, the decay signal can be fitted with an exponential curve of the form:

$$I(t) = I_0 \exp\left(\frac{t - t_0}{\tau}\right) \tag{3.2}$$

where τ is the lifetime of the state under study. If there is more than one contribution, the superposition of several exponential functions can be used.

## 3.4. Photon correlation measurements

Quantum optical techniques exploit the consequences of considering a beam of light as a stream of photons rather than a classical wave. In this section, the basic concepts of quantum optics are discussed starting with the classification of light according to the photon statistics. Afterwards, the second-order correlation function is presented giving rise to a second classification of the light. Then, the measurement of the intensity correlation function provides information about the nature of the light. Further detailed information about the quantum theory of light can be found in [8, 11, 41, 141, 142].

### 3.4.1. Photon statistics

Consider a light beam with a well-defined average photon flux. Due to the discrete nature of photons, the photon number fluctuates on a short time scale. These fluctuations are described by the photon statistics of the light. Different light fields can be characterized by their specific photon number fluctuations.

In classical physics, the most stable type of light that we can imagine is a perfectly coherent monochromatic wave with constant intensity, which can be, for example, a laser operating well above threshold. In that system, the photon number probability is described by the *Poisson distribution*:

$$P(n) = \frac{\langle n \rangle^n}{n!} e^{-\langle n \rangle} \tag{3.3}$$

where $\langle n \rangle$ is the mean photon number. The fluctuations of a statistical distribution about its mean value are usually quantified in terms on the variance, which in this case is:

$$\Delta n = \sqrt{\langle n \rangle} \tag{3.4}$$

This shows that the relative size of the fluctuations decreases as $\langle n \rangle$ gets larger.

Compared to the coherent state, there are three possibilities according to the variance of the photon number distributions:

- *super-Poissonian* statistics: $\Delta n > \sqrt{\langle n \rangle}$
- *Poissonian* statistics: $\Delta n = \sqrt{\langle n \rangle}$
- *sub-Poissonian* statistics: $\Delta n < \sqrt{\langle n \rangle}$

It is clear that distributions for *super-Poissonian* and *sub-Poissonian* light are broader or narrower than the Poisson distribution respectively. It is not difficult to think of the types of light that would be expected to have *super-Poissonian* statistics. Since a perfect stable intensity gives *Poissonian* statistics, all classical light with time-varying light intensities will have *super-Poissonian* distribution. Two examples are thermal light from a black-body source and chaotic (partially coherent) light, for example, from a discharge lamp. On the other hand, *sub-Poissonian* light is somehow more stable than perfectly coherent light and has no classical equivalent. Therefore, the observation of *sub-Poissonian* statistics is a clear evidence of the quantum nature of light. Table 3.1 gives a summary of the classification of light according to the photon statistics.

| **Photon statistics** | **Classical equivalents** | **I(t)** | $\Delta n$ |
|---|---|---|---|
| Super-Poissonian | chaotic, incoherent, thermal light | Time-varying | $> \sqrt{\langle n \rangle}$ |
| Poissonian | perfectly coherent light | Constant | $\sqrt{\langle n \rangle}$ |
| Sub-Poissonian | none (non-classical) | Constant | $< \sqrt{\langle n \rangle}$ |

**Table 3.1.** Classification of light according to photon statistics.

### 3.4.2. Second order correlation function

To quantify the intensity fluctuations of a light source it is necessary to evaluate the so-called second-order correlation function which is classically defined as:

$$g^{(2)}(t_1,t_2) = \frac{\left\langle E^*(t_1)E^*(t_2)E(t_2)E(t_1)\right\rangle}{\left\langle E^*(t_1)E(t_1)\right\rangle\left\langle E^*(t_2)E(t_2)\right\rangle} = \frac{\left\langle I(t_1)I(t_2)\right\rangle}{\left\langle I(t_1)\right\rangle\left\langle I(t_2)\right\rangle} \tag{3.5}$$

where $E(t_i)$ and $I(t_i)$ are the electric field and the intensity of the beam at time $t_i$. The brackets indicate the time average computed by integrating over a long time period.

For light sources with stationary statistics, the average in equation (3.5) does not depend on the particular starting time $t_1$ and the correlation is only a function of the delay time $\tau = t_2 - t_1$:

$$g^{(2)}(\tau) = \frac{\left\langle E^*(t)E^*(t+\tau)E(t+\tau)E(t)\right\rangle}{\left\langle E^*(t)E(t)\right\rangle^2} = \frac{\left\langle I(t)I(t+\tau)\right\rangle}{\left\langle I(t)\right\rangle^2} \tag{3.6}$$

The time-scale of the intensity fluctuations is determined by the coherence time $\tau_c$ of the source. If $\tau >> \tau_c$, the intensity fluctuations at times $t$ and $t+\tau$ will be completely uncorrelated with each other. That means that:

$$g^{(2)}(\tau >> \tau_c) = \frac{\left\langle I(t)I(t+\tau)\right\rangle}{\left\langle I(t)\right\rangle^2} = \frac{\left\langle I(t)\right\rangle^2}{\left\langle I(t)\right\rangle^2} = 1 \tag{3.7}$$

On the other hand, if $\tau << \tau_c$, there will be correlations at the two times. In particular, if $\tau = 0$, we have:

$$g^{(2)}(0) = \frac{\left\langle I(t)^2\right\rangle}{\left\langle I(t)\right\rangle^2} \tag{3.8}$$

It can be shown that for any classical time dependence $I(t)$, the case will always be that:

$$\begin{aligned} g^{(2)}(0) &\geq 1 \\ g^{(2)}(0) &\geq g^{(2)}(\tau) \end{aligned} \tag{3.9}$$

The definition in equation (3.6) can be treated more generally considering the scalar electric field operator of a single mode with frequency ω and wavevector $\vec{k}$ parallel to the z-direction, given by:

$$\hat{E}(\chi) = E_0 \left\{ \hat{a} e^{-i\chi} + \hat{a}^{\dagger} e^{i\chi} \right\} \tag{3.10}$$

where $\chi = \omega t - kz - \pi/2$ is the phase angle and $\hat{a}$ and $\hat{a}^{\dagger}$ are the annihilation and creation operators. It can be demonstrated [141] that equation (3.6) can be rewritten in terms of $\hat{a}$ and $\hat{a}^{\dagger}$ as follows:

$$g^{(2)}(\tau) = \frac{\left\langle \hat{a}^{\dagger}(t)\hat{a}^{\dagger}(t+\tau)\hat{a}(t+\tau)\hat{a}(t) \right\rangle}{\left\langle \hat{a}^{\dagger}(t)\hat{a}(t) \right\rangle^2} \tag{3.11}$$

If we consider a beam of light as a stream of photons, $g^{(2)}(\tau)$ gives the probability of detecting a photon at a time $t+\tau$, given that a previous photon has been measured at time *t*. Thus, for $\tau = 0$, $g^{(2)}(\tau)$ gives the probability of detecting two photons at the same time. This can lead to results without classical analogue. Let us consider a stream of photons with long time intervals between successive photons. It is clear that no events are expected at $\tau = 0$, which contradicts the classical result given in equation (3.9). This situation is known as *antibunching*. On the contrary, if we now consider a light source with photons arriving in bunches, there will be many events near $\tau = 0$ and fewer at later times, which is compatible with equation (3.9). This situation is known as *bunching*. These results allows a new classification of the light according to the value of $g^{(2)}(0)$, which is summarized in Table 3.2. Once more, as occurred with *sub-Poissonian* statistics, antibunched light has no classical equivalent. It is now worthy to emphasize that photon *antibunching* and *sub-Poissonian* statistics are two different quantum optical phenomena and although it is frequent that non-classical light shows both at the same time, the two effects are different and need not to occur together [142].
The first experimental demonstration of photon *antibunching* was made by *Kimble et al.* in 1977 [143] using the light emitted by an individual sodium atom. Once a photon has been emitted, the atom needs some time before the next photon can be emitted. This time is approximately equal to the radiative lifetime of the transition.

An application of the generation of antibunched light is the development of single-photon emitters. As explained in Chapter 1, these sources are needed, for example, to improve the security in quantum cryptography experiments.

| **Photon stream** | **Illustration** | **Classical description** | $g^{(2)}(0)$ |
|---|---|---|---|
| bunched | •••• ••• •••• ••• | chaotic | >1 |
| random | • •• • •• •• • • • | coherent | 1 |
| antibunched | • • • • • • • • • | none | <1 |

**Table 3.2.** Classification of light according to the value of $g^{(2)}(0)$.

### 3.4.3. Photon auto-correlation measurements

In the previous section we have considered the correlation of a beam with itself. In this particular case, the quantity $g^{(2)}(\tau)$ is known as the second-order *auto*-correlation function. The classic photon correlation experiment records a histogram of the time intervals between the photons of the investigated signal. If the times involved are in the nanosecond and picosecond-scale, the experiment cannot be performed with only one detector due to the dead time, which in an APD is of the order of tens of nanoseconds. This problem is avoided by using a *Hanbury-Brown and Twiss* (HBT) interferometer, whose setup is schematically shown in Figure 3.3. Photons of the incident signal are split on a non-polarizing 50/50 beam-splitter and directed onto two photodetectors. The operation principle is quite similar to the TCSPC technique. The time difference between the detection events (*start* and *stop*) is registered and, in a subsequent process, a histogram of coincidence events as a function of time delay is performed by the TAC

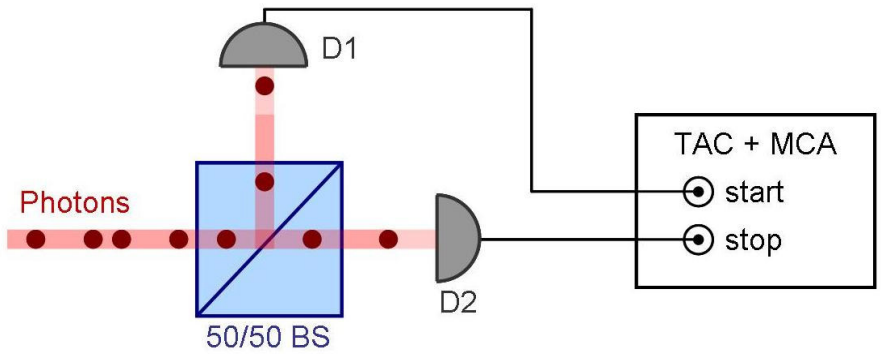


**Figure 3.3.** HBT interferometer setup.

and the MCA. Because separate detectors are used for *start* and *stop*, there is no problem with detector dead time. Moreover, this setup can be used with continuous and pulsed excitation sources.

The measured histogram of coincidence counts approaches the unnormalized second-order correlation function ($G^{(2)}(\tau) = C \cdot g^{(2)}(\tau)$ where $C$ is the average coincidence counts) in the limit when the dark count rate $R_{dark}$ is much smaller than the signal count rate $R$ and when the average arrival time of the photons $1/R$ is much smaller than the observed delay time $\tau$. Normalization of $G^{(2)}(\tau)$ can be achieved by considering a Poisson light source with the same average detector count rate. For such a source, the experimental expectation values of coincidence counts under either pulsed or continuous excitation can be estimated directly from:

$$\begin{aligned} C_{Poisson}^{pulsed} &= R_{start} R_{stop} \Delta t_{laser} t_{\text{int}} \\ C_{Poisson}^{cw} &= R_{start} R_{stop} \Delta t_{res} t_{\text{int}} \end{aligned} \tag{3.12}$$

where $R_{start}$ and $R_{stop}$ are the detector count rates, $t_{int}$ the total integration time, and $\Delta t_{laser}$, $\Delta t_{res}$ are the laser pulse repetition period and the time resolution (binning) respectively.

In the field of semiconductor quantum optics, the measurement of $g^{(2)}(\tau)$ has become a powerful tool for identifying single photon emitters. This has been the case of QDs, which, as individual atoms, exhibit a high degree of antibunching at zero delay time. When the experiment is performed under continuous excitation, $g^{(2)}(\tau)$ is found to follow the next exponential dependence at both sides of $\tau = 0$:

$$g^{(2)}(\tau) = 1 - \exp\left(-\frac{|\tau|}{\tau_r}\right) \tag{3.13}$$

where $\tau_r$ is the antibunching time, which tends to the radiative lifetime of the QD transition in the limit of weak excitation.

### 3.4.4. Photon cross-correlation measurements

In some cases it can be very interesting to study the correlation of two different light sources, *a* and *b*. In this case, the equation (3.11) can be generalized as follows:

$$g_{ab}^{(2)}(\tau) = \frac{\left\langle \hat{a}_a^\dagger(t)\hat{a}_b^\dagger(t+\tau)\hat{a}_b(t+\tau)\hat{a}_a(t)\right\rangle}{\left\langle \hat{a}_a^\dagger(t)\hat{a}_a(t)\right\rangle\left\langle \hat{a}_b^\dagger(t)\hat{a}_b(t)\right\rangle} \tag{3.14}$$

This is known as photon *cross*-correlation. A typical example related with QDs is the cross-correlation measurement of the biexciton (XX) and exciton(X) emission from a single QD, which proves sequential emission in the XX-X transition cascade. In that

case, $g^{(2)}(\tau)$ give the probability of detecting a X photon at time $t+\tau$ upon detection of a XX photon at time *t*.

Experimentally, the HBT setup has to be implemented by separating the two emission lines of the QD and directing each one to a different detector. The TAC-MCA system constructs a histogram of coincidence events as a function of delay time τ just as explained in the previous section. In the case of XX-X cross-correlation, the histogram presents an asymmetric shape around $\tau = 0$, which will be discussed in detail in Chapter 4.

## 3.5. Raman spectroscopy

Most of the light traveling through a medium is transmitted or absorbed following the standard laws of reflection and refraction (which result from $\vec{k}$-conservation). However, light can be also scattered in all directions. Raman spectroscopy is based on the inelastic scattering of light by elementary excitations inside the medium. The origin of these excitations can be electronic, magnetic or vibrational depending on the quasi-particle involved in the process (electronic excitations, magnons or phonons respectively). The purpose of this section is to give a simplified insight on the Raman scattering process and its selection rules. More information about Raman scattering can be found in [136, 144-146].

In this Thesis, we will mainly focus on the Raman effect caused by lattice vibrations, which consists, in its first-order version, of the inelastic scattering of a photon with well-defined energy and momentum by a phonon of energy $\hbar\omega_q$ and wavevector $\vec{q}$ that is excited or absorbed in the process. The energy and momentum of the scattered photon are given by:

$$\begin{aligned} \hbar\omega_s &= \hbar\omega_i \pm \hbar\omega_q \\ \vec{k}_s &= \vec{k}_i \pm \vec{q} \end{aligned} \tag{3.15}$$

where the *i* and *s* subindexes are referred to incident and scattered photons, respectively. If the scattered photon is observed at a frequency that is lower than that of the incident one, the process is known as *Stokes Raman scattering*. On the other hand, if the scattered photon is the more energetic of the two, we talk of *anti-Stokes Raman scattering*. The process is schematically illustrated in Figure 3.4, where it has been included the fact that the *anti-Stokes* processes are less probable (so their scattering intensity is lower) than the *Stokes* ones, since they require the previous existence of phonons in the material. The Raman frequencies can be measured relative to that of the excitation. Thus, the origin of the abscissa scale can be placed at the position of the

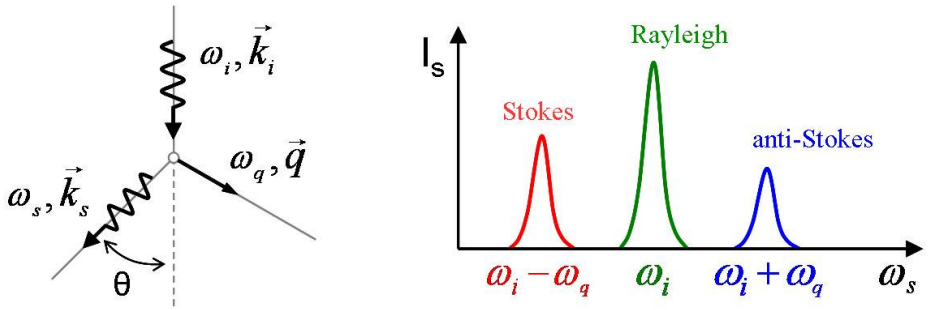


**Figure 3.4.** Scheme of the Raman scattering process and its spectrum. θ=0º and θ=180º designate forward and backward scattering geometry respectively.

excitation frequency and the Raman frequency will then appear at $\pm\omega_q$. In practice, Raman shifts are usually measured in wavenumbers ($\overline{\upsilon} = \upsilon / c = 1/\lambda$) in units of $cm^{-1}$.

It should be emphasized that the efficiencies of these scattering processes are very low. Typically, the intensity of a Raman line (for non-resonant excitation) is about $10^{-6}$ times weaker than the incident excitation.

### 3.5.1. Semi-classical theory of Raman scattering by phonons

The light-matter interaction can be thought in a classical picture as the action of the electric field of the light wave on the charges in the material. In this representation the scattering comes from the radiation emitted by the oscillating dipoles caused by the incident electric field.

Considering an infinite medium with electric susceptibility $\vec{\vec{\chi}}$, the incident electric field $\vec{E}_i(\vec{r},t)$:

$$\vec{E}_i(\vec{r},t) = E_0\vec{e}_i \cos\left(\vec{k}_i \cdot \vec{r} - \omega_i t\right) \tag{3.16}$$

will induce a polarization in the medium given by:

$$\vec{P}(\vec{r},t) = \vec{\vec{\chi}}\vec{E}_i \tag{3.17}$$

If the medium is at finite temperature there are fluctuations in $\vec{\vec{\chi}}$ due to the thermally excited atomic vibrations. In crystalline semiconductors the atomic vibrations are quantized into phonons. The atomic displacements $Q(\vec{r},t)$ associated with a phonon can be expressed as:

$$Q(\vec{r},t) = Q_0 \cos\left(\vec{q} \cdot \vec{r} - \omega_q t\right) \tag{3.18}$$

At room temperature, these vibrations are usually small in amplitude, so we can expand $\vec{\vec{\chi}}$ as a Taylor series in $Q(\vec{r},t)$:

$$\vec{\vec{\chi}} = \vec{\vec{\chi}}_0 + \left(\frac{\partial \vec{\vec{\chi}}}{\partial Q}\right)_0 Q(\vec{r},t) + \cdots \tag{3.19}$$

where $\vec{\vec{\chi}}_0$ denotes the electric susceptibility of the static medium and the second term represents an oscillating susceptibility induced by the lattice wave $Q(\vec{r},t)$. Thus, substituting (3.19) into (3.17), the polarization of the medium can be expressed in two components:

$$\vec{P}(\vec{r},t,Q) = \vec{P}_0(\vec{r},t) + \vec{P}_{ind}(\vec{r},t,Q) \tag{3.20}$$

where

$$\vec{P}_0(\vec{r},t) = \vec{\vec{\chi}}_0 E_0 \vec{e}_i \cos\left(\vec{k}_i \vec{r} - \omega_i t\right) \tag{3.21}$$

is the polarization oscillating in phase with the incident radiation, i.e., it corresponds to the elastic scattering. The second term in (3.20) is given by:

$$\vec{P}_{ind}(\vec{r},t,Q) = \left(\frac{\partial \vec{\vec{\chi}}}{\partial Q}\right)_0 Q(\vec{r},t) E_0 \vec{e}_i \cos\left(\vec{k}_i \vec{r} - \omega_i t\right) \tag{3.22}$$

It corresponds to the polarization wave induced by the phonon and can be rewritten as:

$$\begin{aligned} \vec{P}_{ind}(\vec{r},t,Q) &= \frac{1}{2}\left(\frac{\partial \vec{\vec{\chi}}}{\partial Q}\right)_0 Q_0 E_0 \vec{e}_i \\ &\times\left\{\cos\left((\vec{k}_i + \vec{q})\cdot\vec{r} - (\omega_i + \omega_0)t\right) + \cos\left((\vec{k}_i - \vec{q})\cdot\vec{r} - (\omega_i - \omega_0)t\right)\right\} \end{aligned} \tag{3.23}$$

The first oscillating term corresponds to the absorption of a phonon by the lattice (*anti-Stokes* process), while the second term corresponds to the emission of a phonon (*Stokes* process).

It is worth noticing that both, frequency and wavevector, are conserved in the scattering processes. Since $\left|\vec{k}_i\right| = 2\pi/\lambda_i$ and assuming that visible lasers are normally used in Raman spectroscopy, only phonons near the center of the Brillouin zone ($\vec{q} \approx 0$) will be observed in first-order scattering processes. The whole Brillouin zone can be accessible in higher-order processes, where two or more phonons give the resulting wavevector $\vec{q} = \sum_i \vec{q}_i$.

### 3.5.2. Quantum-mechanical description of Raman scattering by phonons

Although Raman scattering can be described with the classical theory, it is interesting to keep in mind its quantum-mechanical interpretation, which is based on the creation and annihilation of phonons.

There are three *particles* involved in the process: photons (incident and scattered), electrons and phonons. The initial state is formed by: $N(\omega_i)$ incident photons, $N(\omega_s)$ scattered photons, $N_q$ phonons and all the electrons in their ground states (*GS*). The final state, depending on whether the Raman scattering is Stokes or anti-Stokes, will be:

$$Stokes: \begin{cases} N(\omega_i)-1 \\ N(\omega_s)+1 \\ N_q+1 \\ e^- \ in \ GS \end{cases} \qquad anti\text{-}Stokes: \begin{cases} N(\omega_i)-1 \\ N(\omega_s)+1 \\ N_q-1 \\ e^- \ in \ GS \end{cases}$$

Although the electrons seem not to play any role, they are essential intermediaries in the process. The photon-phonon interaction is very weak unless the photons and phonons have comparable frequency. This requirement cannot be experimentally satisfied due to the lack of laser sources in the far-infrared. Thus, when visible photons are used to excite Raman scattering in a semiconductor, they couple to electrons via the electron-radiation interaction Hamiltonian $H_{eR}$.

The scattering event, illustrated in Figure 3.5, occurs in three steps:

1. The incident photon excites the semiconductor into an intermediate virtual state by creating an *e-h pair*.
2. This *e-h pair* is scattered into another state by emitting or absorbing a phonon via the electron-phonon interaction Hamiltonian $H_{e\text{-}ion}$.
3. The new *e-h pair* recombines radiatively with emission of the scattered photon.

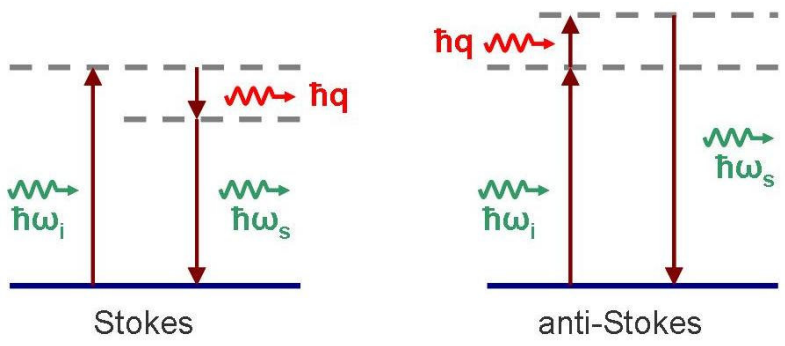


**Figure 3.5.** Quantum diagram of the Raman effect.

Although the system returns to the same electronic state, the vibrational state has changed by one phonon. Since the transitions involving electrons are virtual they do not have to conserve energy, although they still have to conserve wavevector. In the specific case of resonant Raman scattering (RRS), these virtual states become real electronic states so that the process is highly efficient and the intensity of the scattered light is strongly enhanced. Then, via resonance Raman spectra, one can learn also about the electronic structure of the material.

### 3.5.3. Selection rules

Regarding again the semi-classical theory of the Raman effect, the intensity of the scattered radiation will depend on its polarization $\vec{e}_s$ as:

$$I_s \propto \left|\vec{P}_{ind} \cdot \vec{e}_s\right|^2 \tag{3.24}$$

If we denote $\vec{e}_i$ for the incident radiation polarization, the scattered intensity $I_s$ calculated from (3.23) for the Stokes process is given by:

$$I_s \propto \left|\vec{e}_i \cdot \left(\frac{\partial \vec{\chi}}{\partial Q}\right)_0 \cdot \vec{e}_s\right|^2 \tag{3.25}$$

It can also be expressed in terms of the Raman tensor $\vec{\vec{R}}$, which is proportional to $\partial\vec{\chi}/\partial Q$:

$$I_s \propto \left|\vec{e}_i \cdot \vec{\vec{R}} \cdot \vec{e}_s\right|^2 \tag{3.26}$$

This expression for the intensity of the scattered radiation contains the so-called Raman selection rules, which depend on the incident and scattered light polarization and the phonon symmetry.

The phonons in a given crystal correspond to the different symmetries of vibration of the atoms in the unit cell (normal modes). The group theory allows determining these vibrational modes as well as the elements of the Raman tensor which are non-zero. Raman tensors and selection rules for all crystal point groups can be found in [146].

Due to the Raman selection rules, Raman spectra can vary in different experimental geometries. Porto´s notation is useful for representing the scattering geometries and polarization configurations. The polarization ($\vec{e}$) and propagation direction ($\vec{k}$) for incident and scattered light are written in the form $\vec{k}_i(\vec{e}_i,\vec{e}_s)\vec{k}_s$. In this way, for example, the symbol $x(z,x)y$ indicates that the incident light is z-polarized and propagates along x-direction, while the detected light travels along y-direction with x-polarization. For

simplicity, the involved directions are chosen along the crystallographic axes, so they can relate directly to the components of the Raman tensor. Thus, in the example given, the Raman intensity will be proportional to

$$\left|\vec{e}_i \cdot \vec{\vec{R}} \cdot \vec{e}_s\right|^2 = \left| \begin{pmatrix} 0 & 0 & 1 \end{pmatrix} \cdot \begin{pmatrix} R_{xx} & R_{xy} & R_{xz} \\ R_{yx} & R_{yy} & R_{yz} \\ R_{zx} & R_{zy} & R_{zz} \end{pmatrix} \cdot \begin{pmatrix} 1 \\ 0 \\ 0 \end{pmatrix} \right|^2 = R_{zx}^2 \qquad (3.27)$$

In this Thesis, Raman scattering has been essentially studied in InN nanocolumns with wurtzite structure. The corresponding Raman tensors for the optical phonons are given in Table 3.3 [104]. The directions given in parentheses correspond to the polarization direction for the polar phonons, taking into account that for wurtzite structure the z-direction is chosen parallel to the crystallographic *c*-axis. The Raman tensor for the $A_1$ phonon presents only diagonal components which are non-zero, so it can only be detected in parallel polarization geometry. The opposite occurs for the $E_1$ mode that can only be observed for crossed incident and scattered polarizations. The $E_2$ mode can be detected in both parallel and crossed polarization configurations. The Raman selection rules for the pure phonons in wurtzite structure are shown in Table 3.4 for different scattering configurations.

| $A_1(z)$ | $E_1(x)$ | $E_1(y)$ | $E_2$ |
|---|---|---|---|
| $\begin{pmatrix} a & 0 & 0 \\ 0 & a & 0 \\ 0 & 0 & b \end{pmatrix}$ | $\begin{pmatrix} 0 & 0 & c \\ 0 & 0 & 0 \\ c & 0 & 0 \end{pmatrix}$ | $\begin{pmatrix} 0 & 0 & 0 \\ 0 & 0 & c \\ 0 & c & 0 \end{pmatrix}$ | $\begin{pmatrix} d & d & 0 \\ d & -d & 0 \\ 0 & 0 & 0 \end{pmatrix}$ |

**Table 3.3.** Raman tensors for optical phonons in wurzite structure.

| Scattering geometry | Raman mode |
|---|---|
| $z(x,x)\overline{z}$ | $A_1$(LO), $E_2$ |
| $z(x,y)\overline{z}$ | $E_2$ |
| $x(y,y)\overline{x}$ | $A_1$(TO), $E_2$ |
| $x(y,z)\overline{x}$ | $E_1$(TO) |
| $x(z,z)\overline{x}$ | $A_1$(TO) |
| $x(y,z)y$ | $E_1$(LO), $E_1$(TO) |

**Table 3.4.** Selection rules for allowed optical phonons in wurtzite structure.

In the case of polar phonons, the displacements of the atoms can induce an oscillating macroscopic polarization, leading to an electric field. The Coulomb interaction between the carriers in the material and this macroscopic field is known as *Fröhlich interaction* [147-149]. Interband and intraband carrier scattering effects appear due to this interaction. That is the scattering of an *e-h* pair from one exciton state to another one. The intraband Fröhlich interaction constitutes the forbidden scattering mechanism, whose Raman tensor is $\vec{q}$-dependent. Thus, it obeys new selection rules. Despite being forbidden by the usual selection rules, near resonance, this scattering can be dominant over the allowed one. In particular, the Fröhlich interaction is very strong in III-nitrides due to its ionic nature. In these materials, the new selection rules [149] lead to the observation of the $E_1$(LO) mode in parallel polarization configuration as we will see in Chapter 5, which is forbidden according to the usual selection rules (Table 3.4).

## 3.6. Experimental setups for optical spectroscopy

All the experimental setups needed for optical spectroscopy can be divided into the following components:

1. The light source
2. The sample and its environment
3. Detection instrumentation for the light
4. Data processing and control system

This section starts with the description of the basic setups needed for the different optical spectroscopic techniques used in this Thesis. Later on, a description of the instrumentation used for low temperature measurements is given. Finally, the process of gas adsorption on microcavity samples is described. It is needed for changing the cavity mode wavelength during the experiment in order to study the QR-CM system at resonance.

### 3.6.1. Macro- and micro-configuration setups

The basic experimental setups for macro- and micro-configurations of optical spectroscopy are schematically shown in Figures 3.6 and 3.7, respectively.

Different lasers have been used: two continuous-wave lasers with fixed wavelengths, namely Argon ion ($Ar^+$) and He-Ne lasers, one tunable Ti-Sapphire laser pumped with the $Ar^+$-laser and one picosecond pulsed diode laser. Details of the lasers are given in Table 3.5, as well as the specific experimental techniques for which they were used.

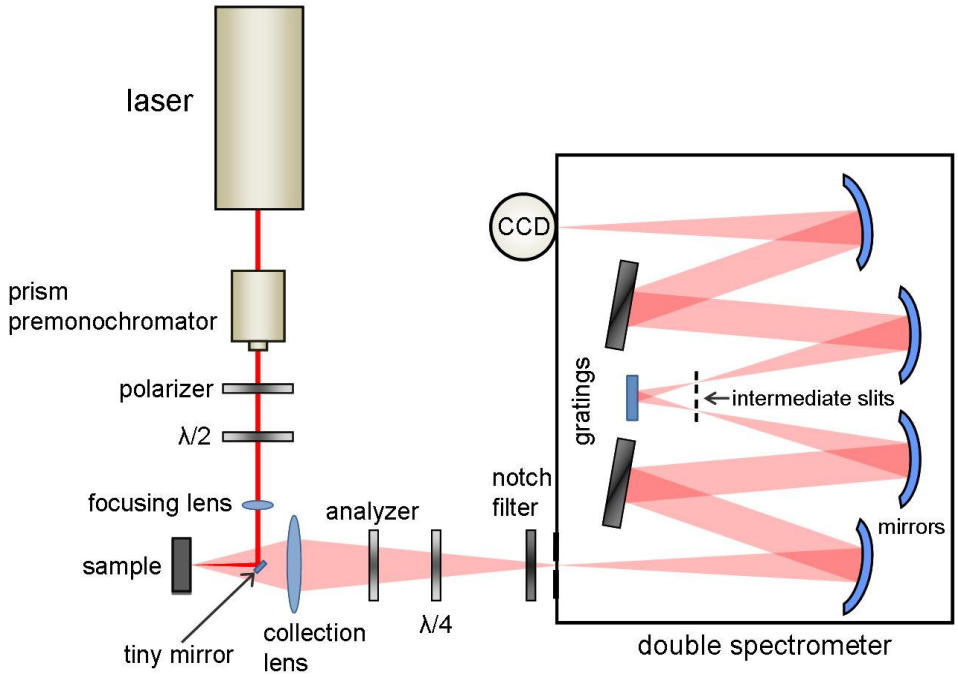


**Figure 3.6.** Schematic illustration of the macro-configuration setup.

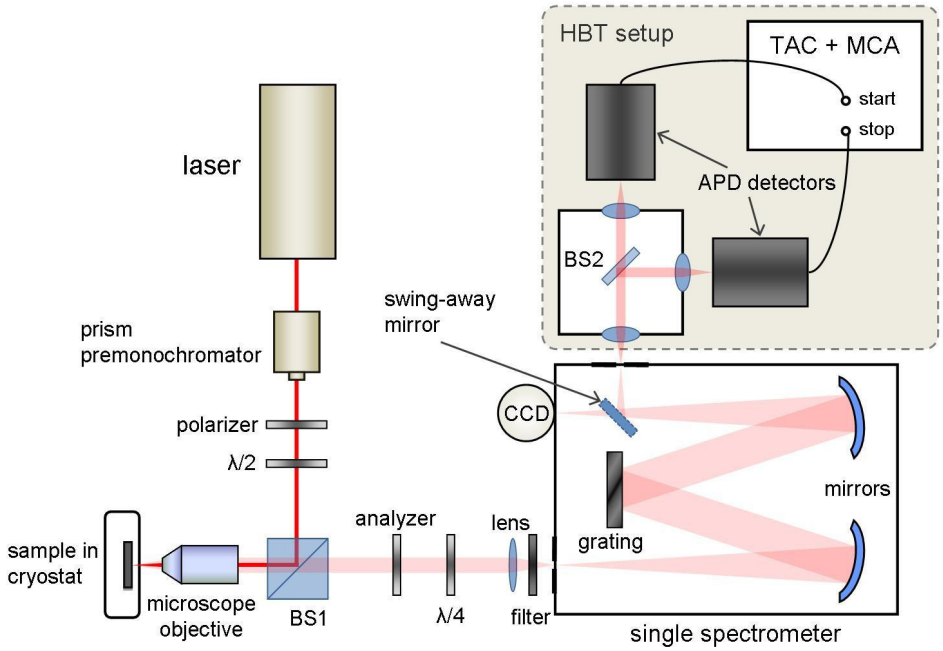


**Figure 3.7.** Schematic illustration of the micro-configuration setup.

| Laser | Model | Wavelength and other specifications | Experimental technique |
|---|---|---|---|
| $Ar^+$ | Spectra Physics: BeamLok 2060/2080 | CW 514.5 and 457.9 nm | Raman |
| He-Ne | Melles Griot: 05-LHP-928 | CW 632.8 nm, 35 mW | PL, Raman and photon correlation |
| Ti:Sapphire | Spectra Physics: 3900S | CW, 700-980 nm | PL, PLE and photon correlation |
| Picosecond Pulsed Diode | PicoQuant:<br>LDH-P-870 laser head +<br>PDL 800B pulsed diode laser driver | 866 nm<br>minimum pulse width 59 ps<br>rep freq up to 40 MHz | TCSPC |

**Table 3.5.** Details of the lasers used in this Thesis.

Before reaching the sample, the laser usually passes through a prism premonochromator for any unwanted sidebands or plasma lines of gas lasers being removed. The main difference between macro- and micro-configurations is found in the sample illumination and collection systems, which are related with the spatial resolution in the measurement. While for macro-setup one lens is used for each purpose (focusing and collection lenses in Figure 3.6), in micro-configuration the central element, which is the microscope objective, is used for both. The lenses used in the macro-setup have typical focal lengths of 10 and 5 cm for the illumination and collection, respectively. The first one is responsible for the laser spot in the sample surface which is given by $d = {4\lambda F}/{\pi D}$ (Gaussian spot diameter) where $F$ is the focal length of the lens, $D$ is the beam diameter and $\lambda$ is the laser wavelength. This yields to a spot size of some tens of microns for lasers with visible and near-infrared wavelengths. Regarding the study of single QDs, this spot size is too large because many of them are illuminated at the same time. For the investigation of the properties of single QDs or other nanostructures, a reduction in the spot size is required and it is achieved by using the micro-setup configuration. A microscope objective of long working distance (few mm), as the ones used in this study, gives a typical spot diameter of 1-2 μm. In this Thesis, the macro-setup has only been used for Raman spectroscopy of InN NCs, while the study of InAs/GaAs QRs, which include all the other optical techniques, has been performed with the micro-configuration setup.

In the general micro-setup, a beam-splitter (BS1 in Figure 3.7) directs the laser through the objective to illuminate the sample. The same beam-splitter transmits the emitted light towards the detection system (the spectrometer). When the He-Ne laser was used to excite the sample, this beam-splitter was substituted by a dichroic filter (*Semrock* LPDO1-633RU-25) working at 45º that reflected almost 100% of that specific

wavelength and transmited again almost 100% of the signal. This substitution is very convenient for those techniques where the signal intensity is of special importance as in TCSPC and photon correlation techniques. Two microscope objectives from *Nikon* with different magnifications have been employed:

- CF SLWD Plan EPI M=100X/NA=0.73 WD 4.7 mm
- CF ELWD Plan EPI M=50X/NA=0.55 WD 8.7 mm

(M, NA and WD refer to magnification, numerical aperture and working distance respectively)

The microscope objective is mounted on a computer-controlled *XYZ* DC-motor stage (*Standa* 8DCMC1.01) and its position can be varied with a step size of 14 nm. This allows the fine adjustment of the spot location on the sample surface.

Once the light from the sample is collected, it is directed to the detection system. A single or double grating spectrometer has been used as dispersive element before the detection. Both spectrometers have been employed in both macro- and micro-configurations. The PL or scattered light is focused onto the entrance slit of the spectrometer. The spectrometer consists of one (single) or two (double) diffraction gratings and several concave mirrors to collimate and focus the light. The grating of the single spectrometer has 1200 grooves/mm and the double spectrometer is equipped with two pairs of gratings of 600 or 1800 grooves/mm. The spectral resolution of a spectrometer depends on the width of the entrance slit, the total number of grooves illuminated and the focal distance. The typical resolution in this Thesis was 100 μeV. Spectral lines of a Ne-lamp were used for spectrometer calibration.

For photoluminescence and Raman experiments, the last mirror of the spectrometer directs and focuses the signal onto a charged coupled device (CCD) camera. Each CCD consists of a two-dimensional matrix of 1024x256 silicon pixels of 26-27 μm size. In order to reduce the noise level, the CCDs are cooled with liquid nitrogen to approximately 170 K.

For TCSPC and photon correlation experiments (only with the single spectrometer), a swing-away mirror is set to send the signal to an exit slit in the side of the spectrometer (see Figure 3.7). Then the signal arrives to the typical HBT interferometer with APD detectors if auto-correlation measurements are planed. For the cross-correlation measurements performed in this Thesis, the exit slit was totally opened and two spectral windows can be extracted from the spectrometer. Then each APD is placed to detect each transition. For TCSPC experiments, the beam-splitter BS2 in Figure 3.7 has to be removed and the complete signal is directed only to one APD. The other one is not needed because the triggered signal of the pulsed laser can be electrically synchronized directly to the correlator device (TAC+MCA).

Among the typical sources of noise in the correlation measurements with a HBT setup are the low signals detected in the APD detectors, the scattered light in the spectrometer and the HBT setup, the laser background and photons reemitted by the detectors [138]. The latter effect was reduced by placing appropriate filters in the HBT setup to avoid that the photons emitted by one detector could reach the other one.

Model numbers and other properties of the spectrometers, the detectors and the correlator device used in this Thesis are listed in Table 3.6.

Other optical elements have been placed in the experimental setup (both macro- and micro-) for the analysis of the polarization properties. A polarizer and λ/2 wave plate (from *Newport*) is positioned in the laser path to choose and rotate its linear polarization. Another polarizer (analyzer) is placed in the signal path before the spectrometer. A λ/4 wave plate is used at 45º to convert the linear polarization of the signal into circular polarization to overcome the different sensibility of the gratings to orthogonal linear polarizations. Moreover, long-wave-pass filters (from *Melles Griot*) have been placed in front of the entrance slit of the spectrometer in order to remove spurious laser light. In the case of Raman measurements, holographic notch filters (from *Kaiser Optical Systems*) are used to reduce the elastically scattered light.

| **Spectrometers** | | |
|---|---|---|
| Single grating | SPEX 750M | F = 75 cm, NA = f/6, res = 0.01nm |
| Double grating | SPEX 1404 | F = 85 cm, NA = f/7.8, res = 0.005nm |
| **Detectors** | | |
| CCD | Jobin Ybon CCD-3000(V) (single SPEX)<br>Jobin Ybon SpectraView-2D (double SPEX) | pixel size = 26 μm, UV-NIR<br>pixel size = 27 μm, VIS-NIR |
| APD | PerkinElmer: SPCM-AQR-16 | efficiency 30% at 920 nm<br>dead time 50 ns<br><25 dark counts/s |
| **Correlator Device** | | |
| TAC+MCA | PicoQuant: PicoHarp300 | TTTR mode:<br>T2 mode → photon correlation<br>T3 mode → TCSPC |

**Table 3.6.** Details of the spectrometers, detectors and correlator device used in this Thesis.

### 3.6.2. Low temperature measurements

It is well known that the PL intensity of a semiconductor usually increases while the temperature of the sample is decreased. Thus, all the measurements involving the PL technique (PL, PLE, TCSPC and photon-correlation) on InAs/GaAs QRs were performed at low temperature (LT). On the contrary, the study of InN NCs, by Raman spectroscopy, was carried out at room temperature (RT).

The sample is cooled down by mounting it in the high vacuum chamber of a cryostat with the sample holder being cooled by a continuous flow of liquid helium (He). For this purpose, the cryostat used was a Konti-Cryostat-Mikro from *CryoVac* suitable for micro-photoluminescence setup. The operation temperature range is 4-325 K. The sample was glued to the sample holder with silver paint to ensure good thermal contact. The cryostat is equipped with a temperature sensor (Si-diode DT670A), a heater and a temperature control unit (TIC 304-MA). The temperature range used in the measurements of this Thesis was from 7 K to approximately 60 K.

The cryostat was mounted in a XYZ translation stage in order to access different regions of the sample, which is larger than the field of view of the microscope objective. Moreover, it was usually mounted horizontally to reach a good mechanical stability, what is crucial especially in photon-correlation measurements in which very long integration times are needed.

### 3.6.3. Spectral tuning by gas adsorption technique

As it has been explained before, the study of the coupling between a single QD and a CM is of great interest in the field of cQED. Photonic crystal microcavities present the smallest mode volume of the solid states microcavities. Therefore, in samples with self-assembled QDs and PC microcavities fabricated non-deterministically, it is very unlikely to find a single QD that is accidentally located near to the CM field maximum and spectrally positioned close to the CM frequency. Usually, one has to look for these accidental coincidences in many cavities. Even if one finds a way to fabricate a PC microcavity around a spatially isolated QD (deterministic location), it would still be a challenge to make both emissions coincide in frequency. One way of reaching this coincidence is changing the sample temperature, which affects both the bandgap of the QD and the effective refractive index of the cavity. As the QD transitions experiment red-shifts with increasing temperature which are much faster than the CM ones, the energy difference (detuning) between QD and CM can be varied. However, this method is limited by the increase of the linewidth due to the phonon broadening at high temperatures. Therefore, it is desirable to control the mode wavelength while the QD transitions remain unchanged.

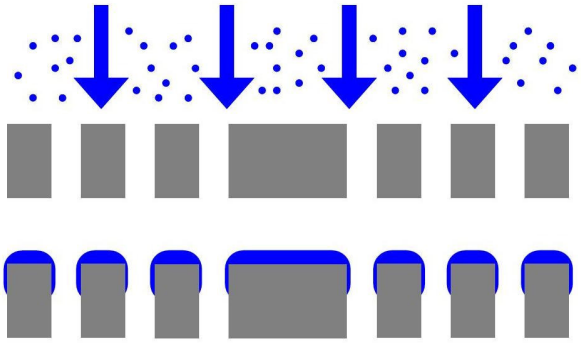

**Figure 3.8.** Schematic illustration of the gas adsorption operation principle.

The CM wavelength in a PC microcavity (see Section 2.1.2) depends only on its geometrical parameters (membrane thickness, lattice constant and hole diameter) and on the refractive index of the material. Then, a change in its structure leads to a wavelength shift of the CM. A post-fabrication fine tuning of the CM can be achieved by controlled deposition of extra dielectric material on the membrane surface [150, 151]. This extra material can be supplied by cryogenic adsorption of gas on the cavity membrane. The cold sample surface acts as an efficient adsorption pump for residual gas in the cryostat vacuum chamber. Thus, gas molecules introduced in the cryostat when it is already cold adhere to the sample surface forming a thin layer of dielectric material, as shown in Figure 3.8, increasing the membrane thickness and reducing the hole diameter. This provokes a red-shift of the CM wavelength.

The implemented setup needed for carrying out this method is shown in Figure 3.9. Trial gases were Xe and $N_2$. The former was finally chosen because the results were much more reproducible than with $N_2$. Xe was supplied by a high-pressure bottle with a regulator to lower the outlet pressure. A dosing valve (*Pfeiffer Vacuum* EVN 116) was used to control the precise pressure of gas in the Xe-chamber. All the elements were previously evacuated to a pressure of $10^{-6}$ mbar. Another valve (yellow valve in Figure 3.9) isolates the Xe-chamber from the cryostat. Once the desired pressure in the Xe chamber is reached (3.5-4 mbar with a chamber volume of ~ 65 ml), the Xe flow is stopped and the gas accumulated is allowed into the cryostat by opening the yellow valve. The shift in the CM wavelength is almost instantaneous. The cycle can be repeated several times until the shift starts to saturate. Total shifts up to 2 nm have been performed in this Thesis without dropping of the cavity quality factor Q. To remove the Xe thin layer, just warming up the sample above the Xe melting temperature (161.4 K) is necessary.

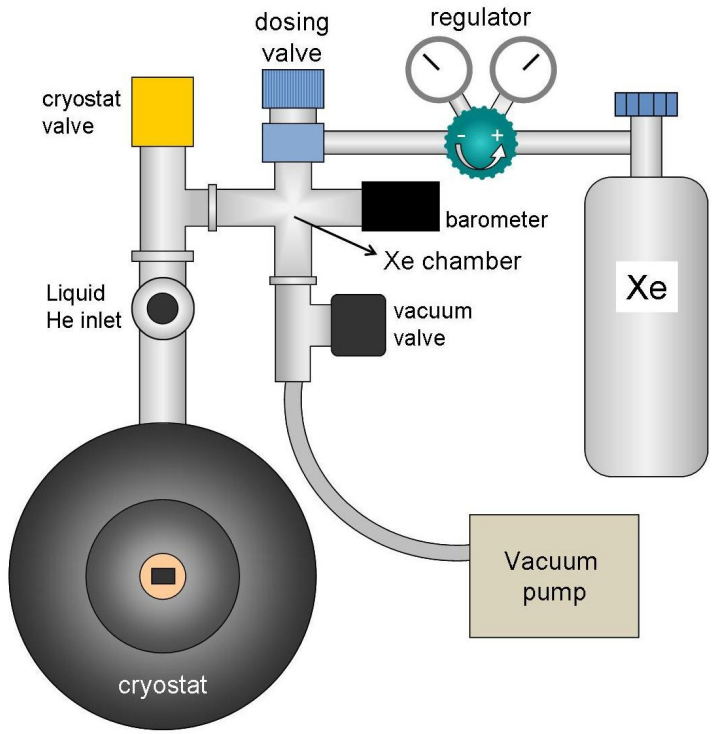


**Figure 3.9.** Schematic instrumentation for gas adsorption technique.

It is worthy to say that the effect of gas adsorption on the sample surface is automatically present due to the not perfect isolation vacuum in cryostats. In fact, each time that we first cool down the sample, the CM wavelength is not predictable due to condensation of residual gas. In order to start each measurement with the same and shortest CM wavelength, temperature cycles from 7 K to 315 K and back again to 7 K are needed.

## 3.7. Transmission electron microscopy

In order to understand the properties of InN NCs, a structural study of them was carried out by transmission electron microscopy (TEM) in collaboration with the group of Dr. A. Trampert at the *Paul-Drude Institut für Festkörperelektronik* (PDI) in Berlin. An innovative procedure was performed for sample preparation. In this section, the basic principle of TEM technique, as well as the sample preparation methods, is explained. Growth details of the InN NCs samples studied in this Thesis will be given in Chapter 5. Further information about TEM can be found in [152-154].

### 3.7.1. Basic principle of TEM.

Transmission electron microscopy is based on the irradiation of thin specimens (around 100 nm thick) by high-energy electrons. Due to the short wavelength of electrons compared to visible photons, resolutions of few angstroms can be achieved. Then this technique can provide very useful information about the quality or the defects of crystalline structures, as semiconductor materials.

The basic scheme of a TEM is shown in Figure 3.10. The electrons emitted from the electron gun are accelerated within a voltage drop of typically 200-500 kV. The condenser lens collimates the electrons to make an approximately parallel beam, which illuminates the specimen uniformly. Then the objective lens produces the first image. This image is magnified by the intermediate lenses and projected onto a fluorescent screen or a CCD camera by the projector lens. The electron lenses are designed to act as optical lenses. The majority of them utilize electromagnetic coils to generate a convex lens.

Part of the incident electrons are elastically scattered or diffracted by the specimen; another part is inelastically scattered and a third part penetrates the specimen without scattering (direct transmitted beam). The elastically scattered electrons, which are deflected at small angles, and the direct beam can be used for image formation. Below the objective lens there is an aperture which filters the beam. In this way, the electrons scattered at high angles, which may be due to unwanted processes as aberrations, are removed. Imaging methods in TEM use the information contained in the electron-wave at the exit of the sample to form an image. Different imaging modes can be chosen by suitable selection of the size and position of the objective aperture. If a small aperture is employed and centered onto the optical axis so that only the direct beam passes through, the mode is called *bright-field imaging* (Figure 3.11(a)). On the contrary, in *dark-field imaging*, the image is generated by the diffracted or scattered electrons. This can be achieved by displacing the objective aperture or by tilting the incident beam (Figure 3.11(b)).

In general, the amplitude and phase of the electron wavefunction are affected by the sample. Phase effects can be usually ignored at lower magnifications. On the other hand, in very thin specimens (10-50 nm), the interaction between the electrons and the specimen is weak and only the phase of the incident electron wave is changed. In this case, to obtain good image contrast, both direct beam and scattered electrons must be included in image production (Figure 3.11(c)). Thus, in thin crystals, the crystal lattice can be directly imaged in a specific projection. This type of imaging is known as *high-resolution mode* (HR-TEM).

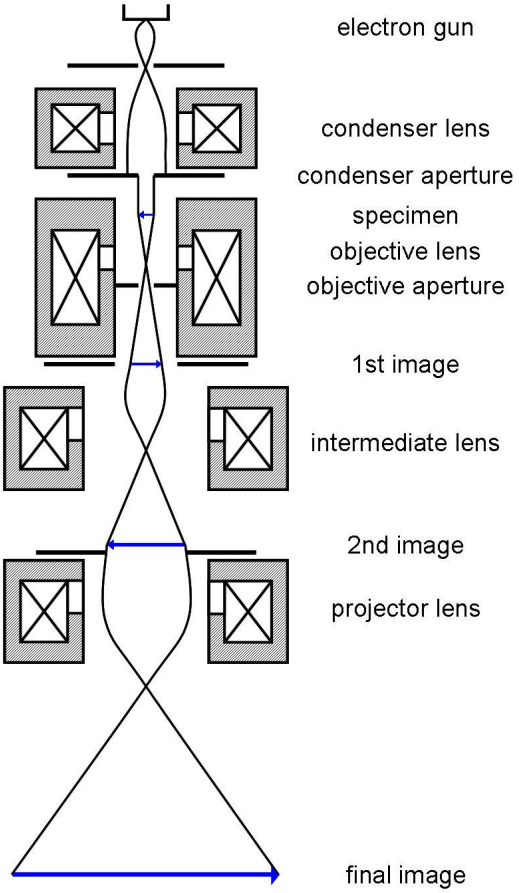


**Figure 3.10.** Schematic diagram of a TEM.

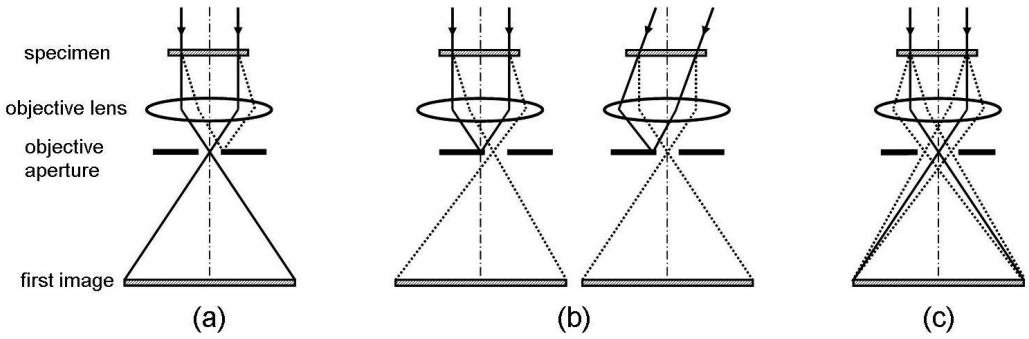


**Figure 3.11**. Imaging modes. (a) Bright-field mode. (b) Dark-field mode, displaced and centered aperture. (c) High-resolution mode.

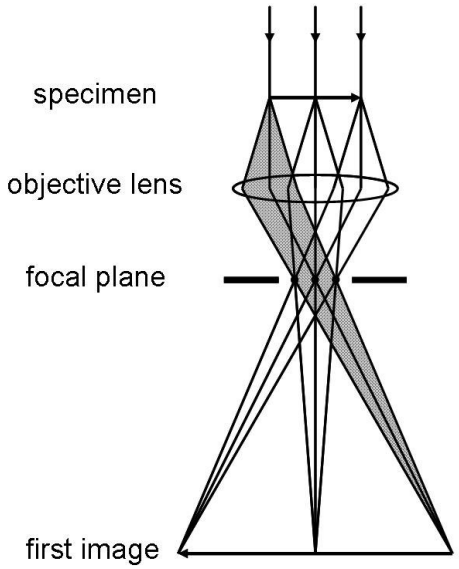


**Figure 3.12.** Relation between imaging and diffraction

Apart from the imaging methods, in a TEM it is possible to analyze the electron diffraction pattern produced by the specimen. In Figure 3.12 the ray path between the specimen and the first image is shown in detail. All rays leaving one specimen point are deflected by the lens so that they meet at one image point, producing a magnified image of the specimen. It is important to notice that all rays leaving the specimen in a specific direction meet in the *back focal plane*. So a specific point in the focal plane corresponds to a particular direction of radiation. The radiation diffracted in different directions is focused by the lens at different points, producing a diffraction pattern. By adjusting the lenses so that the back focal plane is placed on the fluorescence screen, the electron diffraction pattern can be observed. By inserting an additional aperture in the first image plane the diffraction information can be selected from a specific area of the specimen. This method is called *selected area electron diffraction* (SAED).

Different types of specimens produce different types of electron diffraction patterns: very thin single crystals produce spot patterns, thicker single crystals produce Kikuchi patterns, poly-crystals create ring patterns and amorphous substances produce diffuse rings. By analysis of the diffraction patterns, information of the specimen can be obtained. In particular, the spot patterns of an unknown crystal can provide information about the composition and the lattice structure. For that purpose, it is common to make use of tables with the spot patterns of different crystalline structures.

All the TEM images presented in this Thesis have been performed with a JEOL JEM 3010 microscope operating at 300 kV and equipped with a GATAN CCD at the *Paul-Drude Institut für Festkörperelektronik* (PDI) in Berlin.

### 3.7.2. Sample preparation methods

The necessity of specimens with a thickness in the region of 100 nm requires suitable preparation techniques. There are two main modes of preparing the samples namely *plan-view* (PV) and *cross-section* (X) TEM depending on whether the sample is going to be studied from the top or from the side, respectively. The conventional preparation method of specimens for TEM consists of 4 steps [155, 156]:

1. Preparing a piece of the sample with suitable size for the TEM. For PV-TEM cutting a 2x2 mm piece is enough. For X-TEM this step is more elaborated: two longer pieces (2x10 mm) of the sample are glued with epoxy, with the surfaces facing each other, and then inserted into a tube filling it with more epoxy. Then the tube is cut into slices. Each slice can be prepared for TEM.
2. Polishing of the sample down to a thickness of around 100 μm.
3. Dimpling the sample for one side. This process produces a thin central region in the sample of about 30 μm.
4. Ion milling. The sample is sputtered with ion-guns until perforation. It takes usually few hours. The regions of the sample near the hole are thin enough for TEM investigations.

The main difficulty in NCs samples lies on the fact that the NCs are weakly bound to the substrate and there is a high probability of detachment as a result of the improper manipulation. The preparation method for X-TEM in NCs was already established from the group of PDI when the collaboration started, so only PV-TEM preparation procedure will be explained in detail.

The aim of studying InN NCs in PV-TEM was the analysis of the surface electron accumulation layer at the sidewalls of the NCs. The first trial was based on the easy detachment of the NCs mentioned above. The NCs were removed for the substrate by sonication in an ethanol bath or by scratching directly the sample surface. Then they were dispersed on a TEM carbon grid. This method relied on the probability of finding NCs oriented in the right direction for PV-observation. However, most of the NCs were found to be lying on the grid along their *c*-axis, so only X-TEM images could be obtained.

It was then a crucial prerequisite to find a mechanical stabilization of the NCs on the substrate. The idea was filling the space in between the columns with a cured epoxy or resin. Although the idea is simple in theory, in practice there was an important problem: how to deposit a uniform thin coating (around 500 nm thick) of a material compatible with TEM measurements. The next try was to form the thin layer by rotating the sample with the use of a spinner after the deposition of a resin drop on top. The samples were always baked in a hot-plate after the rotation. Different glues, times, rotation speeds and

hot-plate temperatures were employed, but the result was always that the coating was too thick and no good images could be observed in the TEM.

Finally, the best performance was obtained by using GATAN G1 epoxy by applying manually some tiny drops of the epoxy on the sample surface while it was on a hot-plate at around 65ºC. As shown in Figure 3.13, the resin was slowly spreading until covering the entire surface. Later, it was baked 30 minutes at 140ºC to cure the resin. With this method the NCs were completely stabilized and protected and the sample was ready to continue with the preparation. The next steps were polishing and dimpling the sample. During the dimpling, a second innovative approach was introduced: we dimple the sample until perforation. Afterwards, the sample was sputtered with low energy argon ions for about only 10 minutes. This procedure permits the fabrication of TEM specimens based on NCs samples which fulfills the requirements for high resolution, as will be shown in Chapter 5.

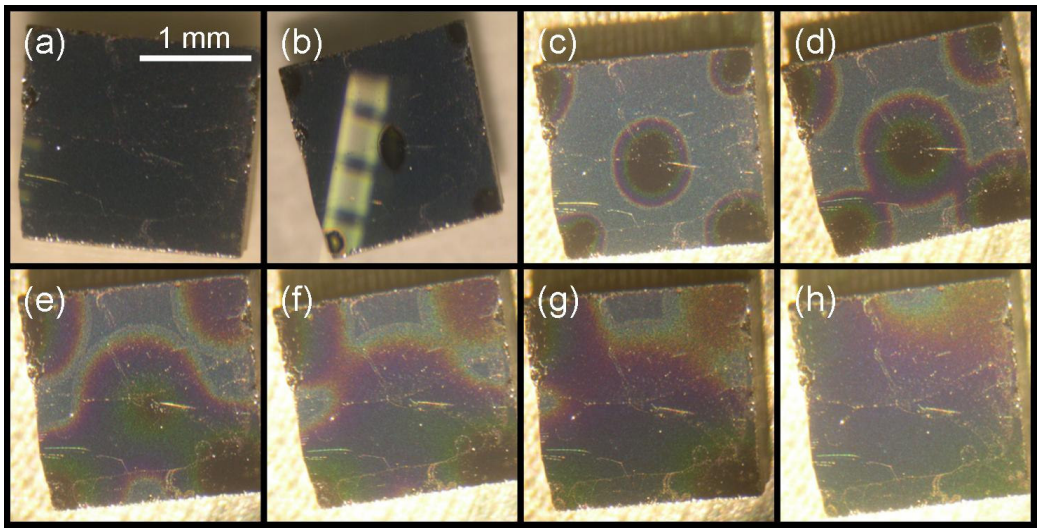


**Figure 3.13.** Epoxy application process on a sample with NCs. (a) Sample with no glue. (b) Tiny drops are applied on the corners and the center of the sample. (c-g) The resin is slowly spreading on the sample surface. (h) The sample is almost totally covered with the resin.

# Chapter 4

# Optical Properties of InAs/GaAs Quantum Rings in a Photonic Crystal Microcavity

Single zero-dimensional semiconductor nanostructures (as QDs) coupled to optical microcavities are the basis of efficient single photon sources for quantum information applications. Continuous polarization control of the QDs emission is desirable for the development of sources of entangled photon pairs. Moreover, QDs are potential semiconductor qubits needed for quantum logic operations, which could be carried out by the coupling of two or more distant qubits mediated by an optical cavity. The use of QRs for the demonstration of these properties adds flexibility in the design of quantum devices.

This chapter presents our results on the optical properties of InAs/GaAs QRs embedded in a PC microcavity. They are not specific of the ring-like shaped nanostructures so they could be observed in principle also in "standard" QDs. The chapter is organized as follows: Section 4.1 presents a general description of the sample structure, as well as the studied PC microcavity. An optical characterization of the microcavity showing the spatial and spectral distribution of the CMs is given in section 4.2. Section 4.3 presents photon correlation measurements of a QR not coupled to the cavity, showing SPE behaviour. Individual cavity coupling of two selected QRs is demonstrated in Section 4.4 by continuous and time resolved PL and polarization measurements. An effective coupling between these two QRs mediated by the cavity is shown in Section 4.5 by PLE measurements. Finally, a summary and proposals for future work are given in Sections 4.6 and 4.7 respectively.

## 4.1. Sample description

The sample investigated in this chapter consists of one layer of randomly distributed self-assembled InAs QRs grown by solid source MBE. The QRs are located inside a 158 nm thick GaAs slab grown on top of a 500 nm thick $Al_{0.75}Ga_{0.25}As$ sacrificial layer. The

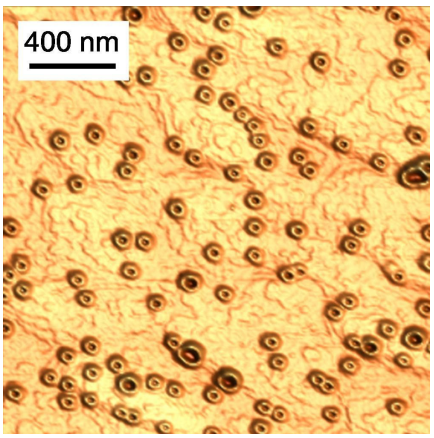


**Figure 4.1.** AFM image of an uncapped sample of InAs/GaAs QRs.

ring-like shape is obtained by covering a layer of InAs QDs grown at 540 ºC with a thin GaAs cap (~ 20% of the dot height) followed by an annealing at 500 ºC under $As_2$ flux. Then the nanostructures were buried under a thicker GaAs layer. An atomic force microscopy (AFM) image of the uncapped layer is shown in Figure 4.1, indicating a QR surface density of $7.5 \cdot 10^9$ QRs/cm$^2$. The QR average height is 2 nm and the average lateral size is 50 nm in the $(1\,\bar{1}0)$ direction. The lateral size is 20% smaller in the $(110)$ direction, due to the preferential In diffusion along the $(1\,\bar{1}0)$ direction. Cross sectional scanning tunneling microscopy (X-STM) images reveal that the QRs keep their ring-like shape after capping, with an increased in-plane asymmetry [157]. Oscillatory persistent currents related with Aharonov-Bohm effect have been observed in this kind of QRs, demonstrating the ring shape of the confinement potential [6]. The epitaxial material was grown by Dr. D. Granados and Dr. J.M. García at *Instituto de Microelectrónica de Madrid (CSIC)*. More details about the growth process can be found in [49].

A PC microcavity based on a triangular lattice of air holes was patterned by electron-beam lithography and dry etching. The PC structure was fabricated by Dr. L. J. Martínez at the *University of California, Santa Barbara*. The hole diameter is $2r = 140\ nm$ and the lattice constant is $a = 230\ nm$ (see Figure 2.5). Air suspended membranes were realized by sacrificial etching of an underlying AlGaAs layer. These parameter values result in a photonic bandgap that ranges from 736 nm to 952 nm. The schematic structure of the sample pre- and post-PC fabrication processes are shown in Figure 4.2. The cavity is formed by a missing hole in the PC. A slight inward shift of its nearest neighbours truncated holes is performed in order to increase the Q factor of the resonant modes. This kind of microcavity is known as *H1 calzone* PC microcavity [158]. In Figure 4.3 SEM images of the fabricated PC microcavity are shown. The mode volume

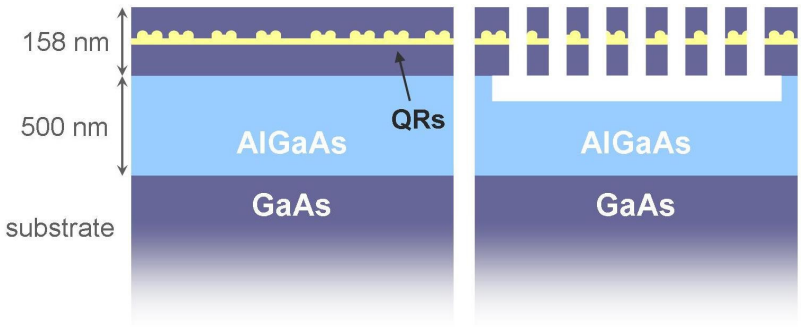


**Figure 4.2.** Sample structure scheme. Left: pre-PC fabrication. Right: post-PC fabrication.

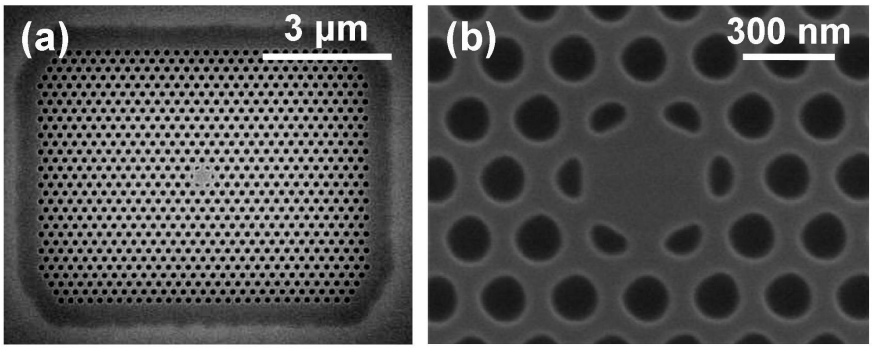


**Figure 4.3.** SEM images of the H1 calzone PC microcavity. (a) Complete PC structure. (b) Detail of the cavity structure.

for this microcavity is around $8 \cdot 10^{-3}$ $\mu m^3$. More details about the PC microcavity fabrication can be found in [159].

A total of 360 PC microcavities (36 rows x 10 columns) of different types were fabricated based on a triangular lattice of air holes. The fact that self-assembled QRs are randomly distributed and emit over a wide energy range reduces significantly the probability of finding one QR located spatially and spectrally near the CM field maximum. A large amount of H1-PC microcavities were studied trying to find coupling between a QR and the cavity resonance. Good results were only obtained from the H1 calzone microcavity described in the previous paragraph.

## 4.2. Optical characterization of the H1 calzone microcavity

Ideally, the lowest energy CM of a H1 calzone PC microcavity is formed by a doubly degenerate dipole mode. The two mode components are cross-polarized (with X and Y

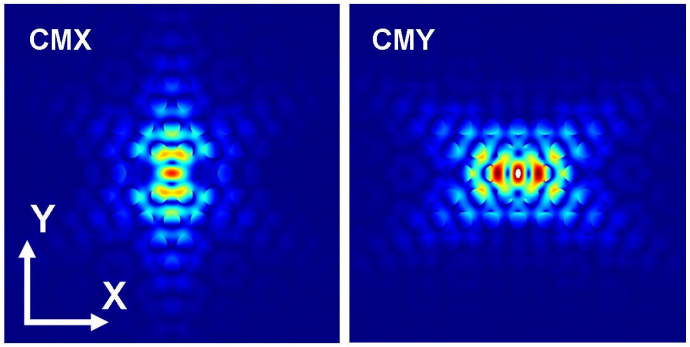


**Figure 4.4.** Spatial distribution of the electric field intensity for the lowest energy modes of a H1 calzone PC microcavity calculated by 3D-FDTD (finite-differences time-domain) by Dr. L. J. Martínez. Left panel: X polarized CM. Right panel: Y polarized CM.

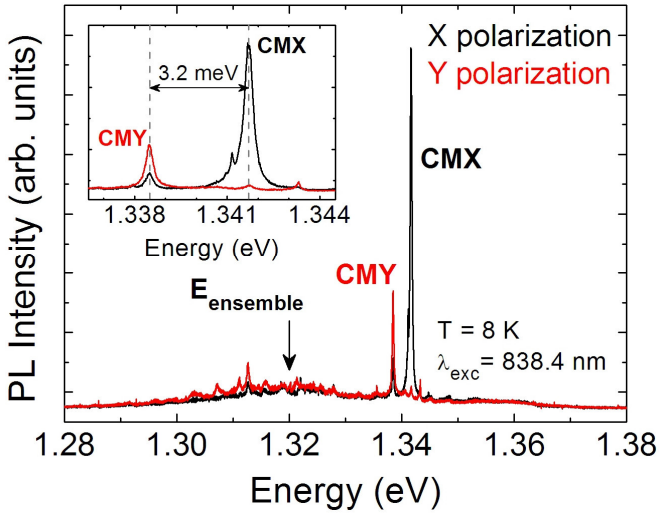


**Figure 4.5.** Polarization dependent spectra of the H1 calzone PC microcavity.

polarization directions) and spatially distributed as shown in Figure 4.4. Due to local fabrication imperfections, the degeneracy is usually lost and the dipole mode splits into two components spectrally separated by ~ 1-2 nm [158]. They will be denoted as CMX and CMY.

Figure 4.5 shows the polarization resolved spectra of the cavity studied in this chapter, taken with the excitation energy above the WL emission (1.455 eV). The two components of the lowest energy mode are separated by ~ 3.2 meV (as shown in the inset) and exhibit orthogonal linear polarization along X and Y directions respectively (marked in Figure 4.4). The Q factor of the cavity under study is estimated from the spectral width of the CM with equation (2.2). The values of the linewidths obtained

from Figure 4.5 are 350 μeV for CMX and 290 μeV for CMY, giving quality factors of 3800 and 4600 respectively. The QR ensemble PL emission ranges from 1.28-1.37 eV having its maximum intensity at 1.32 eV. Sharp peaks corresponding to the emission of individual QRs are observed.

## 4.3. Single photon emission by a quantum ring in a photonic crystal membrane

Single photon emission (SPE) has been demonstrated for QD nanostructures in the past years [160-168]. Clear antibunching, i.e. a minimum in the second order auto-correlation function $g^{(2)}(\tau)$ at zero delay time, has been observed for X and XX transitions proving the quantum nature of the emitted light. Photon antibunching under pulsed excitation has been reported recently in GaAs/AlGaAs double QRs [4]. In this section, SPE of an individual InAs/GaAs QR is demonstrated under continuous nonresonant excitation. The use of the continuous excitation allows us to measure, in addition to the antibunching minimum, the characteristic rise times of each QR transition.

All the measurements shown in this section were taken with the micro-PL setup shown in Section 3.6.1 with a single grating spectrometer and a He-Ne laser. The sample temperature was 7 K.

### 4.3.1. Single QR characterization

The power dependent PL spectra of a single QR are shown in Figure 4.6(a) for an excitation intensity range of 0.5-24 μW. The data were normalized to the intensity of the peak labeled X. For the lowest pump powers only one peak at 1.3505 eV can be observed in the spectrum. Upon increasing excitation intensity two additional emission lines arise. For the highest pump power, the peak labeled XX dominates the spectrum.
The three peaks are identified by their intensity evolution which is shown in a double-logaritmic scale in Figure 4.6(b) as a function of the power of the exciting laser. The solid lines are fits to the expression $I \propto P^{\gamma}$. The values of γ will help to determine the origin of each emission line. We obtain γ=1.87, γ=1.02 and γ=1.39 for the peaks at 1.348 eV, 1.3505 eV and 1.3545 eV respectively. The linear and quadratic dependence together with the saturation behaviour at high excitation powers are considered as the fingerprint of the exciton (X) and biexciton (XX) emissions [46]. The peak at 1.3545 eV has been attributed to the positive trion $X^+$ taking into account also its energy relative to X and XX lines (see Section 2.1.1).

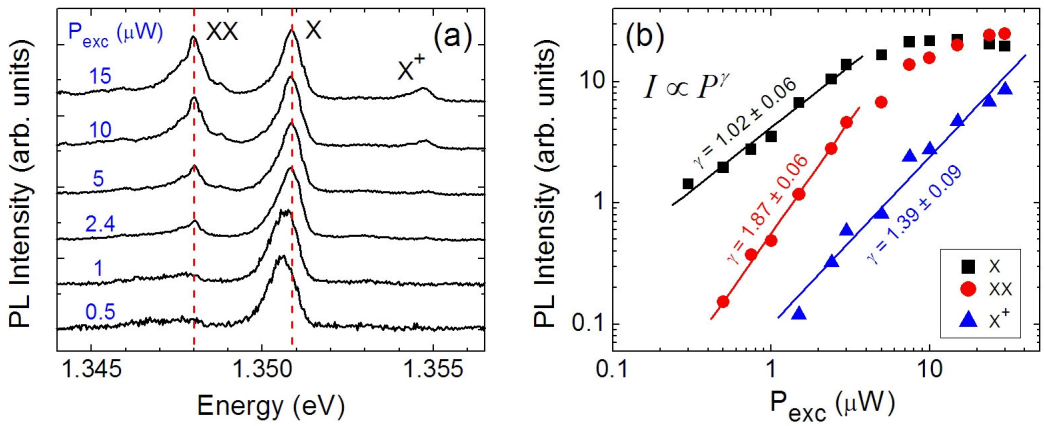


**Figure 4.6.** (a) Power dependent PL spectra of a single QR not coupled to the cavity (T = 7 K). The data are normalized to the X intensity. (b) PL intensity of X, XX and $X^+$ lines as a function of the excitation power.

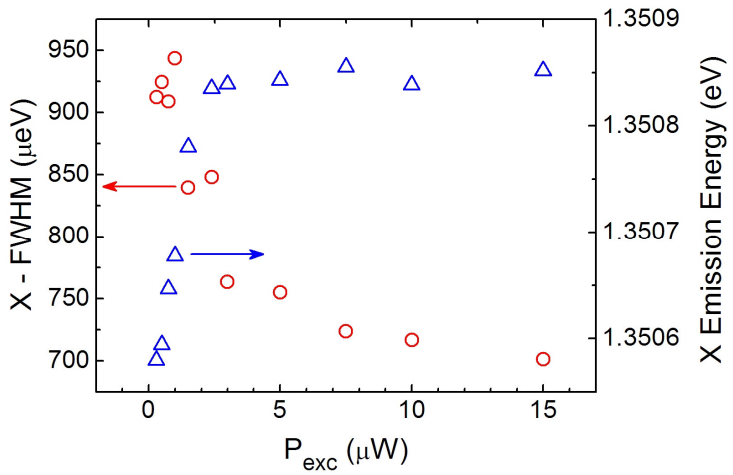


**Figure 4.7.** FWHM and emission energy of X line as a function of the excitation power.

The X and XX line shapes are found to change significantly upon varying the excitation power. The full width at half maximum (FWHM) and the emission energy of the X line is shown in Figure 4.7 as a function of the excitation intensity. The peaks broaden and slightly redshift as the power is decreased. This has been observed also for InAs/AlAs QDs [169] and is explained in terms of sidebands due to acoustic phonon emission. One of the mechanisms that mediate the interaction of the excitons with the long-wavelength acoustic phonons is the piezoelectric (PZ) coupling. This mechanism is demonstrated to produce the appearance of non-Lorentzian sidebands in the zero-phonon line (ZPL) emissions of QDs. At low temperature, these sidebands are more pronounced at the low-energy side, reflecting the higher probability of emitting than

absorbing a phonon. PZ coupling can be screened out by free carriers, whose density increases by increasing the excitation power. Then, at low excitation power, the spectra are dominated by acoustic phonon sidebands. By increasing the power the PZ coupling mechanism is suppressed by screening and the ZPL emission becomes predominant.

### 4.3.2. Photon correlation measurements

The QR described above emits in the high energy tail of the ensemble emission. It is located inside the PC slab but far away from the cavity region. Indeed no CM photons were detected with the laser spot centered at the QR position. However, the presence of the photonic bandgap of the PC provokes an enhancement in the light extraction efficiency which gives PL intensities around 6 times stronger than for the QRs located outside the PC. This enhancement makes possible carrying out the photon correlation measurements in reasonable integration times (several hours).

The second order auto-correlation functions of the X and XX emissions (Figure 4.8) exhibit clear antibunchings. The excitation intensity was fixed at 15 μW in both cases, so that X and XX PL intensities were almost equal. The count rate at each APD detector was around 3000 counts/s. Each profile is the result of around 8 hours of accumulation time, so for a resolution of 128 ps the coincidence counts were around $C = 30$, according to equation 3.12. The signal to noise ratio (SNR) was calculated by the following expression:

$$SNR = \frac{S}{S+B} \tag{4.1}$$

where $S$ and $B$ are the number of signal and background photons respectively measured from the corresponding spectrum. The measured SNR was 0.93 in both cases. The measured $g^{(2)}(\tau)$ function is then obtained by normalizing the experimental histogram ($G^{(2)}(\tau)$) with the coincidence counts ($C$) corrected by the SNR as follows [167, 168]:

$$g^{(2)}_{meas}(\tau) = \frac{G^{(2)}(\tau)/C - \left(1 - SNR^2\right)}{SNR^2} \tag{4.2}$$

In the HBT experiment, the time resolution of the APD detectors, the TAC and the MCA may affect the correlation measurements, especially the correlation dip $g^{(2)}(0)$. In order to obtain reliable values of that parameter the instrumental response function (IRF) of the HBT setup was measured using a 2-ps-pulsed Ti:sapphire laser. The function that was found to fit best the IRF is of the form [167]:

$$IRF(\tau) = \frac{1}{2\sigma}\exp\left(-\frac{|\tau|}{\sigma}\right) \tag{4.3}$$

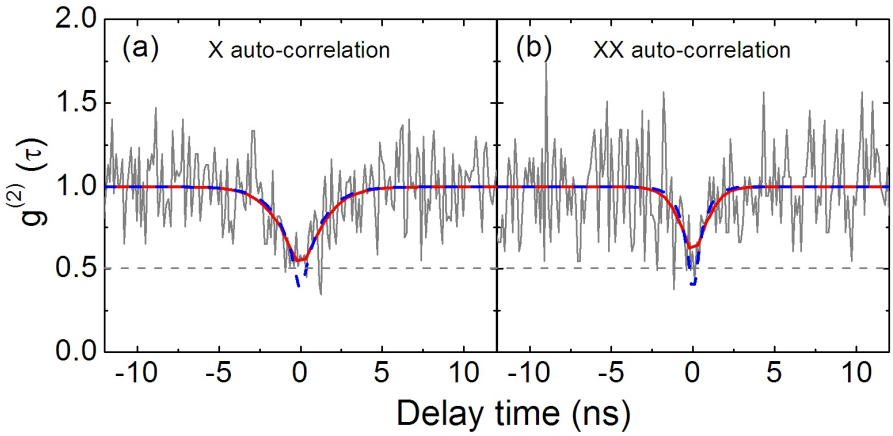


**Figure 4.8.** Auto-correlation functions of X (a) and XX (b) emission lines of a single InAs QR. The red solid lines are fits convoluted with the IRF. The dashed blue lines correspond to the unconvoluted functions.

where the response time is $\sigma = 0.5\ ns$. Then, the measured correlation function is given by the convolution of the real $g^{(2)}(\tau)$ given by equation (3.13) and the system response (4.3) [166]:

$$g^{(2)}_{meas}(\tau) = \int_{-\infty}^{\infty} IRF(\tau - \tau')\, g^{(2)}(\tau')\, d\tau' \tag{4.4}$$

from which the following expression is derived:

$$g^{(2)}_{meas}(\tau) = 1 - \beta\left[\frac{\tau_R^2 \sigma}{\sigma^2 - \tau_R^2}\left(\frac{1}{\tau_R}\exp\left(-\frac{|\tau|}{\sigma}\right) - \frac{1}{\sigma}\exp\left(-\frac{|\tau|}{\tau_R}\right)\right)\right] \tag{4.5}$$

The red solid lines in Figure 4.8 are fits to the expression given in equation (4.5). The blue dashed curves correspond to the unconvoluted function $g^{(2)}(\tau)$ (equation (3.13)). It is clear that in both X and XX auto-correlation measurements the $g^{(2)}(0)$ values are increased by the instrumental response. In contrast, the characteristic rise times are not especially affected. The X and XX rise times $\tau_R$ and the $g^{(2)}(0)$ values obtained from the fits with equation (4.5) are presented in Table 4.1.

| | X | XX |
|---|---|---|
| $\tau_R$ (ns) | 1.2 | 0.6 |
| $g^{(2)}(0)$ | 0.34 | 0.27 |

**Table 4.1.** Characteristic rise times and $g^{(2)}(0)$ values obtained from the fits of X and XX auto-correlation functions.

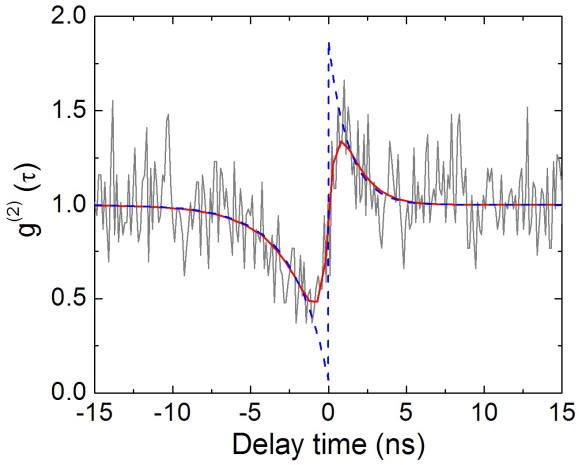


**Figure 4.9.** XX-X cross-correlation function of a single InAs QR. The red solid line is a fit convoluted with the IRF. The dashed blue line corresponds to the unconvoluted function.

The values of $g^{(2)}(0)$ below 0.5 are indicative of SPE. The characteristic rise time is longer for the X emission than for the XX one for similar emission intensities. This effect has been previously observed for QDs [164, 168] and can be explained as follows. For an empty QR, the capture of an *e-h* pair can result in either a bright or a dark exciton ($\left| X_{x,y} \right\rangle$ and $\left| DX_{\pm} \right\rangle$ respectively in Figure 2.2). Instead, the capture of a second *e–h* pair by any exciton (either bright or dark) always results in an optically active biexciton. As the excitation power during the experiments was set to have almost the same X and XX PL intensities, the recharging time must be fast enough to expect a higher probability of emitting two consecutive XX photons with short time delay than for X photons.

The XX-X cross-correlation function is shown in Figure 4.9. The pump power and the integration time were the same as in the auto-correlation measurements. Start and stop signals are given by the XX and X photon detection, respectively. A different behaviour is observed for positive and negative time delays giving rise to an asymmetric shape. There is bunching for positive delay time and antibunching for negative delay time. This asymmetric shape is the signature for the cascade emission of a biexciton photon followed by an exciton photon (Figure 2.2) [170]. The bunching behaviour is the consequence of an increase in the X emission probability right after the XX emission. In the same way, the antibunching feature comes from the following argument: when a X photon is detected, the system has returned to the ground state and then two *e–h* pairs have to be captured for a XX photon to be emitted. In this way, the cross-correlation measurement allows us to identify unambiguously these two lines as exciton and biexciton of the same QR.

The full line-shape analysis requires solving a rate equation system involving several QR states with up to nine parameters [171]. Instead, a simple exponential fit has been used to estimate the correlation times. Again the red solid curve is a fit taking into account the convolution with the IRF and the blue dashed line is the deconvoluted function. An asymmetry is also found in the characteristic times for positive and negative delays. The value found for negative and positive delay times are 2.4 ns and 1.3 ns, respectively. This time asymmetry is the consequence of the different rise times found in the auto-correlation functions of X and XX.

The high noise level in all the photon correlation profiles, the auto- and cross-correlation measurements is mostly due to the low signal detected in each APD detector (only 3000 counts/s), which requires long accumulation time.

## 4.4. Individual quantum ring-cavity coupling

The determination of the coupling regime (strong or weak) between a quantum emitter and a cavity requires the study of the optical properties of their emissions as the detuning changes. In this section the individual coupling of two QRs located near the cavity center are demonstrated by PL intensity enhancement, time resolved measurements and effects in the polarization of the emission.

All the measurements shown in this section were taken with the micro-PL setup shown in Section 3.6.1 with a single or double grating spectrometer. A He-Ne laser and Ti:sapphire laser were used for continuous excitation and a pulsed diode laser for time resolved measurements. The sample temperature was varied in the range of 7-58 K.

### 4.4.1. Characterization of single QRs near the cavity center

Figure 4.10 shows the PL emission spectra at low temperature under resonant excitation in the vicinity of the cavity for X and Y polarizations. The CMX emission is observed together with two intense sharp lines with almost opposite polarizations. These two lines have been identified by their power dependence (inset of Figure 4.10) as the exciton emissions of two different QRs (named QR-A and QR-B). The approximate location of each QR with respect to the CMX maximum has been roughly estimated by maximizing their PL intensities as a function of the laser spot position with an accuracy of 300 nm. QR-A and QR-B are at 0.5 and 0.9 μm respectively away from the CMX maximum almost in opposite directions along the Y axis. The QR positions are schematically shown in Figure 4.11.

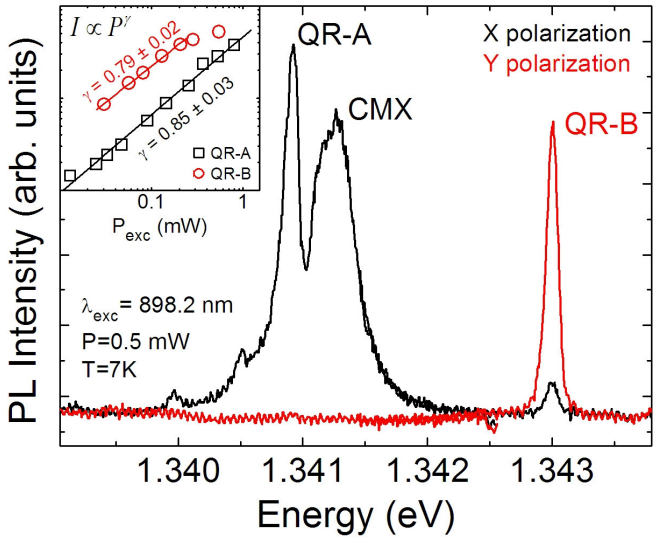


**Figure 4.10.** LT PL spectra of QR-A, QR-B and CMX for X (black) and Y (red) polarizations. Inset: power dependent PL intensities of QR-A and QR-B.

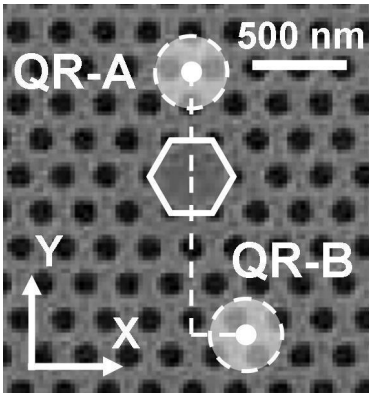


**Figure 4.11.** SEM image of the H1 calzone PC microcavity with the approximate location of QR-A and QR-B.

By fitting the different peaks to Gaussian curves, the following linewidths are obtained:

$$\begin{aligned} &\text{CMX:} \quad \kappa = 340 \pm 6\ \mu eV \\ &\text{QR-A:} \quad \gamma_A = 170 \pm 4\ \mu eV \\ &\text{QR-B:} \quad \gamma_B = 100 \pm 2\ \mu eV \end{aligned} \tag{4.6}$$

No FSS has been observed for the emissions of these two QRs. In fact, both lines present linear polarization as will be shown in Section 4.4.4. Besides, QR-B can be excited only with Y linear polarization of the laser. This can be the consequence of the

strong anisotropy typical for these QRs [157], which can result in large energy differences between successive electronic states. In this way, the emission energies of the two orthogonally polarized X lines could be spectrally separated by a large amount.

### 4.4.2. Effects of the coupling on the PL spectra

In order to determine the possible coupling of each QR with the cavity, the PL emission spectra have been recorded across the resonance of CMX with each QR. Tuning the QR and CM energies has been performed by changing the sample temperature and by Xe thin film deposition (see Section 3.6.3).

Figure 4.12(a) shows the PL spectra of QR-A and CMX for increasing temperature. The CMX was previously shifted to lower energy than the QR-A by Xe adsorption in

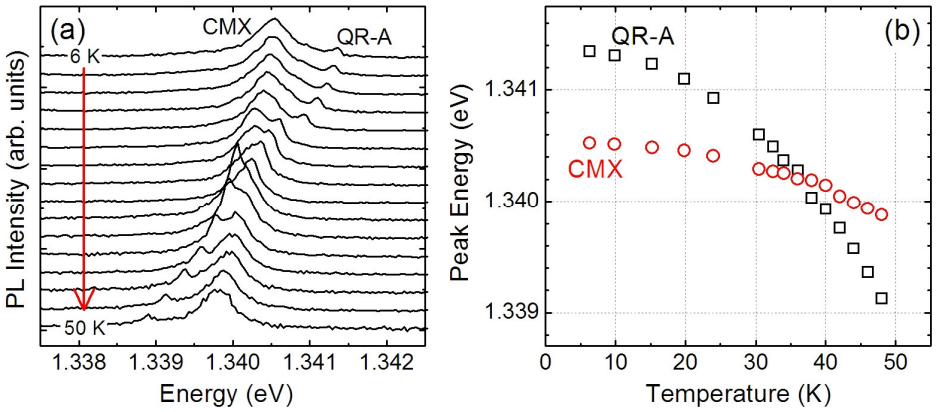


**Figure 4.12.** (a) PL spectra of QR-A and CMX for different temperatures. (b) Energies of QR-A and CMX emission lines as a function of the temperature.

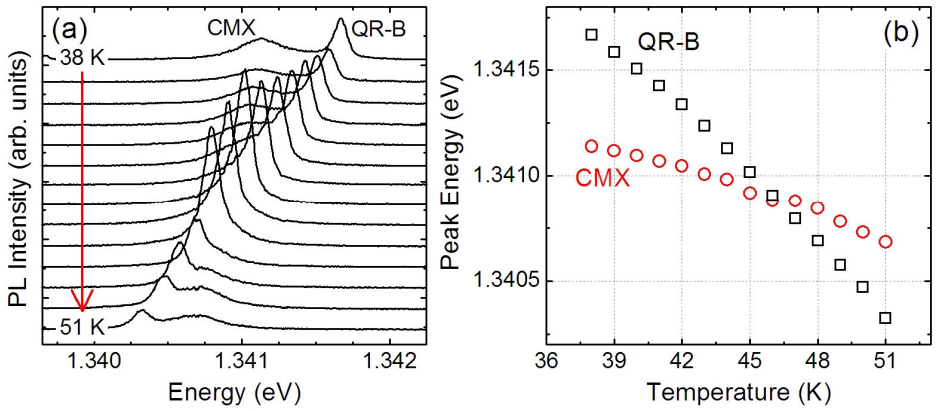


**Figure 4.13.** (a) PL spectra of QR-B and CMX for different temperatures. (b) Energies of QR-B and CMX emission lines as a function of the temperature.

order to scan both positive and negative detunings ( $\Delta = E_{QR} - E_{CMX}$ ). In Figure 4.12(b) the peak positions of both peaks are plotted as a function of temperature. Similar PL spectra are shown in Figure 4.13 for QR-B. In this case, only the temperature change was used to tune the QR-B emission into resonance with the CMX. No measurable anticrossing is observed in any case which would indicate in principle weak coupling regime for each QR with the CMX. The experimental uncertainty of the energies would give an upper limit of 40 and 30 μeV for QR-A- and QR-B-CMX coupling strengths ($g_{A,B}$). However, as it was explained in Section 2.1.3, strong coupling can be still present even in the absence of a visible anticrossing [68, 69]. The unambiguous evidence of weak coupling regime will be given in Section 4.4.3.

The first evidence of the individual QR coupling to the cavity is given by the enhancement in the PL intensity experimented by the QR excitons as they approach the CMX energy. Figure 4.14 shows the relative intensities $I_{QR}/(I_{QR}+I_{CMX})$ for both QRs as a function of the detuning. Significant intensity increases are observed at zero detuning for both QRs. This result is a consequence of the Purcell effect that will be demonstrated in the next section. It produces an enhancement in the spontaneous emission rate that is reflected in an increase in the PL intensity.

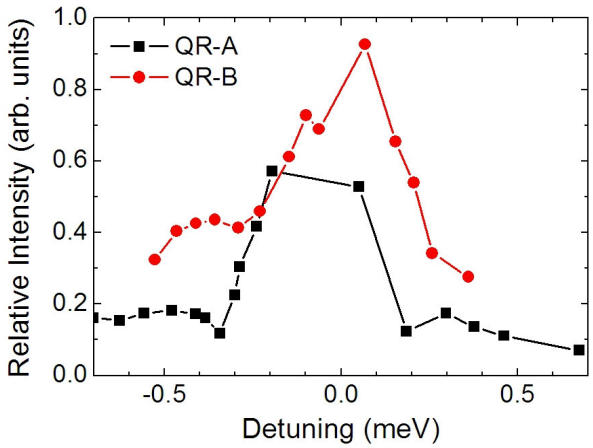


**Figure 4.14.** Relative intensity of QR-A and QR-B as a function of the detuning.

Another experimental evidence of the coupling in the case of QR-A is given in Figure 4.15, where the PL intensities of QR-A and CMX lines are shown as a function of the excitation power for different temperatures, i.e. for different detunings. The corresponding spectra are shown in Figure 4.15(a). For large detuning (panel (b): 35 K → Δ = -1.08 meV), the power dependence of the QR-A exciton line shows a linear increase with a slope of 1.08 before saturation at around 10 μW. In contrast, the CMX

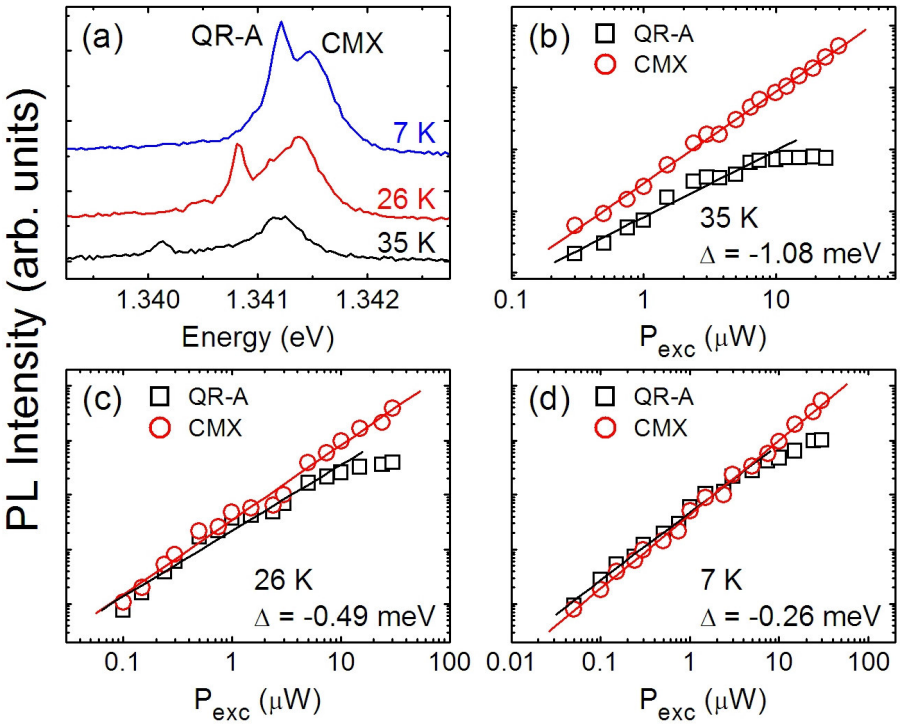


**Figure 4.15.** (a) PL spectra of QR-A and CMX for different temperatures. (b-d) Power dependence of the PL intensities of QR-A and CMX for the three temperatures presented in (a).

line presents a super-linear dependence with a slope of 1.48 without saturation. As the detuning is decreased (panel (c): 26 K → Δ = -0.49 meV), the slope of the QR-A power dependence increases to 1.2 while the CMX one decreases to 1.37. For even smaller detuning (panel (d): 7 K → Δ = -0.26 meV) the slopes of both lines become almost equal with values of 1.24 and 1.36 for QR-A and CMX respectively. This result suggests that QR-A and CMX states become mixed as the detuning is decreased.

### 4.4.3. Effects of the coupling on the QR lifetime: Purcell effect

The existence of the coupling of each QR to the cavity can be definitely proved by measuring the modification of the spontaneous emission rate of the QRs as they approach the CMX energy. This is the Purcell effect explained in Section 2.1.3 and is reflected in the detuning dependence of the lifetime of the QR excitons.

Time resolved PL measurements of both QR excitons have been performed as a function of the detuning using the TCSPC technique presented in Section 3.3. The

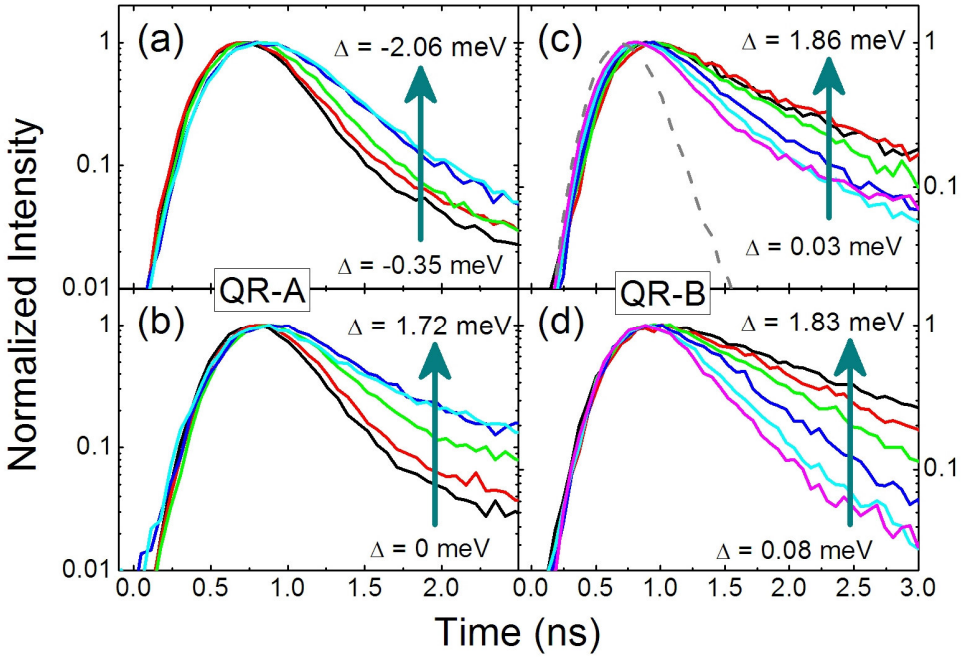


**Figure 4.16.** Time resolved spectra of QR-A (a,b) and QR-B (c,d) for different detunings. The change in the detuning was achieved by temperature changing (a,c,d) and Xe deposition (b). The dashed gray line in (c) corresponds to the time resolved measurement of the laser pulse.

results are shown in Figure 4.16 in a semilogaritmic scale. Left (a, b) and right (c, d) panels correspond to QR-A and QR-B respectively. Results of QR-A for negative detunings ($E_{QR}<E_{CMX}$) are presented in (a), where the increasing temperature provokes an increase in the absolute value of Δ. The results for positive detunings are shown in panel (b) where several cicles of Xe thin film deposition were used while maintaining the same sample temperature (8 K). The time resolved PL spectra for QR-B for different temperatures for X and Y polarizations are presented in (c) and (d) respectively. In this case only positive detunings could be reached, as the temperature needed to change the detuning sign was too high (around 50 K) for the PL to survive. The dashed gray line shown in (c) is the time resolved measurement of the laser pulses. A clear reduction of the lifetime is observed in all figures when the detuning approaches to zero. The values of the lifetime τ were obtained by fitting each curve with a simple exponential decay. The detuning dependent lifetimes for both QRs are presented in Figure 4.17, where the detuning scales have been shifted by the energy difference between the emission of QR-A and QR-B, which is 2.08 meV. Bottom and right scales correspond to QR-A while upper and left ones to QR-B. For QR-A, the lifetime τ varies from 0.3 ns for small

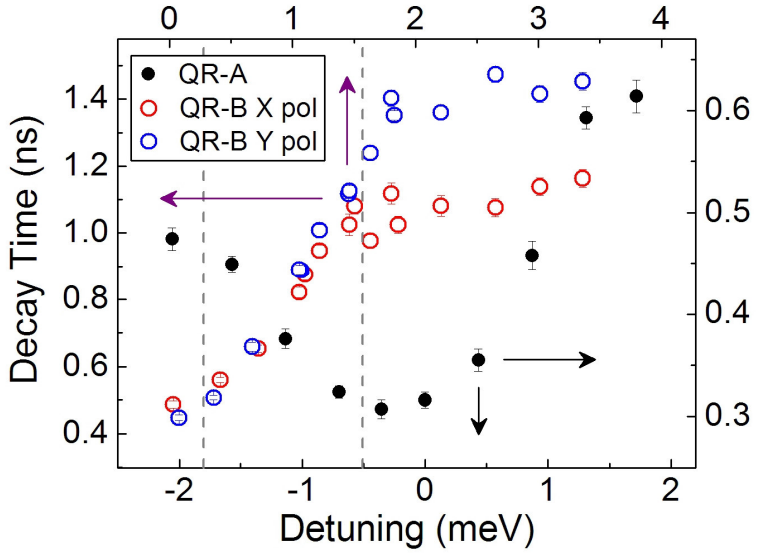


**Figure 4.17.** Decay lifetime of the QR emissions as a function of the detuning. The detuning scales are shifted by the energy difference between the QR emissions. Down and right (up and left) scales correspond to QR-A (QR-B).

detunings to 0.6 ns for large ones, which correspond to the lifetime only influenced by the PC band structure. In the case of QR-B, the lifetime varies from 0.4 ns at almost zero detuning for both polarizations to 1.15 and 1.4 ns for X and Y polarizations respectively. For QR-B, the data in the detuning range of 1.8-3.4 meV were taken at 8 K with different deposited amounts of Xe gas.

Due to the shift in the detuning scales in Figure 4.17, points separated vertically correspond to measurements performed with the same CMX emission energy. In other words, for a specific emission energy of the CMX, time resolved measurements were performed in QR-A and QR-B (each one with its own detuning) and the corresponding lifetimes are plotted in Figure 4.17 in the same vertical line. Therefore, in the detuning range between the vertical dashed lines both QRs are *simultaneously* coupled to the cavity mode. This range roughly corresponds to the CMX energy being intermediate between that of QR-A and QR-B. This is an important result whose consequences will be shown in Section 4.5 where the cavity will be shown to act as a mediator of an effective interaction between the QRs.

The coupling strengths $g_{A,B}$ can be estimated from the total decay rate increase. With the combination of the equations (2.21) and (2.23), the detuning dependent total SE rate is found to be given for large detunings ($\Delta >> \kappa, g$) by [76]:

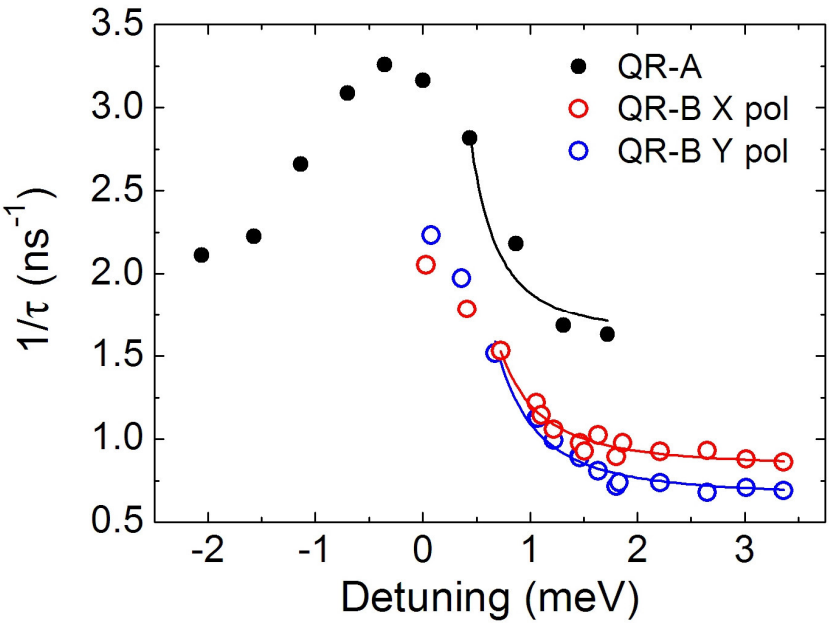


**Figure 4.18.** Total SE rate of both QRs as a function of the detuning. The solid lines are fits to eq. (4.7).

$$\frac{1}{\tau} = \frac{1}{\tau_{PC}} + \frac{4g^2}{\kappa} \frac{\kappa^2}{4\Delta^2 + \kappa^2} \tag{4.7}$$

where $\tau_{PC}$ is the lifetime of the QR exciton in the PC structure.

In Figure 4.18 the SE rate is plotted as a function of the detuning. The solid lines correspond to fits of the experimental data to equation (4.7) taking the linewidth κ from equation (4.6). The fits give the following values for the coupling strengths:

$$\begin{aligned} g_A &= 28 \pm 4 \ \mu eV \\ g_B &= 29 \pm 1 \ \mu eV \end{aligned} \tag{4.8}$$

Comparing these values with the linewidths κ and γ, we have:

$$\begin{aligned} |\kappa - \gamma_A| &= 170 \ \mu eV \quad > \quad 4g_A = 112 \ \mu eV \\ |\kappa - \gamma_B| &= 240 \ \mu eV \quad > \quad 4g_B = 116 \ \mu eV \end{aligned} \tag{4.9}$$

Therefore, according to equation (2.18), we can conclude that both QRs are weakly coupled to CMX.

The data from Figure 4.18 can also be used to extract the coupling efficiency of the emission of both QRs into the CM, described by the $\beta$-factor [172]:

$$\beta = \frac{\Gamma_{res} - \Gamma_{non-res}}{\Gamma_{res}} \tag{4.10}$$

where $\Gamma_{res}$ and $\Gamma_{non\text{-}res}$ are the SE rates of the QR on-resonance and off-resonance with the CM respectively. A $\beta$-factor of 50% has been obtained for QR-A, while for QR-B it has found to be 60% and 70% for X and Y polarizations respectively.

### 4.4.4. Effects of the coupling on the polarization of the QR emission

The coupling of the CMX to the QRs also influences the polarization properties of the QR emissions. Different polarization behaviours are found in each QR as the detuning is varied.

The temperature dependent PL emission of QR-A is shown in Figure 4.19 for both X (black lines) and Y (red lines) polarizations. At low temperature (7 K), the QR-A emission energy is close to the CMX one and is fully X polarized. As the temperature is increased, the QR-A emission moves away the CMX and approaches the CMY emission. The QR-A preserves its X polarization even when it is very close to CMY at 55 K (the QR-A emission energy is marked by the black arrow). This is clearly shown in the inset of Figure 4.19 for higher excitation intensity. This result agrees with the one reported by *Oulton et al.* [30], where QDs coupled to a L3 PC microcavity maintain their polarization parallel to one of the CMs even for large detunings (see Section 2.1.3).

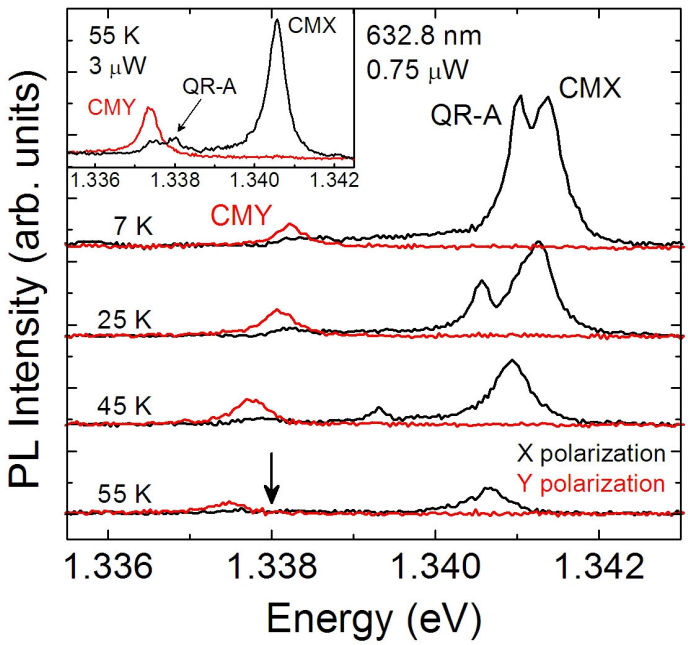


**Figure 4.19.** Temperature dependent PL spectra of QR-A, CMX and CMY. Black (red) lines correspond to X (Y) polarization. The QR-A energy at 55 K is marked by the arrow. Inset: PL spectra at 55 K and higher excitation power.

In contrast to QR-A, QR-B emission changes its linear polarization axis as the detuning between QR-B and CMX is varied. Figure 4.20 displays the polarization polar plots of QR-B emission for different negative and positive detunings and similar excitation conditions. Tuning was carried out by changing the sample temperature. The polar plots of the CMX emission are also shown. The data are normalized to unity and the radial scale starts at zero intensity in all cases. A clear rotation of the polarization angle $\phi$ (defined in panel (c)) of QR-B emission is observed as a function of Δ, while CMX maintains its 95 % X polarized emission. QR-B emission exhibits a predominant Y polarization at large detunings (Figure 4.10 and 4.20(a)). This polarization progressively rotates towards X as Δ is decreased and changes its sign for negative Δ (Figure 4.20 (g-l)). The polarization rotation is more clearly shown in Figure 4.21, where the emission polarization angle of QR-B is plotted as a function of the detuning. A continuous change of $\phi$ in the +80º/-80º range is observed with sign reversal for negative detunings. To discard any possible thermal effect on the QR strain as the source of the polarization rotation, measurements at fixed temperature were included (blue squares) using Xe thin film controlled deposition to modify the CMX energy. The polarization degree $P = \frac{I_{MAX} - I_{MIN}}{I_{MAX} + I_{MIN}}$ is also presented in Figure 4.21. Its value varies between 0.6 and 0.8 in the detuning range studied, without showing a clear trend as a function of Δ. The influence of CMY on the QR-B polarization angle is not expected to be important, as its detuning with respect to CMY changes from 2.6 to 5.1 meV in the temperature range corresponding to Figure 4.21. The present result demonstrates the continuous control (including sign) of the polarization angle of a QR coupled to a cavity.

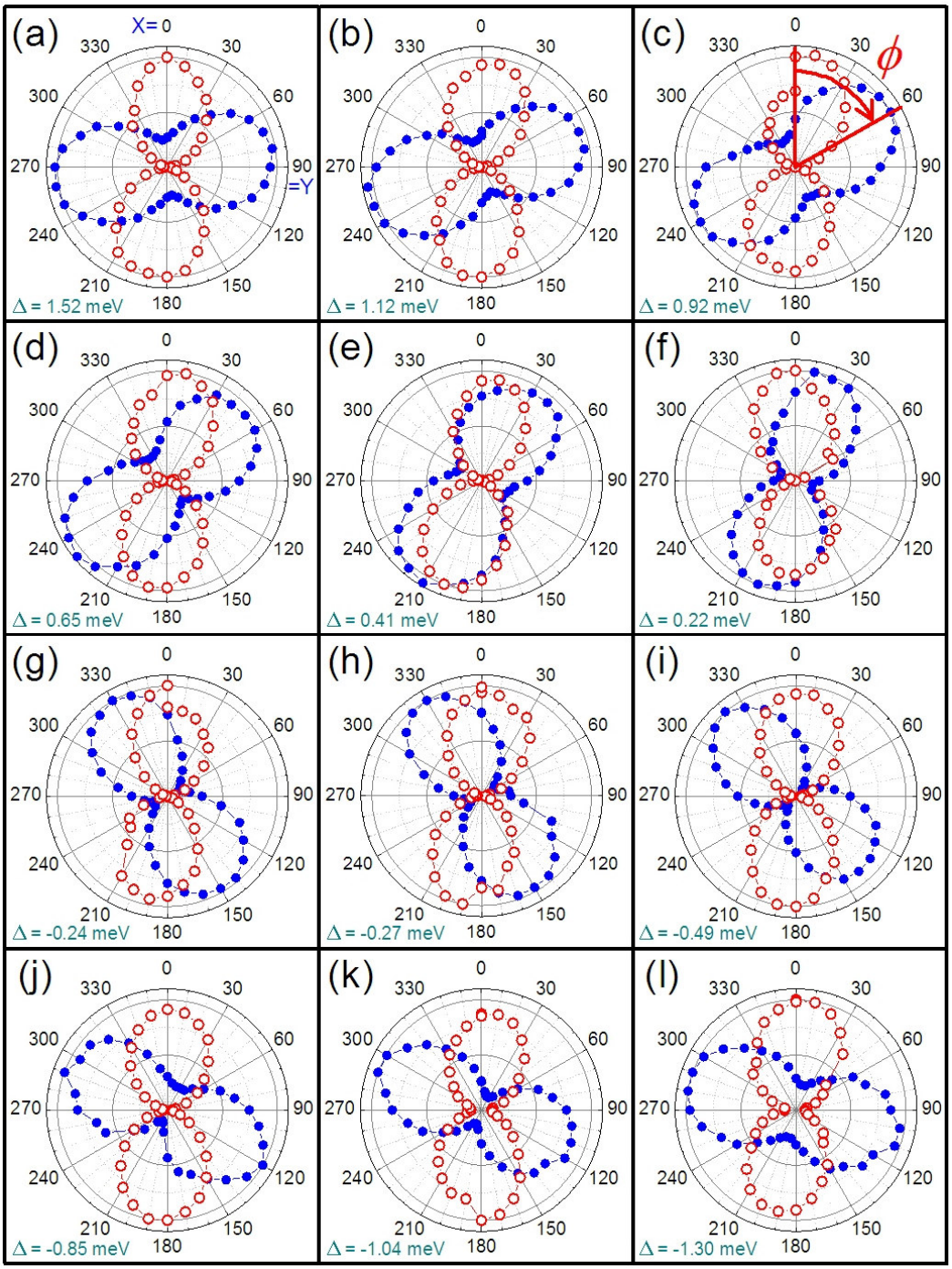


**Figure 4.20.** QR-B polarization polar plots for different detunings (blue circles). The detuning values are given by the green label in each case. CMX polar plots are also included (red open circles). The data are normalized to unity. The polarization angle $\phi$ is defined in panel (c). $\phi$ = 0º (90º) corresponds to X (Y) polarization.

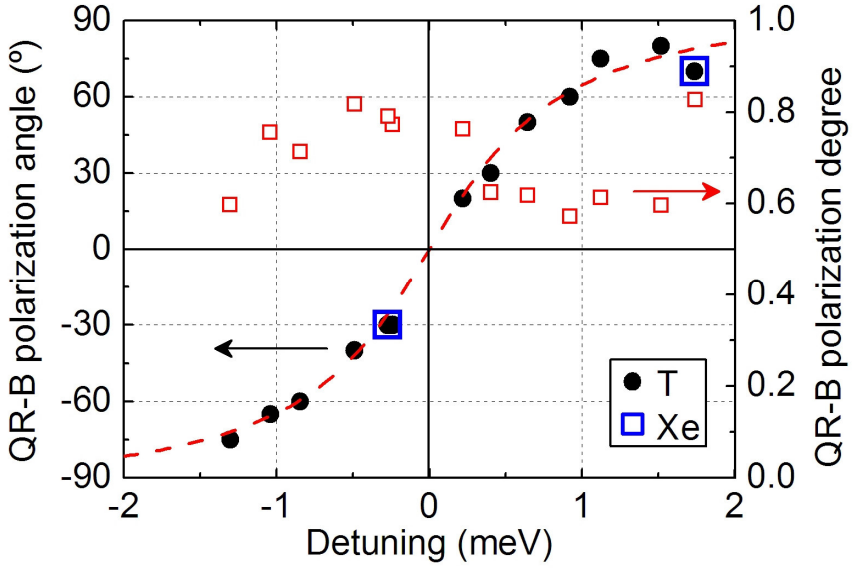


**Figure 4.21.** Polarization angle (black dots) and polarization degree (red open squares) of QR-B emission as a function of its detuning. The detuning was varied by changing the sample temperature. Blue squares correspond to measurements at fixed temperature but changing the detuning by Xe thin film deposition.

Comparison with the results reported by *Daraei et al.* [28] for QDs in an elliptical micropillar cavity (see Section 2.1.3) is not straightforward due to an important difference between both systems: while PC microcavities emit both cavity- and QD-photons in the same direction (perpendicular to the PC slab), in micropillar cavities QD-photons are mainly emitted along their axis (the usual collection direction) and cavity-photons are mainly emitted perpendicular to it (leaky modes). *Daraei et al.* show that the QD emission becomes parallel to that of the spectrally closest CM by only measuring the polarization ratio $(I_X-I_Y)/(I_X+I_Y)$ as a function of the detuning. Then, unlike the results presented in this section, their measurements cannot demonstrate eventual changes in the polarization angle, as two possible sequences, presented in Figure 4.22, would give the same behaviour of the polarization ratio.

One possible origin of the observed polarization rotation could be the preferential enhancement of the QR emission polarized parallel to the cavity mode, due to the Purcell effect, as the detuning is reduced. The sum of two dipoles that are not strictly orthogonal can produce a change in the polarization angle. However, considering the large difference in the polarization angle (at least 80º) the resulting polarization degree should decrease strongly for any significant polarization rotation. This situation is illustrated in Figure 4.23, where two dipoles (black and blue lines) with an angle

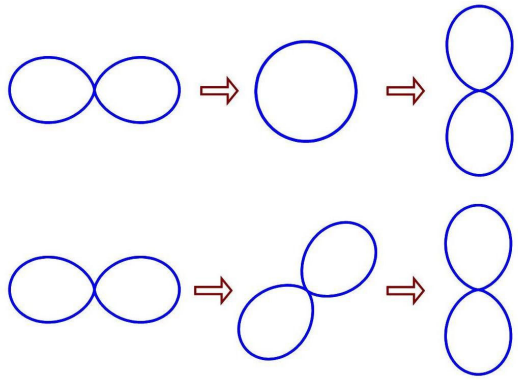

**Figure 4.22.** Possible sequences of polarization which would give the same behaviour of the polarization ratio $(I_X-I_Y)/(I_X+I_Y)$.

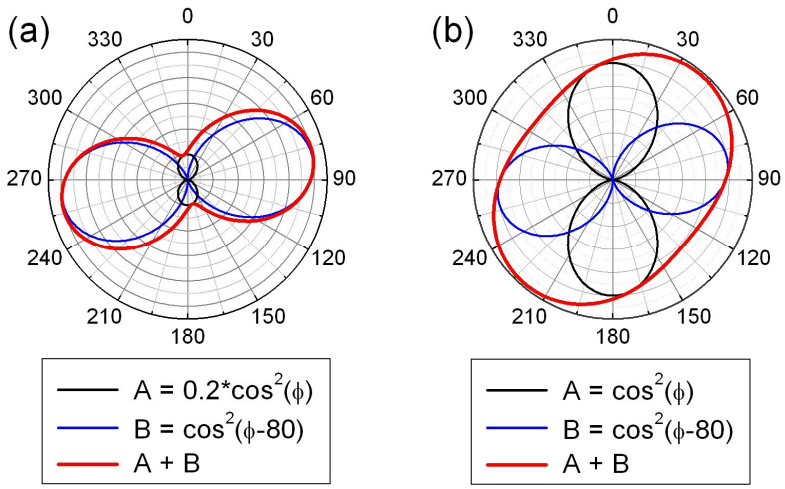


**Figure 4.23.** Sum (red line) of two dipoles (black and blue lines) with an angle difference of 80º for different (a) and similar (b) intensities.

difference of 80º and different (panel (a)) and similar (panel (b)) intensities are summed (red line) and represented in polar plots. For large intensity difference of the two dipoles (Figure 4.23(a)), a small increase in the polarization degree is observed without significant rotation of the polarization angle. In contrast, when the dipole intensities are similar (Figure 4.23(b)), the rotation becomes evident but with a strong decrease in the polarization degree. This decrease is absent in our measurements, as shown in Figures 4.20 and 4.21, so that the preferential enhancement of the QR emission polarized parallel to the CM has to be ruled out as the main origin of the observed polarization rotation, which requires the effective rotation of the emitted dipole (lower diagram of Figure 4.22).

The sign dependence of the polarization angle with the sign of the detuning can be explained qualitatively in terms of hybridization of the bare states of the system: $(1 \quad 0)$ for the CMX and $(0 \quad 1)$ for QR-B. The eigenvalues and eigenstates are obtained by diagonalization of the corresponding Hamiltonian:

$$\hat{H} = \begin{pmatrix} 0 & g \\ g & \Delta \end{pmatrix} \tag{4.11}$$

For positive detunings the eigenstates have the following form:

$$\psi_1 = \frac{1}{\sqrt{1+\left(g/\omega_+\right)^2}} \begin{pmatrix} 1 \\ g/\omega_+ \end{pmatrix} \qquad \psi_2 = \frac{1}{\sqrt{1+\left(g/\omega_-\right)^2}} \begin{pmatrix} g/\omega_- \\ 1 \end{pmatrix} \tag{4.12}$$

while for negative detunings they are:

$$\psi_2 = \frac{1}{\sqrt{1+\left(g/\omega_+\right)^2}} \begin{pmatrix} g/\omega_+ \\ 1 \end{pmatrix} \qquad \psi_1 = \frac{1}{\sqrt{1+\left(g/\omega_-\right)^2}} \begin{pmatrix} 1 \\ g/\omega_- \end{pmatrix} \tag{4.13}$$

where $g = g_{VAC}\sqrt{n}$ with $n$ the number of photons in the cavity state. $\omega_\pm$ are the eigenvalues for the emission frequency:

$$\omega_\pm = \frac{\Delta}{2} \pm \sqrt{\frac{\Delta^2}{4} + g^2} \tag{4.14}$$

As shown in Figure 4.24, the QR-B state evolves into $\psi_1$ with the eigenvalues $\omega_+$ for $\Delta > 0$ and $\omega_-$ for $\Delta < 0$. The polarization angle in each case is given by:

$$\begin{aligned} \Delta > 0 \quad &\rightarrow \quad \phi = \arctan\left(g/\omega_+\right) \\ \Delta < 0 \quad &\rightarrow \quad \phi = \arctan\left(g/\omega_-\right) \end{aligned} \tag{4.15}$$

As the relation $\omega_+(\Delta) = -\omega_-(-\Delta)$ is fulfilled, the sign of the polarization angle must follow then the sign of Δ.

The previous argument explains the sign of $\phi$ in Figure 4.21, but not its detailed dependence on Δ found experimentally. In fact, this model would predict a limit of $\phi$ = ± 45º (depending on the sign of the detuning) of the polarization angle of QR-B together with an opposite polarization rotation in the CMX emission. It is obvious from Figure

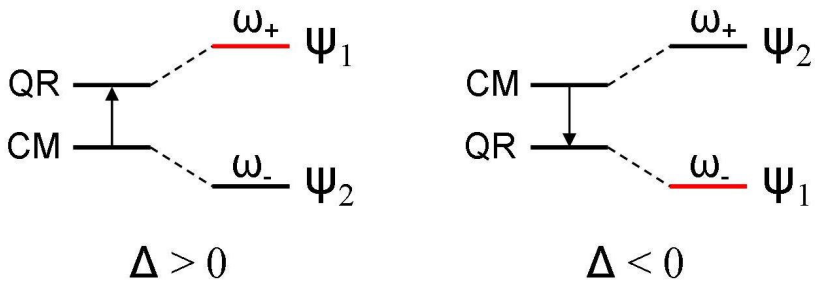


**Figure 4.24.** Hybridized states in the general case for positive (left) and negative (right) detuning.

4.20 that this is not observed in our system. A quantitative explanation of the experimental trend and the invariance of the CMX polarization angle would require the detailed knowledge of the coupling mechanism together with the consideration of other factors, as a high photon occupation of the cavity mode. However, an important conclusion can be obtained from the results presented in this section: even in the weak coupling regime, the polarization of the emission can be used for detecting hybridization of QD and cavity states.

Two possible arguments can be given in order to explain the different polarization behaviours observed in QR-A and QR-B. First, QRs are not symmetric [157] and the intrinsic dipole orientation, which is specific of each QR, can determine their polarization properties. Second, the electric field of the two modes is found to vary strongly in the regions where the QRs are located. Then, QR-A could accidentally lie on a local minimum of the CMY so it does not influence its polarization. In the general case, a combination of these two effects is expected to occur.

### 4.4.5. Photon correlation measurements

Photon correlation measurements have been performed in both QRs and CMX emission transitions. Their second order auto-correlation functions for resonant excitation at the respective *p*-states (see Section 4.5) are presented in Figure 4.25 for different detunings. A narrow (~ 1.3 ns) antibunching dip is observed for QR-B at the center of a wider bunching peak. This bunching is attributed to the enhanced probability of QR recharge after emitting a photon, by the direct photon injection from the cavity and/or the resonant excitation at the *p*-state. Moreover, by comparing the QR-B antibunching peak with the ones of other QRs not coupled to the cavity (see Section 4.3.2), a clear reduction of the width is observed in the QR-B dip indicating a decrease in the characteristic rise time due to the faster recharging of the QR. The fitting of the

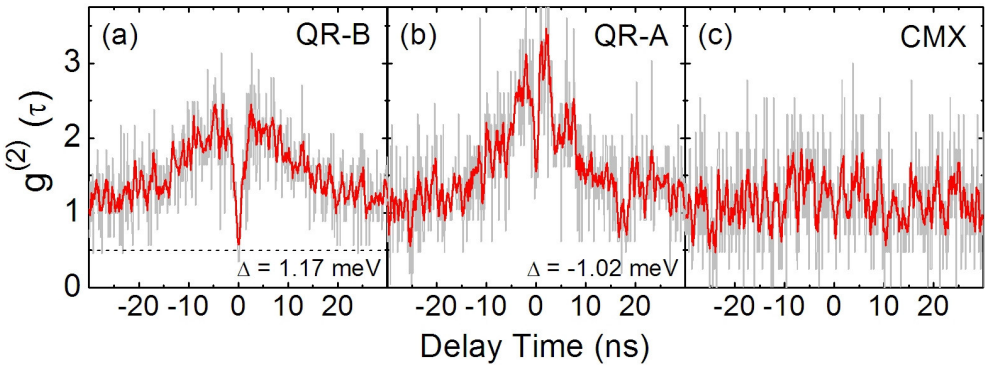


**Figure 4.25.** Second order auto-correlation function of (a) QR-B, (b) QR-A and (c) CMX. The data were recorded at Y (a) and X (b, c) polarizations. The red lines are smoothed curves of the data.

data in order to extract the correct values for $g^{(2)}(0)$ and the characteristic rise time would require again the knowledge of the complicated dynamics of the coupling mechanism. However, a value of around 0.34 for $g^{(2)}(0)$ can be extracted directly from the experimental data. As the convolution with the IRF would give a value even smaller, we can conclude that QR-B presents characteristics of a SPE.

In the case of QR-A, an antibunching peak is also observed together with a wide bunching one. However, the dip is less pronounced and SPE cannot be stated from the experimental data. The CMX auto-correlation function does not show any feature of antibunching.

The auto-correlation measurements of QR-B for different detunings are shown in Figure 4.26. The measurements were recorded for the Y polarization. For detunings between 1.9 and 0.73 meV (Figure 4.26(a-c)) the antibunching peak is clearly observed maintaining $g^{(2)}(0)$ values below 0.5 and similar peak widths. For the smallest detuning (0.28 meV), the antibunching is almost lost probably due to the more efficient photon injection from the cavity mode. Therefore, the present results are encouraging for the development of single photon emitters with precise continuous control of the linear polarization orientation, which would constitute a relevant step for the quantum information applications.

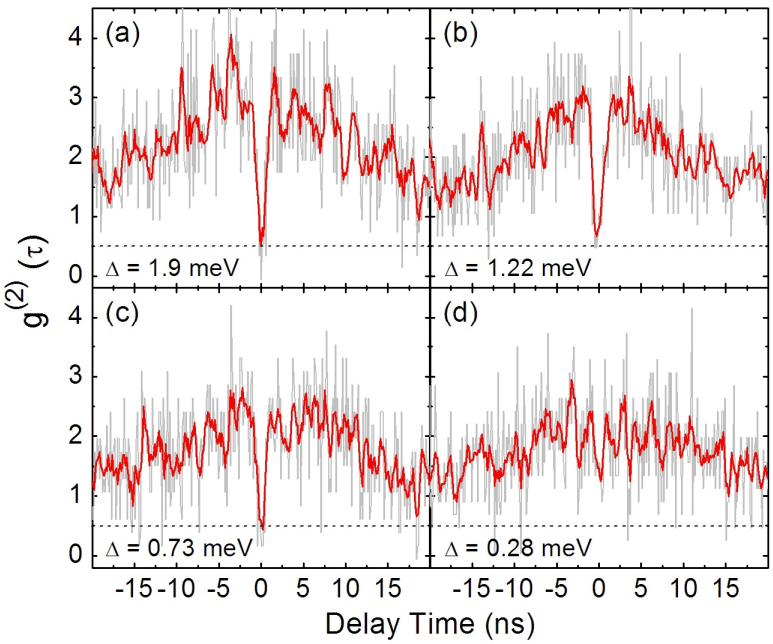


**Figure 4.26.** Second order auto-correlation function of QR-B for different detunings recorded at Y polarization. The red lines are smoothed curves of the data.

## 4.5. Coupling of two distant quantum rings by a photonic crystal microcavity

So far we have studied the individual coupling of two QRs to the CMX. In this section an effective interaction between the two QRs will be shown. As demonstrated in Section 4.4.3, both QRs are simultaneously coupled to the cavity mode over a wide detuning range. In this way, the cavity can act as a mediator in the interaction between them.

The long-distance interaction will be demonstrated by PLE measurements. They were taken with the micro-PL setup shown in Section 3.6.1 with a double grating spectrometer. A Ti-sapphire laser was used for resonant continuous excitation. The sample temperature was varied in the range of 7-37 K

The PLE spectra of both QRs for a wide range of excitation energy are shown in Figure 4.27. The spectra start with an excitation energy of 1.3634 meV with less than 10 cts/s. Then the PLE intensity begins to increase and several resonances are observed in both profiles, the most evident ones being at around 30 and 40 meV. In the following we will focus on the most intense one at 40.2 and 37 meV for QR-A and QR-B respectively. This resonance corresponds to excited states [51] that will be simply called *p-states*.

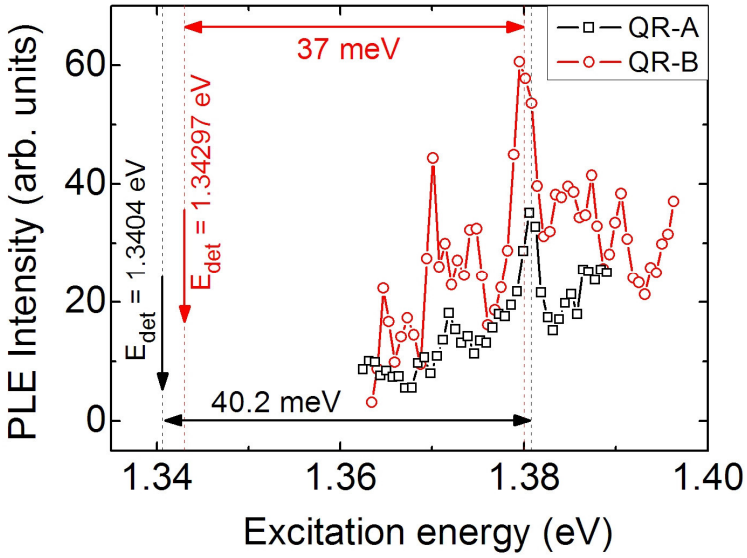


**Figure 4.27.** LT PLE spectra of both QR-A (black) and QR-B (red) for a wide excitation energy range.

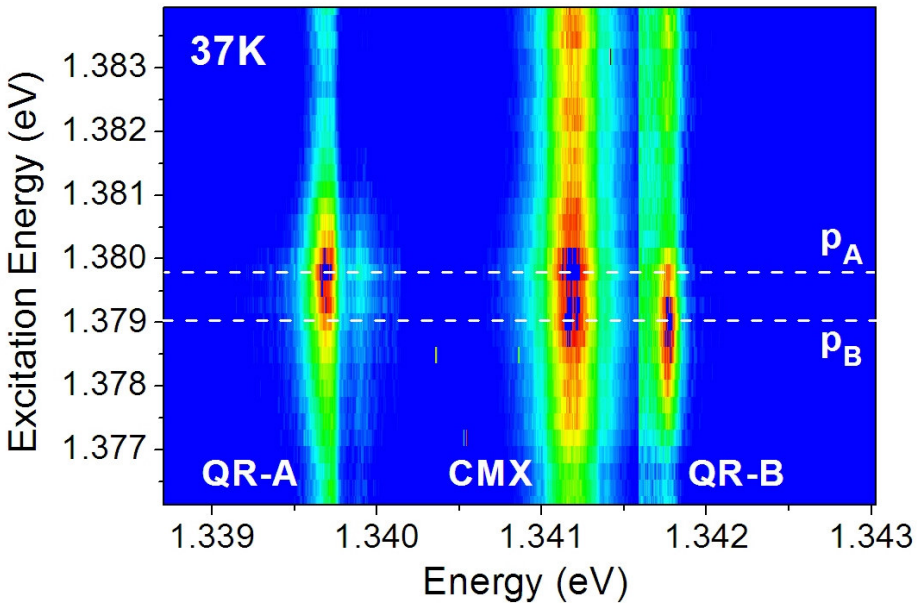


**Figure 4.28.** Emission intensity dependence of QR-A, QR-B and CMX (colour scale) on excitation (vertical axis) and emission (horizontal axis) energies recorded at X polarization and 37K. The excitation power was around 0.2 mW. A different colour scale has been used for each peak. The PLE maxima in QR traces correspond to the *p*-state of each QR.

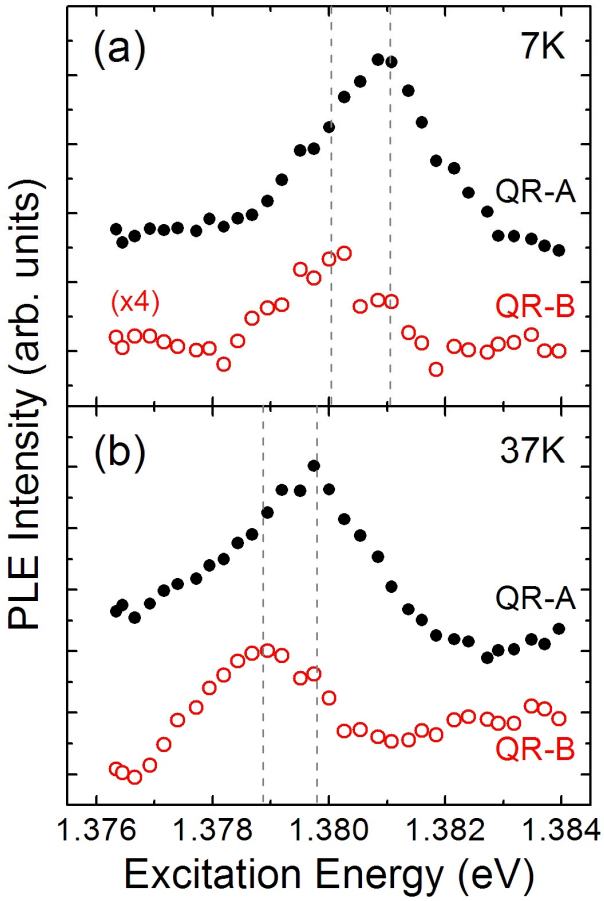


**Figure 4.29.** PLE spectra of QR-A and QR-B for X polarization at (a) 7K and (b) 37K. The excitation intensity was 0.2 mW in both cases. The vertical lines mark the *p*-state energies.

That resonance is shown in detail in the colour plot of Figure 4.28 for a sample temperature of 37 K, low excitation power (around 0.2 mW) and X polarization. The emission intensity of both QRs and the CMX is presented in colour scale as a function of the excitation (vertical scale) and emission (horizontal scale) energies. Three different colour scales have been used (one for each peak) in order to visualize easily the three resonances. The energy of the exciton emission maxima (*s*-state) of the QRs corresponds to the respective *p*-states. A double maximum at the QRs *p*-states is observed in the CMX emission. This is again an evidence of the individual coupling of each QR to the CMX. The PLE profiles of the QRs, corresponding to vertical cuts in Figure 4.28, are shown in Figure 4.29 together with the ones obtained at 7 K. The QR-B PLE spectra (red open circles) display small shoulders at the *p*-state energy of QR-A indicating an enhancement of the QR-B emission upon excitation in QR-A *p*-state. Moreover, the QR-A PLE profiles (black solid circles) show an asymmetry to lower

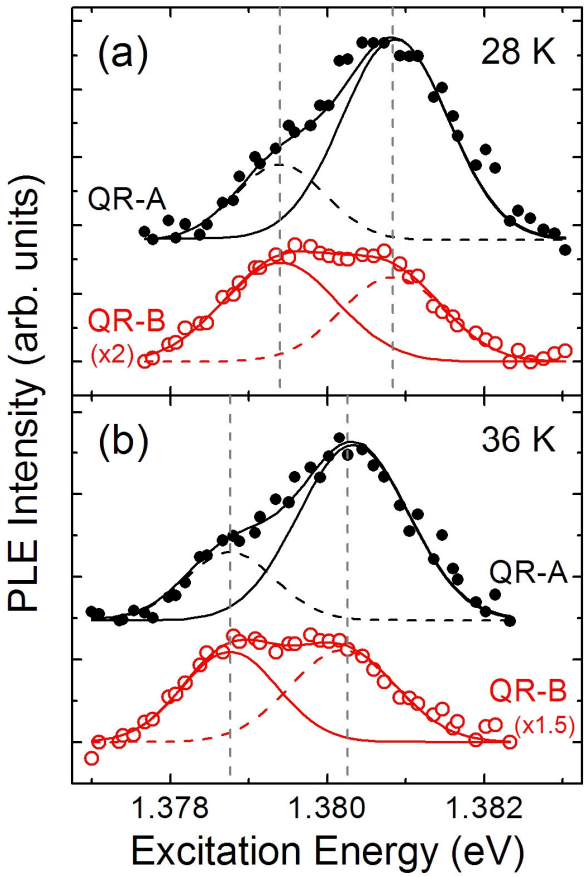


**Figure 4.30.** PLE spectra of QR-A and QR-B for X polarization at (a) 28K and (b) 36K. The excitation intensity was 1.5 mW in both cases. The vertical lines mark the *p*-state energies. Each profile is fitted by two Gaussian curves. The solid (dashed) Gaussian lines correspond to the intra-QR (inter-QR) excitation.

excitation energies which are indicative of the reciprocal process. These are signs of cross-excitation between the two QRs. Although weak, they are systematically observed for all the detunings studied. They become clearer at high excitation intensities. Figure 4.30 shows the PLE spectra of QR-A (black solid circles) and QR-B (red open circles) taken at 1.5 mW for different detunings (28 and 36 K). It can be observed that the shoulders and the asymmetries found at low excitation power have evolved into distinct peaks when the power is increased. All the spectra present a double peak structure, which is well fitted by two Gaussian curves. The main maxima, fitted by the solid lines, correspond to the enhancement of each QR emission upon excitation at its own *p*-state. This will be called *intra-QR* excitation. In addition, new peaks, fitted by dashed lines, appear at the *p*-state energy of the other QR. This is the *inter-QR* excitation. Then, each

QR becomes brighter upon excitation at the *p*-state of the other QR giving clear evidence of the cross-excitation between both QRs.

The cross-excitation is schematically drawn in Figure 4.31 where the involved states and transitions are shown. Black solid arrows represent the excitation (up) and emission (down) processes of QR-A. The one from the CMX state represent the emission of QR-A into a cavity photon. The dashed black arrow indicates the QR-B exciton emission induced by its coupling to QR-A mediated by the cavity. Red curved arrows stand for the reciprocal case. This type of cross-excitation is not possible in independent QDs being separated by 1.4 μm. A rough estimate of the electrostatic dipole interaction for CdSe QDs gives a transfer of energy of 1 meV for an interdot distance of R = 5 nm [79]. Assuming a similar value for our InAs QRs, and considering the $1/R^3$ dependence of the interaction, the direct dipole coupling would be in the range of $10^{-8}$ meV for our specific QRs. Consequently, coupling between the two QRs is only possible through their interaction with the CMX.

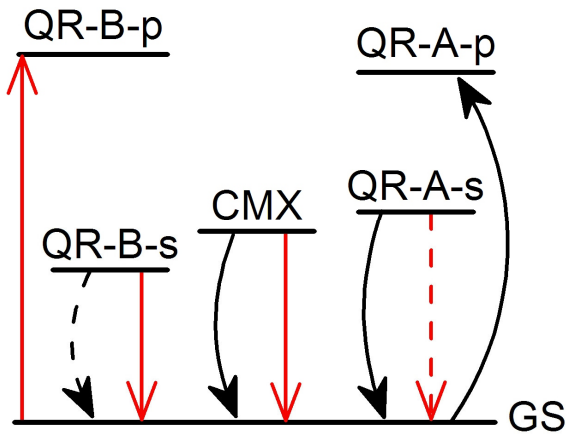


**Figure 4.31.** Schematic diagram of the cross-excitation between the QRs. QR-*s,p* indicate first and second excited states. GS and CMX indicate ground and CMX states. The arrows represent the involved transitions.

The cross-excitation is then demonstrated to depend on the external pumping power. As is shown in Figure 4.32(a), the intra- and inter-QR contributions to the QR-A emission increase for increasing the excitation power. By fitting the spectra with two Gaussian curves, we can extract the excitation intensity evolution shown in Figure 4.32(b) of the intra-QR (red crosses) and inter-QR (blue triangles) contributions to the PLE intensity of QR-A. Both contributions increase and saturate at high excitation power in a similar way. A similar behaviour is observed also in QR-B as it can be observed in Figure 4.33. The sublinear trend observed in the inter-QR excitation

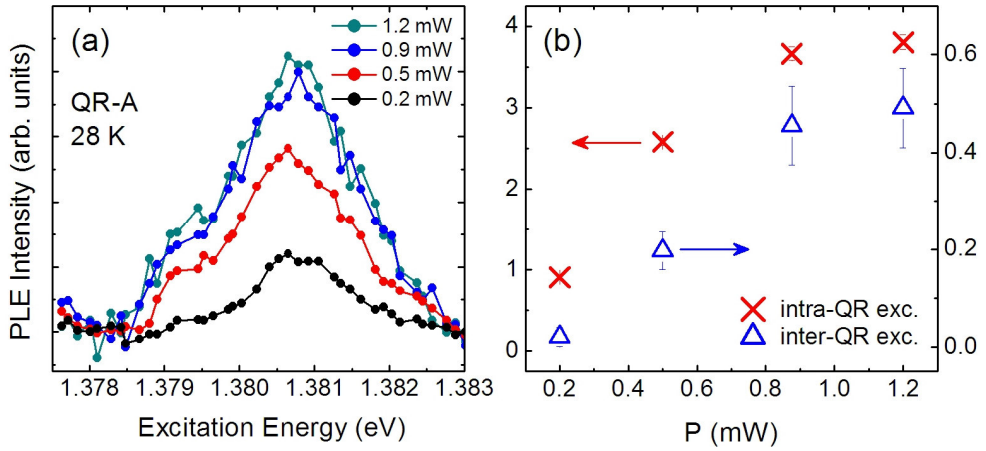


**Figure 4.32.** (a) PLE spectra of QR-A for different excitation powers recorded at X polarization and 28K. (b) PLE intensity, extracted from the fits of PLE spectra in (a), for intra-QR (red crosses) and inter-QR (blue triangles) excitation as a function of the applied power.

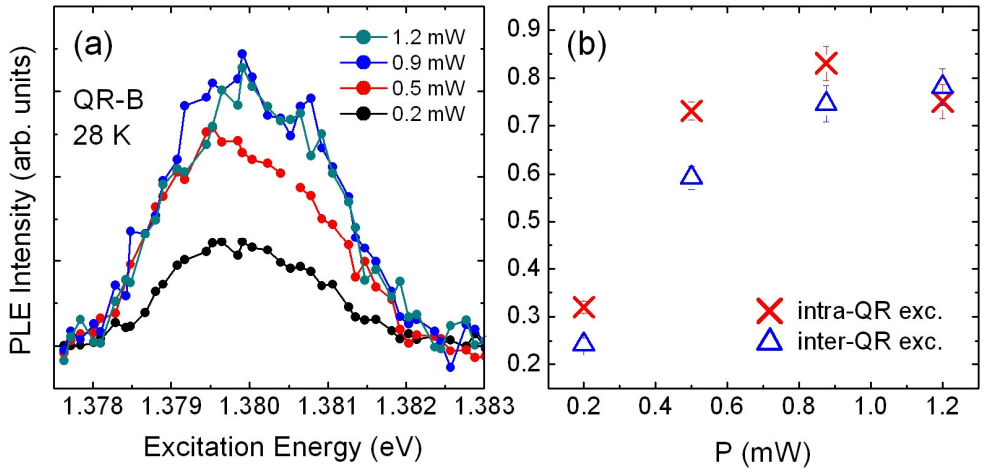


**Figure 4.33.** (a) PLE spectra of QR-B for different excitation powers recorded at X polarization and 28K. (b) PLE intensity, extracted from the fits of PLE spectra in (a), for intra-QR (red crosses) and inter-QR (blue triangles) excitation as a function of the applied power.

processes suggests a coherent coupling of the *s*-states mediated by the cavity mode. The process would occur in the following way: after the resonant excitation of the *p*-state of one QR, the *e-h* pair relaxes incoherently (by phonon emission) to the *s*-state of the same QR and becomes coherently coupled to the other QR by the cavity mode. A second channel leading to an incoherent inter-QR interaction would consist of an

incoherent decay from the *p*-state of the first QR into a cavity photon, exciting then the second QR. Although this second mechanism cannot be completely ruled out, if the inter-QR emission were due to the direct photon injection from the CM, a linear trend would be expected in its intensity as a function of the excitation power due to the fact that the CM emission does not saturate.

We can now evaluate the magnitude $J$ of the effective coupling between the QRs. Using equation (2.29) and the individual coupling strengths $g_i \approx 30$ μeV ($i = A, B$) obtained in Section 4.4.3, together with the typical values for the detunings ($\Delta_i \approx 1$ meV), we obtain $J \approx 2$ μeV. This magnitude is much smaller than $\left|\Delta_A - \Delta_B\right|$ for typical values of the detunings. Therefore, population oscillations between the two qubits are expected to be slow enough to be easily detectable [79].

## 4.6. Summary

InAs/GaAs self-assembled QRs have been demonstrated to be SPE by quantum-correlation measurements under continuous excitation based on a HBT interferometer. The second order auto-correlation functions of the X and XX lines of a single QR show clear antibunching with $g^{(2)}(0)$ values below 0.5. The asymmetric shape of the XX-X cross-correlation measurement indicates sequential emission in the XX-X transition cascade. The characteristic rise times are longer for the X emission than for the XX one for similar emission intensities.

Two additional QRs, with an estimated spatial separation of 1.4 μm and coupled to the same cavity mode, have been investigated. Individual coupling of each QR with the cavity is demonstrated by significant PL intensity increases and a reduction in the lifetime as the detuning is decreased. The estimated values of 30 μeV of the individual coupling strengths by the modification in the SE rate, together with the absence of a measurable energy anticrossing, indicate weak coupling regime in both cases. Different polarization behaviours have been observed in each QR as the detuning is varied. While one QR preserves its linear polarization parallel to the CM one even at large detunings, the other one changes continuously its linear polarization angle from perpendicular, at large detuning, to parallel to the CM one, at zero detuning. Besides, its polarization angle changes its sign for negative detunings, which is qualitatively explained in terms of the QR mixing with cavity states. The intrinsic dipole orientation of the uncoupled QRs and their precise location with respect to the cavity center could play an important role in the polarization dependence on the energy detuning.

Simultaneous coupling of the QRs to the cavity is demonstrated by the observation of Purcell effect in both QRs at the same time, which allows the CM to mediate an effective coupling between them. The inter-QR effective interaction is evidenced by the increase in the emission intensity of each QR upon the resonant excitation at the excited state of the other one. Coherent coupling between the two QRs is believed to be the most probable interaction mechanism due to the similar saturation in both emission processes (intra- and inter-ring excitation) upon increasing the excitation power.

## 4.7. Future work

The results presented in this chapter leave new possibilities to a further investigation that can be carried out in order to have a better understanding of the light-matter interaction in these systems.

Firstly, the presented argument based on the QR and CM state mixing presented in Section 4.4.4 only gives a qualitative explanation of the linear polaritation rotation in QR-B as the detuning is varied. It would predict a rotation also in the CMX polarization, which is not experimentally observed. As was explained, other factors should be taken into account, as the number of photons in the cavity. In this way, the lack of rotation in the CMX emission could be due to a high photon occupation of the cavity mode. With this in mind, then the effective rotation should depend on the excitation intensity. A preliminary result is shown in Figure 4.34, where the polar plots of the QR-B polarization are presented for two different excitation powers at $\Delta$ = 1.55 meV. No

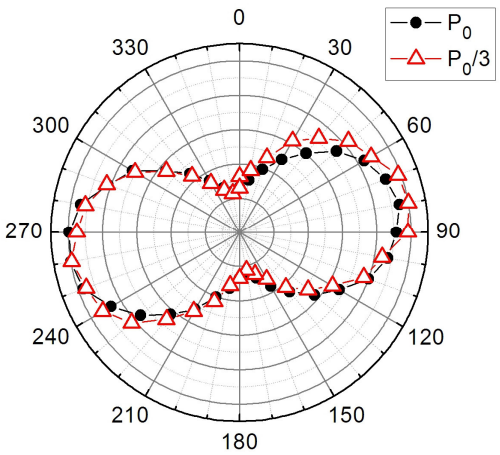


**Figure 4.34.** QR-B polarization polar plots for two different excitation powers ($P_0$ = 300 μW). The detuning was $\Delta$ = 1.55 meV. The data are normalized to unity.

significant difference is observed in the polarization angle which is believed to be due to the large detuning used. A more complete study would be needed at smaller detunings to clarify this point.

On the other hand, the cavity effect on the quantum correlation measurements in the form of a wide bunching peak observed in Section 4.4.5 has not been totally understood yet. Solving the dynamic equations including the CMX state could give a theoretical expression for $g^{(2)}(\tau)$ and a better understanding of the coupling mechanism. Moreover, auto-correlation measurements of the QR-B line selecting its polarization axis as a function of the detuning would allow assessing the SPE character of QR-B over a continuous range of polarization angles.

Another effect that deserves further investigation is related to the cross-excitation between QR-A and QR-B. The power dependence of the inter-QR PLE intensity would be expected to depend on the detunings of both QRs in a similar way as the power dependence of the *s*-state of QR-A, that was shown in Section 4.4.2 to increase the slope of its trend as the detuning was decreased (Figure 4.15).

# Chapter 5

# Optical and Structural Properties of InN Nanocolumns

Nanotechnology based on group-III nitride nanocolumns (NCs) points to a new generation of devices benefiting from quantum confinement effects, large surface to volume ratios and broad emission range [121]. Among group-III nitrides, the InN fundamental parameters are the poorest known due to the difficulties to grow high quality InN layers (mainly due to the low dissociation temperature of InN) [32-34]. Structural defects and strain usually found in InN epilayers are minimized to a great extent in InN NCs [33] due to the lateral elastic relaxation, which admits greater lattice mismatch without the formation of defects. Therefore, NCs constitute perfect candidates for studying InN fundamental properties. One of the most intriguing is the presence of an electron accumulation layer (EAL) at the surface, which leads to a strong surface conductivity that could prevent the development of electronic devices requiring doping control. Thus, the knowledge of the EAL origin and possible mechanisms to control it constitutes an important issue in the InN research. Moreover, the possibility of growing high quality InN NCs in different crystallographic directions favours the study of InN properties in different polar and non-polar surfaces.

This chapter presents an investigation, by inelastic light scattering, of the structural and vibrational properties of InN NCs grown on different substrates and with different orientations. Special attention has been paid to the LO phonon-plasmon coupling at the surface EAL, whose microscopic origin has been studied by HR-TEM. The chapter is organized as follows: Section 5.1 presents a description of the samples including growth and structural details. Results of inelastic light scattering and HR-TEM in InN NCs grown on silicon substrates are given in Section 5.2, focusing on the LO phonon-plasmon coupled mode and the surface EAL. Section 5.3 shows a study of Raman scattering in InN NCs grown on *a*-plane GaN templates. Finally, a summary and proposals for future work are given in Sections 5.4 and 5.5 respectively.

# 5.1. Sample description

## 5.1.1. Growth details

The growth of the InN samples studied in this chapter was performed by Dr. J. Grandal at *Instituto de Sistemas Optoelectrónicos y Microelectrónica* (*ISOM*) from *Universidad Politécnica de Madrid*. Different InN columnar layers were grown by plasma-assisted MBE using a radio frequency plasma source to activate the nitrogen and a standard *Knudsen* effusion cell for In. Details about the MBE system can be found in [37, 126]. N-rich conditions were established to achieve the columnar morphology, as explained in Section 2.2.5. The InN NCs were grown on different substrates: Si(111), Si(001) and GaN $(11\bar{2}0)$ templates deposited on *r*-plane sapphire. In some cases, AlN buffer layers or few monolayers of metallic Al were used to improve the crystal quality.

Table 5.1 summarizes the growth characteristics of the InN samples investigated in this chapter. The substrate temperature, the most critical parameter (see Section 2.2.5), was varied in the range of 460 – 480 ºC for samples grown on silicon (m1051, m1397, m1414 and m1419) and was set at 525 ºC for *a*-plane GaN templates (R558 and R563).

| Sample | Substrate | $T_{subs}$ (ºC) | Average diameter (nm) | Average NC height/layer thickness (µm) | Buffer layer | Morphology |
|---|---|---|---|---|---|---|
| m1051 | Si(111) | 475 | 125 | 1.60 | AlN | columnar |
| m1397 | Si(001) | 480 | 140 | 1.30 | Al (30 sec) | columnar |
| m1414 | Si(001) | 460 | 70 | 0.5-0.85 | - | columnar |
| m1419 | Si(001) | 465 | 65 | 0.75 | Al (30 sec) | columnar |
| m1345 | Si(111) | 465 | 50 | 1.20 | - | columnar |
| m1346 | Si(111) | 465 | 60 | 1.20 | - | columnar |
| m1347 | Si(111) | 465 | 80 | 1.20 | - | columnar |
| m1373 | Si(111) | 465 | 110 | 1.20 | Al (30 sec) | columnar |
| m1374 | Si(111) | 465 | 135 | 1.20 | Al (30 sec) | columnar |
| m1157 | Si(111) | 465 | - | 0.80 | AlN | compact |
| R558 | $Al_2O_3$ (1-102) | 525 | 200 | 1.00 | GaN (11-20) | columnar |
| R563 | $Al_2O_3$ (1-102) | 525 | 200 | 1.00 | GaN (11-20) | columnar |

**Table 5.1.** Growth characteristics of the InN samples studied in this chapter.

A group of 5 samples (m1345, m1346, m1347, m1373 and m1374) were grown on silicon substrates at fixed substrate temperature (465ºC) and different nitrogen flux, leading to InN NCs with different average diameters. A compact InN sample (m1157) was also used as reference.

### 5.1.2. Structural characterization

The structural characterization of the samples was carried out by scanning (SEM) and transmission (TEM) electron microscopy. Both techniques give information about the morphology of the samples (NC density, average diameter, shape, etc.). TEM also provides details about the crystalline orientation, quality and strain. The SEM images presented in this section were obtained by Dr. J. Grandal with a JOEL JSM-5800 microscope belonging to *ISOM* while the TEM ones were performed by Dr. E. Luna and Dr. A. Trampert at the *Paul-Drude Institut für Festkörperelektronik* (PDI) in Berlin, with a JEOL JEM 3010 microscope operating at 300 kV. The cross-sectional specimens for TEM characterization were prepared by standard methods of mechanical grinding, dimpling and Ar-ion beam milling (see Section 3.7.2).

**InN nanocolumns grown on silicon substrates**

Figure 5.1 shows SEM images of the samples m1051 and m1419 revealing the nanocolumnar morphology of the InN layers grown on Si(111) and Si(001) substrates respectively. The isolated InN NCs display some dispersion in height and diameter. The hexagonal cross-section of the NCs can be clearly observed in the SEM image of m1419 (Figure 5.1(b)).

Figure 5.2 presents X-TEM images of sample m1051 showing again the columnar morphology. The HR-TEM micrograph in Figure 5.3(a) shows NCs as hexagonal single crystals with the growth direction along the [0001] axis. A flat interface, marked by the yellow arrow, can be observed between InN and AlN layers. The corresponding selected area electron diffraction (SAED) pattern is shown in Figure 5.3(b). Three patterns are observed: green, yellow and red marked spots refer to Si, InN and AlN reciprocal lattices respectively. This image confirms the wurtzite structure and a perfect epitaxial alignment of the InN NCs with the AlN buffer layer, as well as the lack of strain in both materials. However, InN NCs grown on Si(001) substrates (not shown) present an epitaxial misalignment with the substrate but again with the preferential growth direction along [0001] axis.

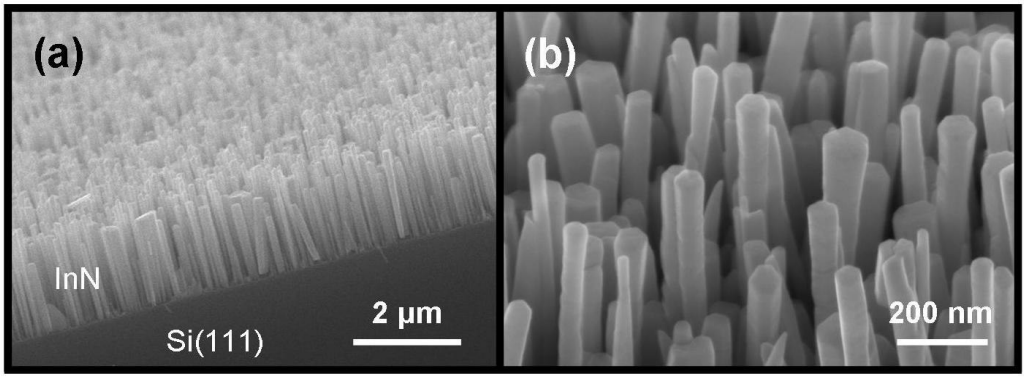


**Figure 5.1.** SEM images of InN NC samples grown on Si substrates: (a) m1051 and (b) m1419.

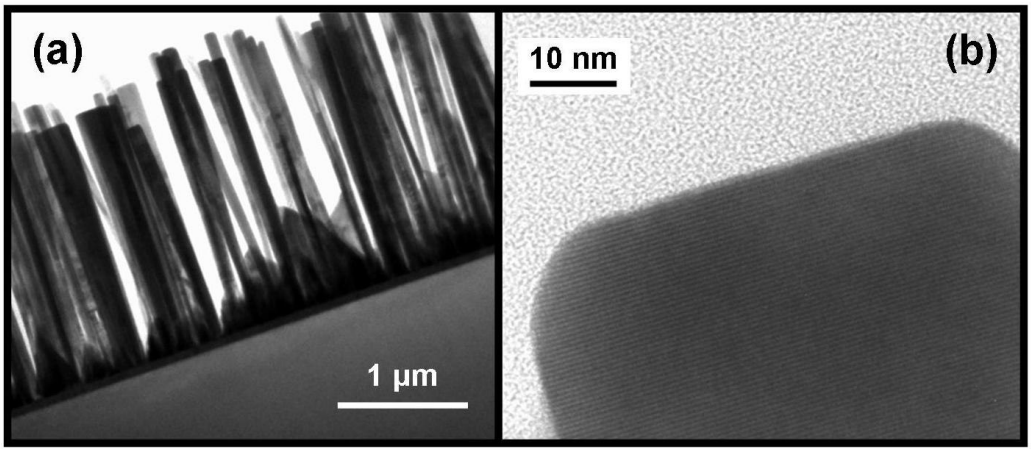


**Figure 5.2.** Cross-sectional TEM images of sample m1051.

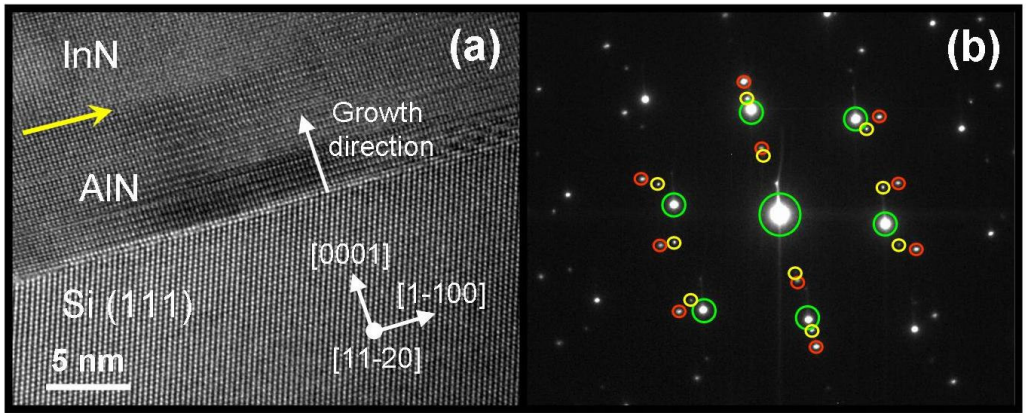


**Figure 5.3.** (a) Cross sectional HR-TEM image and (b) SAED pattern of sample m1051. In (b), green, yellow and red circles refer to Si, InN and AlN spot patterns respectively.

**InN nanocolumns grown on *a*-plane GaN template**

The SEM images in Figure 5.4 display the morphology of InN NCs grown on *a*-plane GaN templates. The columns show clear side facets and even inclined facets at the top, in contrast to *c*-plane oriented NCs with flat end (see Figure 5.2(b)). Assuming the rectangular geometry of the *a*-plane base (see inset of Figure 5.4(b)), the sidewalls are formed by *c*- and *m*-planes ($(0001)$ and $(1\bar{1}00)$ respectively). This kind of morphology has been already observed in AlGaN and InN nanorods grown on *r*-plane sapphire substrates by metal-organic vapor phase epitaxy (MOVPE) [173-175].

The crystalline structure of these NCs is again investigated by TEM. The X-TEM image in the inset of Figure 5.5(a) demonstrates that no compact InN epilayer is formed between the GaN template and the NCs. The HR-TEM image taken along the $[1\bar{1}01]$ axis (perpendicular to the growth direction $[11\bar{2}0]$) and the corresponding SAED pattern are shown in Figure 5.5 (a) and (b) respectively. The interface between the InN and GaN structures is marked by the yellow arrow in Figure 5.5(a). The superposition of two spot patterns is observed in Figure 5.5(b), one from InN (yellow squares) and the other from GaN (red circles). Then, the NCs have wurtzite structure with the same orientation of the GaN template. The estimated lattice parameter reveals that the InN NCs are almost fully relaxed, as occurred in the case of InN NCs grown on silicon substrates.

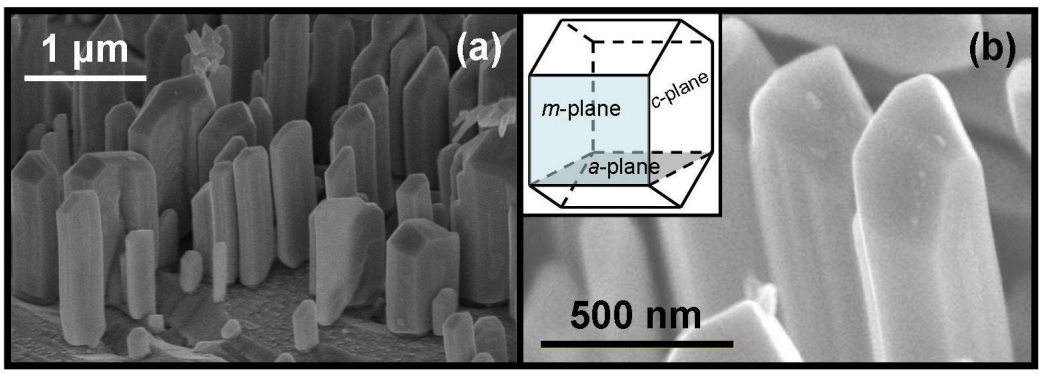


**Figure 5.4.** (a) SEM image of *a*-plane InN NCs (sample R558). (b) SEM image of sample R558 showing facets at the top. Inset: *a*-plane base rectangular geometry.

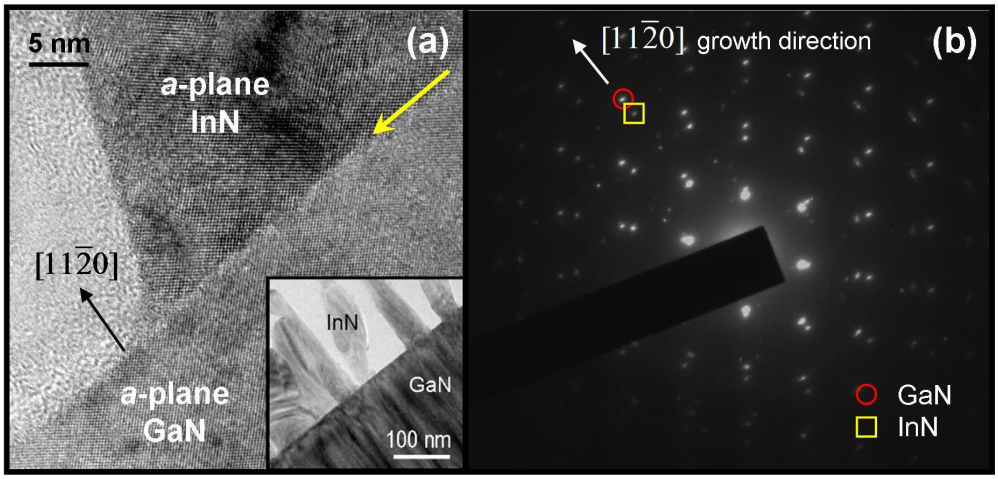


**Figure 5.5.** (a) Cross-sectional HR-TEM image of sample R558. Inset: a lower magnification X-TEM image. (b) SAED pattern of the image in (a). Red circles and yellow squares refer to GaN and InN spot patterns respectively.

## 5.2. Raman scattering in InN nanocolumns grown on silicon substrates

Optical and structural properties of hexagonal InN NCs grown on silicon substrates have been analyzed also by Raman spectroscopy. All the Raman measurements presented in this section were taken at room temperature with the macro-setup configuration described in Section 3.6.1 with a single spectrometer. He-Ne and $Ar^+$-lasers were used as excitation sources. A new sample preparation for *plan-view* (PV) TEM investigation of NCs was performed at the *Paul-Drude Institut für Festkörperelektronik* (PDI) in Berlin in collaboration with the group of Dr. A. Trampert. The TEM images were taken also at PDI with a JEOL JEM 3010 microscope operating at 300 kV.

The RT macro-Raman spectra of a compact InN layer and two NC samples grown on either Si(111) and Si(001) substrates are shown in Figure 5.6. The spectra were recorded at backscattering configuration along the growth direction (*c*-axis) and with a laser wavelength of 632 nm.

All the spectra show a narrow non-polar $E_2$ mode (4 and 5 $cm^{-1}$ width for NCs grown on Si(111) and Si(001) respectively) at essentially the same frequency (491 $cm^{-1}$), indicating total strain relaxation and high crystalline quality. The compact sample displays the allowed $A_1$(LO) phonon at 589 $cm^{-1}$ while the NC samples show the LO phonon with $E_1$ symmetry (599 $cm^{-1}$). As was explained in Section 2.2.5, this is the

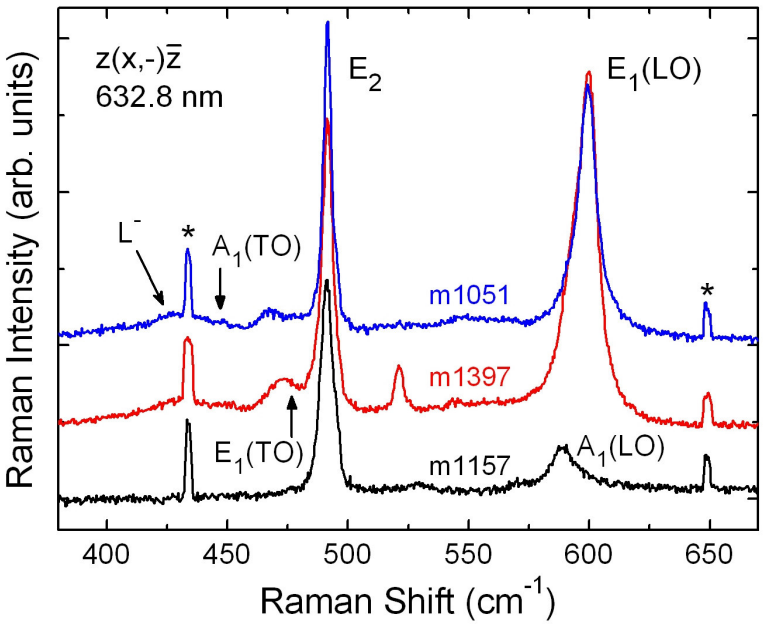


**Figure 5.6.** RT Raman spectra of a compact InN layer (sample m1157) and two NC samples grown on Si(001) (m1397) and Si(111) (m1051) for $z(x,-)\bar{z}$ nominal scattering configuration. Ne spectral lines are marked with asterisks.

result of the light refraction and elastic scattering due to the surface roughness of the NCs ensemble. This effect is schematically depicted in Figure 5.7(a). Each NC scatters the light in different directions which, together with the high refraction index of InN, results in light propagation inside the NCs perpendicular to the *c*-axis. Then, the *"real"* scattering configuration differs from the nominal one. These configurations are shown in Figure 5.7(b) together with the allowed modes in each case. *x*- and *y*-directions are equivalent for these NCs. The $E_1$(LO) phonon is included in the list because an important Fröhlich contribution to the Raman intensity is expected for the InN NCs, as was already mentioned in Section 3.5.3. The Fröhlich Raman tensors depend on the phonon propagation direction $\vec{q}$. The corresponding Raman tensors for "forbidden" scattering by the polar $E_1$ phonon in wurtzite crystals are shown in Table 5.2 for phonon propagation parallel and perpendicular to the *c*-axis [149]. When $\vec{q}$ is parallel to *x*- or *y*-direction the $E_1$(LO) phonon arises from the diagonal elements.

A contribution to the $A_1$(LO) phonon intensity would be expected from the light entering the NCs along the *c*-axis. However, this contribution is not observed probably due to the small upper surface of the NCs compared with their lateral sidewalls.

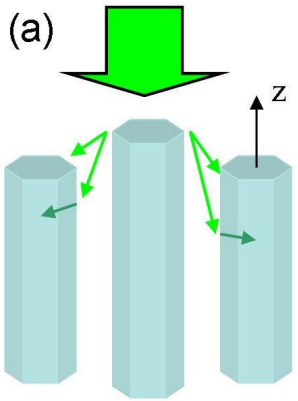


(b)

| nominal configuration | "real" configuration | allowed modes |
|---|---|---|

$$z(x,x)\bar{z} \rightarrow \begin{cases} x(z,z)\bar{x} \rightarrow A_1(TO), E_1(LO) \\ y(x,x)\bar{y} \rightarrow A_1(TO), E_2 \end{cases}$$

$$z(x,y)\bar{z} \rightarrow \begin{cases} x(z,y)\bar{x} \rightarrow E_1(TO) \\ y(x,z)\bar{y} \rightarrow E_1(TO) \end{cases}$$

**Figure 5.7.** (a) Scheme of the light propagation inside the hexagonal NCs when the sample is illuminated along the *c*-axis. (b) Nominal and "real" scattering configurations and allowed vibrational modes in each case.

| $E_1(x)$ | $E_1(y)$ |
|---|---|
| $\begin{pmatrix} a' & 0 & 0 \\ 0 & a' & 0 \\ 0 & 0 & b' \end{pmatrix}$ | $\begin{pmatrix} 0 & d' & 0 \\ d' & 0 & 0 \\ 0 & 0 & 0 \end{pmatrix}$ |

**Table 5.2.** Raman tensors for forbidden scattering by the polar $E_1$ phonon in wurtzite.

Finally, the feature appearing near 468 $cm^{-1}$ in the NC samples in Figure 5.6 is absent for 514.5 nm excitation (not shown). As the InN band structure has no critical points in this energy range, this feature is attributed to an extrinsic effect.

### 5.2.1. LO phonon-plasmon coupling

The weak and broad peak observed around 430 $cm^{-1}$ in Figure 5.6 is attributed to the lower branch of the LO phonon-plasmon coupled mode, marked by $L^-$ (see Section 2.2.4), confirming the presence of an EAL at the lateral non-polar surfaces of the NCs. In this way, the uncoupled $E_1$(LO) phonon comes from the inner part of the NCs while the coupled $L^-$ mode arises from their lateral surfaces [129, 130]. The observed $L^-$ peak cannot be attributed to the $A_1$(TO) phonon. The dispersion of $A_1$(TO) phonon away from the BZ center is positive in wurtzite, then any scattering event without wavevector conservation would result in a peak at higher frequency than the Γ-point value (marked at 447 $cm^{-1}$ in Figure 5.6). The $L^-$ peak is not observed in the compact layer probably due to its lower specific surface.

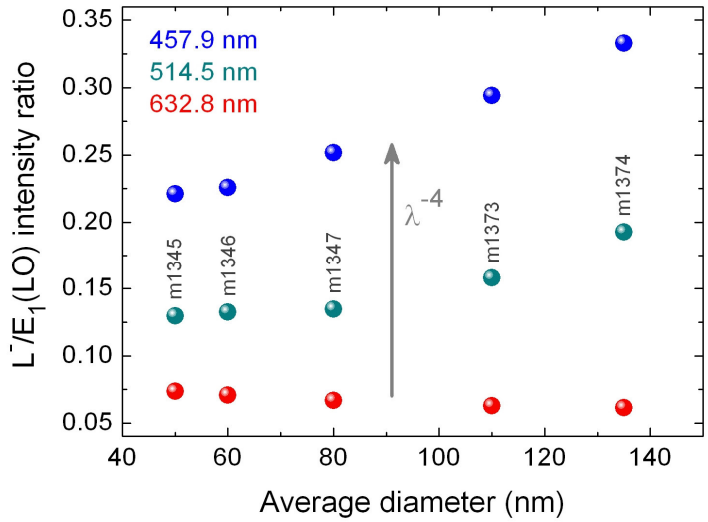


**Figure 5.8.** $L^{-}/E_1$(LO) intensity ratio as a function of the average diameter of InN NCs grown on Si(111) for 457.9 nm (blue), 514.5 nm (green) and 632.8 nm (red) excitation wavelengths.

The $L^{-}$ to $E_1$(LO) intensity ratio has been investigated for the sample set grown at fixed temperature but with different average NC diameter (m1345, m1346, m1347, m1373 and m1374). The $L^{-}/E_1$(LO) intensity ratio is plotted as a function of the average NC diameter in Figure 5.8 for different excitation wavelengths.

The general increase observed for decreasing the excitation wavelength (from 632.8 to 457.9 nm) is mainly due to light scattering by the NC [129]. Indeed, the $L^{-}/E_1$(LO) intensity ratio represented as a function of the excitation energy for all the samples in Figure 5.9 follows the $\lambda^{-4}$ trend of the scattering cross section [136] normalized to the highest energy (grey triangles).

Coming back to Figure 5.8, different trends are observed in the $L^{-}/E_1$(LO) intensity ratio as a function of NC diameter by changing the exciting wavelength. While for largest excitation wavelength (632.8 nm) this ratio decreases as the NC diameter increases, the opposite dependence is observed at shorter excitation wavelengths (514.5 and 457.9 nm). This difference can be qualitatively explained considering the competition of two effects: 1) the elastic light scattering, which according to Figure 5.7(a), enhances the lateral surface contribution to the Raman intensity and 2) the surface to volume ratio contribution.

Considering the presence of a surface EAL of fixed width and the fact that $L^{-}$ and $E_1$(LO) arise from the surface and the inner parts of the NCs respectively, the $L^{-}/E_1$(LO) intensity ratio should depend on the average NC diameter as the surface to volume ratio given by:

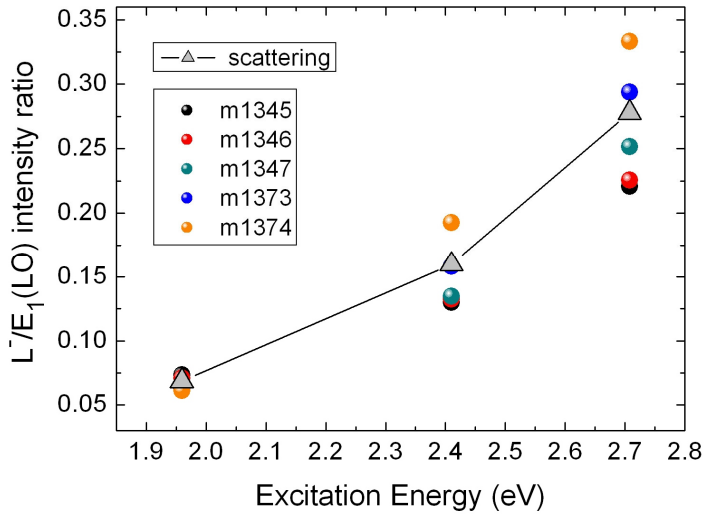


**Figure 5.9.** $L^{-}/E_1$(LO) intensity ratio as a function of the excitation energy (colour circles) for the NC samples with different average NC diameters. The fourth power of the excitation energy normalized to the highest energy (2.71 eV) is shown by the grey triangles.

$$\frac{S}{V}(r) = \frac{L\left(\pi r^2 - \pi(r-d)^2\right)}{L\pi(r-d)^2} = \frac{d(2r-d)}{(r-d)^2} \tag{5.1}$$

where $d$ and $r$ are the EAL width and the NC radius respectively. $L$ is the NC height. This ratio decreases as the NC diameter increases for fixed $d$. This is the trend observed for 632.8 nm excitation in Figure 5.8. However, it is masked by the enhanced scattering for higher excitation energies (514.5 and 457.9 nm). This indicates that a more accurate description of the scattering cross section as a function of the scattering parameter $r / \lambda$ is required to account for the trends observed in Figure 5.8. Indeed, the light wavelength inside the NCs is comparable to the NC diameter (the InN refraction index is 2.9), thus small variations in $r / \lambda$ result in strong changes in the scattering cross-section, as results from the Mie´s theory [176].

### 5.2.2. Microscopic structure of the EAL

In order to investigate the origin of the surface EAL at the lateral sidewalls of the NCs, the crystalline structure near the surface has been studied in detail by HR-TEM. The PV-TEM preparation method described in Section 3.7.2 was carried out for this purpose.

The first important result is the possibility of determining the cross-sectional shape of the NCs. Figure 5.10 shows a PV-TEM micrograph of InN NCs grown on Si(111),

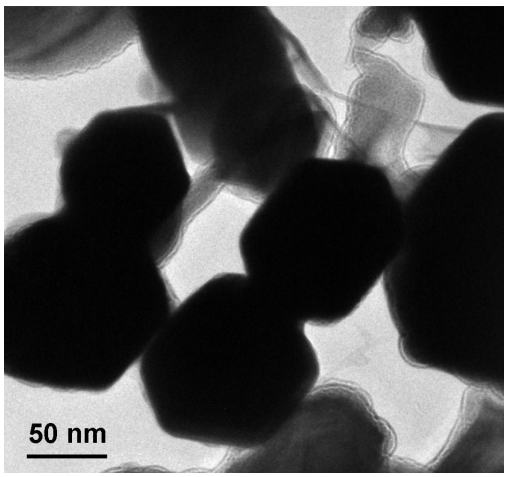


**Figure 5.10.** PV-TEM image of an InN NC sample grown on Si(111) (m1051).

where the hexagonal cross-section can be observed. The images also give the average diameter and the density of NCs.

The detailed analysis of the NCs surface does not show clearly defined lateral facets. In fact, PV-HR-TEM images shown in Figure 5.11 reveal a central InN core surrounded by a thin (2-3 nm) disordered shell. The interface between this shell and the InN core (marked by the yellow arrow in Figure 5.11) is rather sharp, suggesting that the facets of the InN core material are well defined. In order to discard the sample preparation method as the origin of the surrounding shell, the same procedure was carried out in a GaN NC sample. In contrast to InN NCs, GaN NCs exhibit sharp surfaces without a surrounding shell (Figure 5.12). The lateral surface roughness of InN NCs can also be appreciated when the images are taken perpendicularly to the growth direction. Figure 5.13 shows an InN NC that was removed from its substrate by scratching the sample surface. Once more a rough shell (in a range of a few nanometers) around the NCs core is observed

The analysis of the corresponding SAED patterns points at $In_2O_3$ as the composition of the surrounding shell of the InN NC. This is in agreement with recent publications reporting on the aging properties of InN and the formation of a native indium oxide layer [177]. In this way, the shell would form by natural oxidation of the NCs exposed to the ambient atmosphere after growth. This oxidation occurs in polar and non-polar InN surfaces, as shown in the following section, where the EAL is manipulated by external treatments.

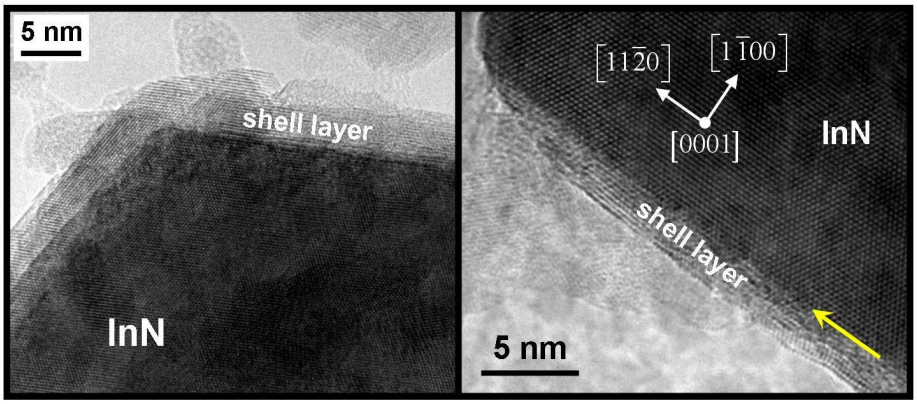


**Figure 5.11.** PV-HR-TEM images of InN NCs grown on Si(001) (sample m1414).

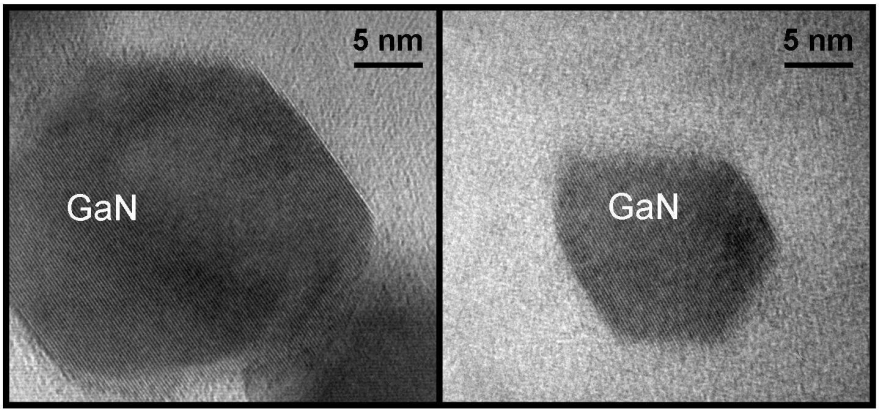


**Figure 5.12.** PV-HR-TEM images of a GaN NC sample prepared as the InN NC samples.

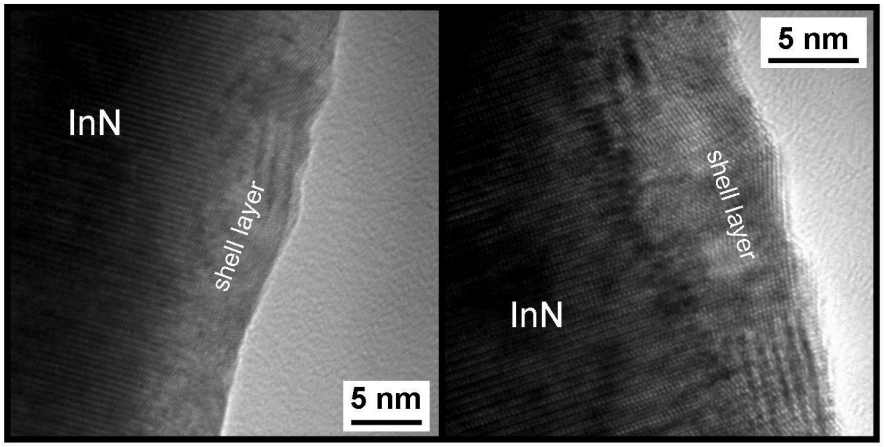


**Figure 5.13.** X-HR-TEM images of InN NCs removed from the substrate (sample m1419).

### 5.2.3. Response of the EAL to chemical treatments

The charge accumulation in InN surfaces is an undesirable effect for electronic device applications. Therefore, the development of methods for removing the EAL, or at least controlling it, constitutes an important challenge.

InN NCs are sensitive to the exposure to certain chemical compounds. This is reflected by a frequency shift of the $L^-$ coupled mode. Figure 5.14(a) shows the variation of the electron concentration at the lateral surfaces of the InN NCs (calculated from the $L^-$ frequency by equations (2.34) and (2.35)) upon immersion in hydrochloric acid (HCl). The immersion provokes an increase in the electron concentration which tends to saturate for large etching times. Figure 5.14(b) presents the electron concentration evolution with time after dipping the sample for 1 minute in HCl and letting it dry in air. After dipping, the electron concentration is found to decrease progressively with increasing time reaching a final equilibrium value (marked by the dashed line) which is higher than the initial electron density of $2.68 \times 10^{18}$ $cm^{-3}$. It is important to notice the different time scales in panel (a) (seconds) and (b) (hours) of Figure 5.14.

The small and partially reversible effect of HCl on the InN NCs can be explained considering the $In_2O_3$ surrounding shell. It has been recently reported that $In_2O_3$ shows a downward bending of the conduction and valence bands at the surface due to the shift of the branch-point into the CB, as in InN [101]. The calculated $In_2O_3$ band bending and

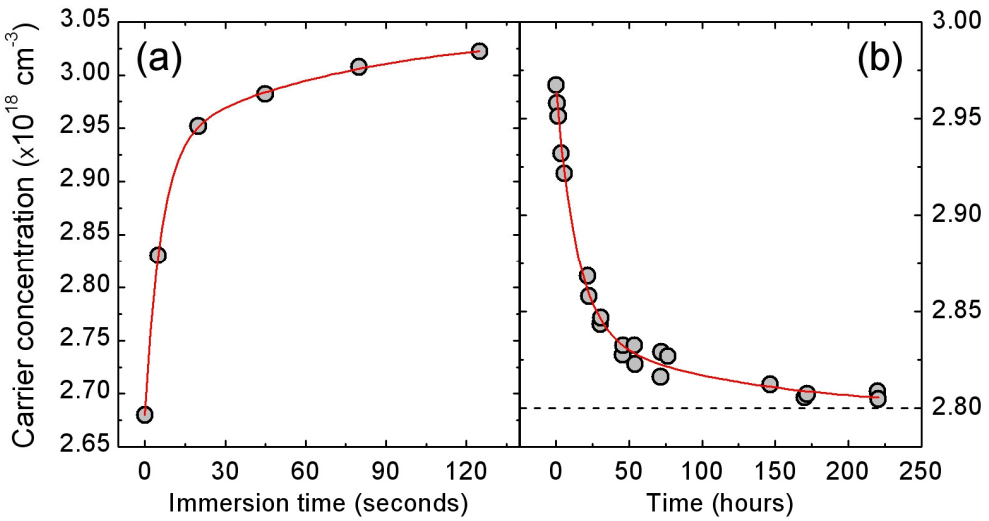


**Figure 5.14.** (a) Electron concentration of an InN NC sample (m1051) as a function of the immersion time in HCl. (b) Temporal evolution of the electron concentration after 1 minute immersion in HCl. The red solid lines are guides to the eye.

carrier concentration profiles are shown in Figure 5.15(a) and (b) as a function of depth below the surface. The CBM at the surface is around 0.4 eV below the branch-point energy in $In_2O_3$. However, for InN this value is larger (around 0.9 eV, see Figure 2.20(a)). As a consequence, an InN surface that is oxidized presents a reduction in the initial surface band bending caused by the passivation of the surface donors [178, 179]. This results in a decrease of the electron density of the accumulation layer and of the electron confinement near the surface, as shown in Figure 5.15(c) [178]. With this in mind, a chemical treatment that eliminates the oxide shell of the InN surface should result in an increase in the electron density at the surface. This is what occurs when the InN NCs are dip in HCl (Figure 5.14(a)). In this way, the electron concentration at saturation (~ $3.04 \times 10^{18}$ $cm^{-3}$) would correspond to clean InN NCs. After taking the NCs out of the HCl bath, the electron concentration decays as the liquid evaporates and the InN surface oxidizes again (Figure 5.14(b)). The initial value of the electron density before the chemical treatment ($2.68 \times 10^{18}$ $cm^{-3}$) is expected to be reached after longer time.

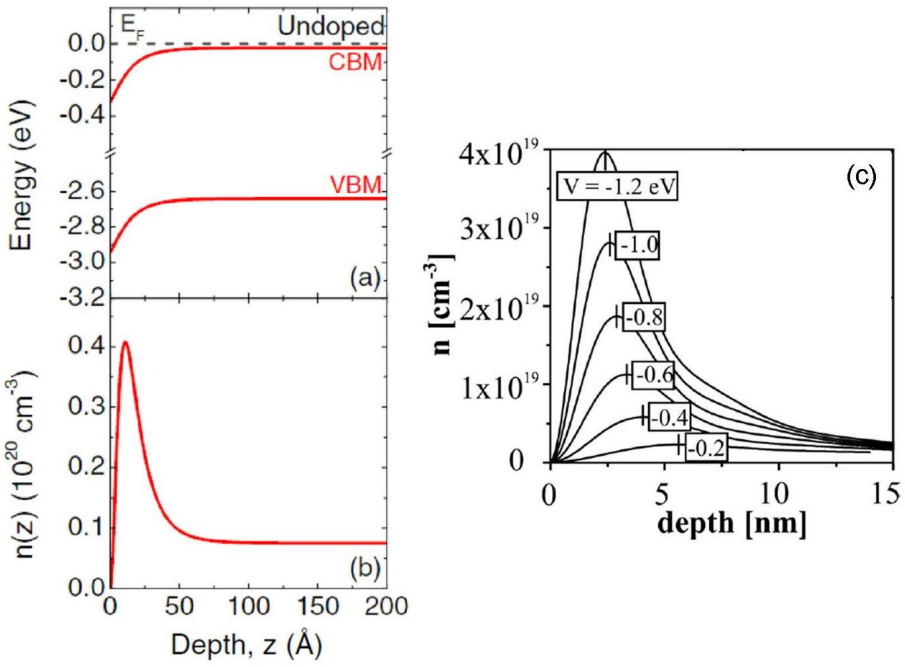


**Figure 5.15.** (a) CBM and VBM with respect to the Fermi level ($E_F$) and (b) carrier concentration profile in the near surface region of $In_2O_3$ [101]. (c) Variation of the carrier concentration profile while decreasing the surface band bending V [178].

## 5.3. Raman scattering in *a*-plane InN NCs

A Raman spectroscopy study has been carried out in the InN NCs grown on *a*-plane GaN templates. It confirms their wurtzite structure and orientation given by TEM images, as well as that the light scattering occurs mainly from the lateral surfaces of the NCs even when the illumination is parallel to their growth direction [129, 130].

All the Raman measurements presented in this section were taken at RT with the macro-setup configuration and using an $Ar^+$-laser (514.5 nm) and a double spectrometer as excitation source and dispersive element respectively.

Figure 5.16 shows the RT macro-Raman spectrum of the *a*-plane InN NCs in backscattering configuration along the growth direction. For comparison, the Raman spectrum of a NC sample grown on Si(111) is also shown. The nominal scattering configurations and polarization are shown in the insets. In both cases, the *z*-direction is chosen parallel to the *c*-axis. All Raman peaks, from NCs and substrate, have been identified. The InN and GaN modes are marked by red and blue labels respectively. The grey arrows indicate phonons of the sapphire substrate. The phonon frequencies have

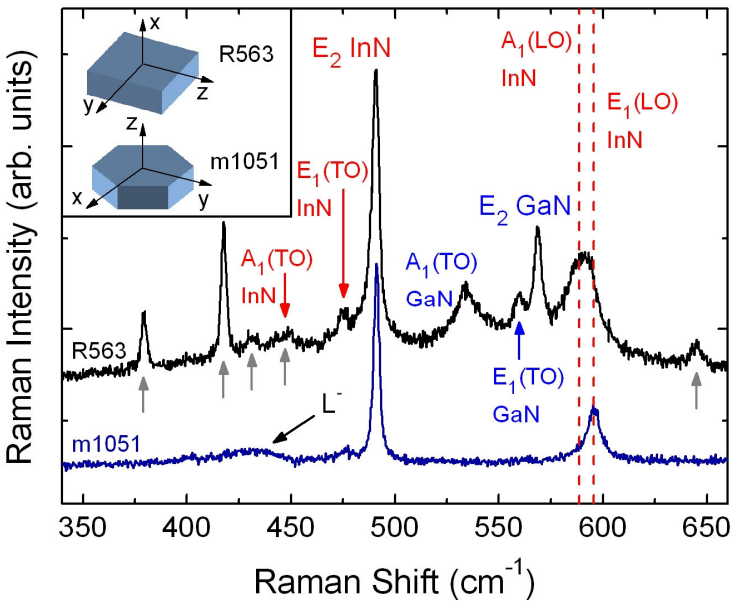


**Figure 5.16.** RT Raman spectra of InN NCs grown on Si(111) (sample m1051) and *a*-plane GaN (sample R563) in backscattering configuration along the growth directions. InN and GaN modes are marked by red and blue labels respectively. The grey arrows indicate the frequencies of the sapphire Raman modes. Inset: scattering directions relative to the crystal structures.

been carefully determined using Ne spectral lines for calibration. Table 5.3 contains the experimental frequencies found for all the phonons, which agree with other reported values [109, 113, 180, 181].

Raman spectra for parallel polarization configurations ( $x(y,y)\bar{x}$ and $x(z,z)\bar{x}$ ) are shown in Figure 5.17 for one of the *a*-plane InN NCs samples. Again the different directions are given in the inset. The *y*- and *z*-directions in the sample were determined by angle-resolved Raman measurements as will be shown later. The GaN template shows the allowed $E_2$ and $A_1$(TO) modes for $x(y,y)\bar{x}$ and the $A_1$(TO) for $x(z,z)\bar{x}$ (see Table 3.4). The difference in the $A_1$(TO) phonon intensities indicates $a > b$ in the Raman tensor (Table 3.3). In $x(z,z)\bar{x}$ configuration, small peaks appear at the GaN $E_1$(TO) and $E_2$ frequencies which are probably due to deviations of the light propagation from the main crystallographic axes. Sapphire modes are marked by grey arrows.

| | $A_1$(TO) | $E_1$(TO) | $E_2$ | $A_1$(LO) | $E_1$(LO) |
|---|---|---|---|---|---|
| InN modes | 447 | 476 | 491 | 589 | 596 |
| GaN modes | 533 | 559 | 568 | - | - |

**Table 5.3.** Experimental frequencies ($cm^{-1}$) of InN and GaN phonons.

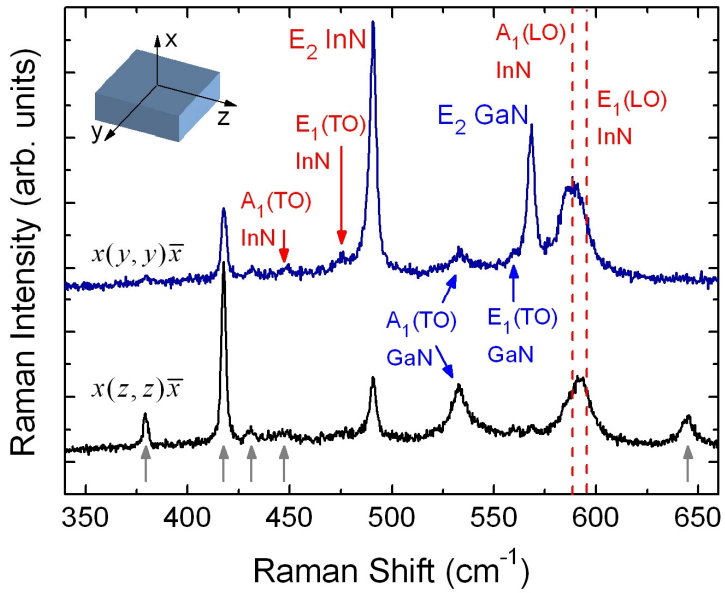


**Figure 5.17.** RT Raman spectra of *a*-plane InN NCs (sample R558) for nominal scattering configurations $x(y,y)\bar{x}$ and $x(z,z)\bar{x}$. InN and GaN modes are marked by red and blue labels respectively. The grey arrows indicate the frequencies of the sapphire Raman modes. Inset: scattering directions relative to the crystal structure.

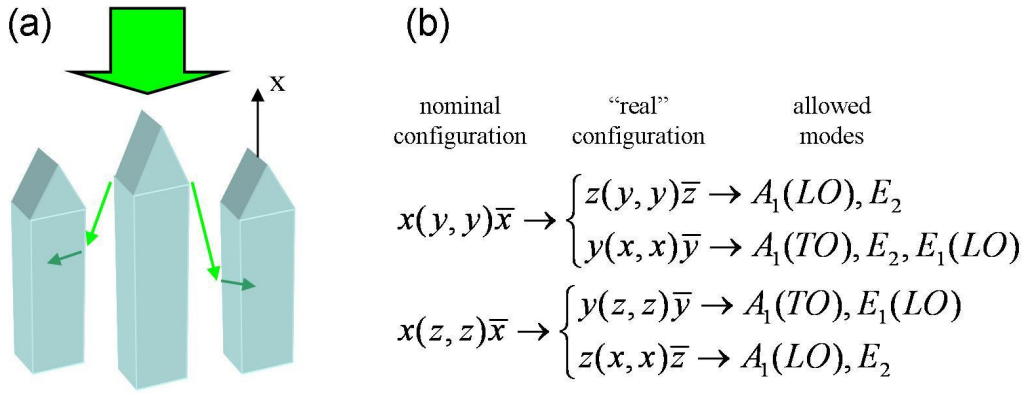


**Figure 5.18.** (a) Scheme of the light propagation inside the *a*-plane NCs when the sample is illuminated along the *x*-axis. (b) Nominal and "real" scattering configurations and allowed vibrational modes in each case.

The situation is different for InN phonons. First, the $E_2$ mode is observed in both configurations, as well as $A_1$(TO). Moreover, a broad peak appear in region of the $A_1$(LO) and $E_1$(LO) phonon frequencies. The appearance of these InN modes in the Raman spectra can be explained again by the fact that most of the light enters through and scatters from the lateral surfaces of the NCs. This situation is schematically depicted in Figure 5.18(a). The nominal and the corresponding *"real"* (considering light propagation inside the NCs strictly perpendicular to their growth direction) scattering configurations together with the allowed phonons in each case are shown in Figure 5.18(b). Again, the $E_1$(LO) phonon is included in the list due to the Fröhlich interaction. In this way, the appearance of all the mentioned InN modes can be justified.

In the case of the mode at $A_1$(LO)-$E_1$(LO) frequencies, the effect of the angular dispersion of the polar Raman modes (see Section 2.2.3) has to be taken into account. This effect occurs when the polar phonon does not propagate exactly along the main crystal axes, as probably happens in the NC system. Then, the experimental peak is a combination of pure $A_1$(LO) and $E_1$(LO) phonons, whose frequency will be given by the upper expression in equation (2.32).

Finally, small features at the forbidden InN $E_1$(TO) frequency can also be appreciated in Figure 5.17 and their appearance is attributed again to light propagation along directions different from the main crystallographic axes.

The presence of the EAL at the lateral sidewalls of these *a*-plane InN NCs cannot be assessed because the observation of a possible LO phonon-plasmon coupled mode ($L^-$) would be hidden by the sapphire modes in the same spectral region (see Figures 5.16 and 5.17).

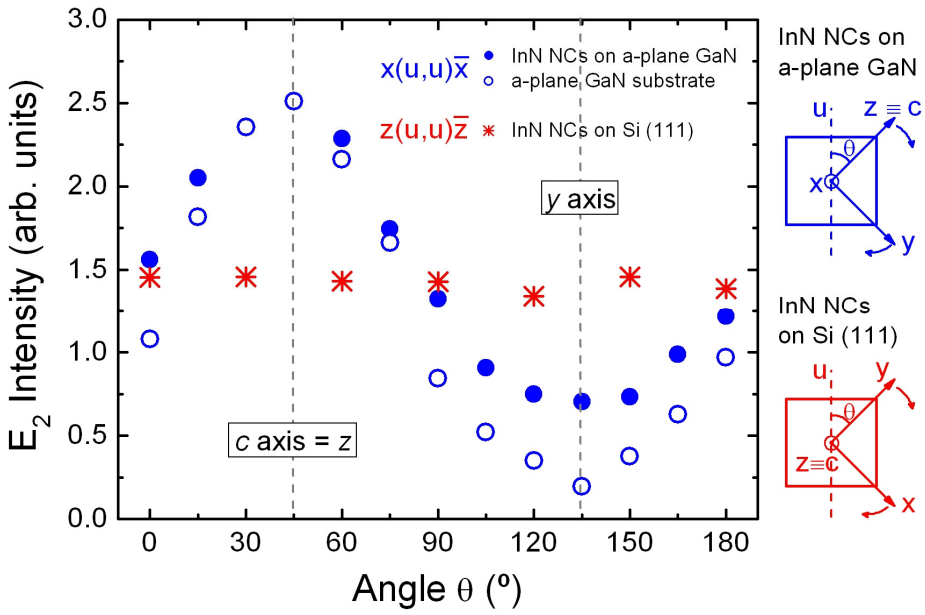


**Figure 5.19.** $E_2$ mode intensity as a function of the polarization angle θ defined in the right panels. Solid (open) blue circles correspond to *a*-plane InN NCs (GaN template). The red stars correspond to hexagonal (polar) InN NCs. The nominal scattering configurations are given in the right panels.

The main crystallographic axes were determined by the variation in the $E_2$ mode Raman intensity as the light polarization direction was changed. For this purpose, the sample-holder was mounted on a rotary platform. Measurements were performed again in backscattering configuration along the growth axis. The incident and scattered light polarization was fixed parallel to a direction, named as *u*-direction in the right panels of Figure 5.19. Then, the samples were rotated and the Raman spectra were taken at different angles. The $E_2$ mode intensity as a function of the angle $\theta$ is represented in Figure 5.19 for polar and non-polar InN NCs and for the *a*-plane GaN template. Regular selection rules imply that the intensity of the $E_2$ mode should be maximum for polarization perpendicular to the *c*-axis and zero for polarization parallel to it (Table 3.4). This is exactly what is observed for the *a*-plane GaN template (open blue circles). For the case of InN NCs grown along the *c*-axis, although the propagation inside the NCs occurs perpendicular to the *c*-axis, there will be always an orientation independent contribution with the polarization perpendicular to it ( $y(x,x)\bar{y}$ part in Figure 5.7(b)) due to the light scattering in all directions in each NC. Therefore, the $E_2$ mode intensity for the hexagonal InN NCs should remain unchanged for all angles, as it is experimentally observed (asterisks). Finally, for the *a*-plane InN NCs, their new selection rules presented in Figure 5.18 establish that $E_2$ intensity should present a

maximum or a minimum depending on which nominal scattering configuration is employed. For $x(y,y)\overline{x}$ nominal configuration, both *"real"* ones ( $z(y,y)\overline{z}$ and $y(x,x)\overline{y}$ ) contribute to the $E_2$ intensity, while for $x(z,z)\overline{x}$ nominal configuration only the $z(x,x)\overline{z}$ part will contribute. This is the situation observed in Figure 5.19 for these NCs (solid blue circles), where the intensity minimum of the $E_2$ mode does not reach zero as it occurs for GaN.

The results presented in this section confirm the wurtzite structure and orientation of the InN NCs grown on *a*-plane GaN templates given by the TEM images. The *c*- and *y*-axis are found to correspond to $\theta$ = 45º and 135º respectively, marked in Figure 5.19 by the vertical dashed lines.

## 5.4. Summary

InN NCs of different orientations have been investigated by Raman spectroscopy, showing their high crystal quality by the narrow $E_2$ phonon peak. The Raman spectra in both cases confirm the light propagation perpendicularly to the NC sidewalls, irrespective of the nominal scattering geometry.

Hexagonal (*c*-plane) InN NCs show the LO phonon-plasmon coupled mode ($L^-$) giving evidence of an EAL at their lateral non-polar surfaces. The $L^-/E_1$(LO) intensity ratio dependence on the column diameter and the excitation wavelength is partially explained in terms of the surface to volume ratio of the EAL and the strong light scattering by the NCs. Plan-view HR-TEM images show a 2-3 nm width $In_2O_3$ shell surrounding the NCs. The electron concentration can be varied by chemical etching. It increases by the immersion of the NCs in HCl which removes the $In_2O_3$ shell and decreases again when the sample oxidizes.

## 5.5. Future work

The most controversial inherent property of InN is the surface EAL observed in different InN structures (compact layers and NCs). As a result, a high conductivity is found in these systems which would in principle prevent the development of InN-based electronic devices. Therefore, any step towards the understanding of the origin of the EAL and its properties will be very interesting. In this section, several proposals are given in order to continue with the InN investigation.

First, a rigorous calculation of the scattering cross section as a function of wavelength and NCs size and shape is required for the quantitative understanding of Figure 5.8.

Secondly, the realization of PV-HR-TEM micrographs and Raman measurements on samples maintained in vacuum from growth to TEM measurements could help to determine the aging effects on the oxidation of the InN surfaces and how they are affected by the exposure to ambient atmosphere.

The presence of an $In_2O_3$ layer around the InN NCs could also be confirmed by Raman measurements if this layer presents a crystalline structure. Choosing the appropriate excitation energy in order to enhance the Raman intensity, the $In_2O_3$ vibrational modes could be observed in the Raman spectra.

Finally, the fabrication of *a*-plane InN NCs in substrates other than sapphire could permit the eventual observation of the $L^-$ coupled mode, so that the EAL at the surfaces of these NCs could also be investigated.

# Chapter 6

# Conclusions

The general conclusions of this work are presented in this chapter. They are classified in two parts, corresponding to the two different semiconductor systems investigated.

**3. InAs/GaAs quantum rings embedded in a photonic crystal microcavity**

3.1. Evidence of single photon emission in InAs quantum rings has been given by auto- and cross-correlation measurements of the exciton and biexciton transitions under continuous excitation. Values below 0.5 are found in the exciton and biexciton auto-correlation functions at zero delay. The cross-correlation function indicates sequential emission of photons from the biexciton to the exciton state and from the exciton to the ground state.

3.2. For similar emission intensities, the line shapes of the second order auto- and cross-correlation functions indicate characteristic rise times longer for the exciton emission than for the biexciton one. The probability of emitting two consecutive XX photons with short time delay is expected to be higher than for X photons at high excitation power, as a result of the fast recharging time.

3.3. The individual couplings of two distant quantum rings with the cavity mode of the same H1 calzone photonic crystal microcavity have been demonstrated by PL intensity enhancement and lifetime reduction (Purcell effect) of the quantum rings when the detuning between QR and CM emissions is decreased. The simultaneous coupling of both quantum rings to the same cavity mode is proved by the observation of Purcell effect in both quantum rings at the same time. Values of 30 μeV for the individual coupling strength of each quantum ring have been estimated from the modification of the spontaneous emission rates. Comparing these values with the QR and CM linewidths, weak coupling regime is determined in both cases.

3.4. Experimental evidence of the precise control of the linear polarization emission angle of one quantum ring coupled to the photonic crystal microcavity (QR-B) has been demonstrated by changing the energy detuning. The linear polarization of QR-B rotates continuously from perpendicular, at large detunings, to parallel to the CM one, at zero detuning. Moreover, the polarization angle of QR-B emission with respect to the CM polarization changes its sign for negative detunings, which is qualitatively explained in terms of hybridization of the QR and CM states. These results confirm that the mixing of QR and CM states in the weak coupling regime can be demonstrated by the polarization of the emitted photons.

3.5. A different polarization behaviour has been observed for other quantum ring (QR-A), which maintains its linear polarization parallel to the cavity mode one for all detunings. The precise position of each quantum ring with respect to the cavity center and their intrinsic dipole orientation are considered as the origin of these different behaviours.

3.6. An effective coupling between two distant quantum rings (QR-A and QR-B) mediated by the confined cavity mode of the microcavity has been demonstrated by PLE measurements. This interaction is proved by the increased emission intensity of each quantum ring upon the resonant excitation at the excited state of the other one. The coupling strength between the two quantum rings has been estimated to be approximately 2 μeV.

3.7. The most probable interaction mechanism between the two quantum rings involves the coherent coupling of their *s*-states by the cavity mode, as the two contributions to the QR emissions (intra- and inter-QR excitation) saturate in a similar way upon increasing the excitation power.

## 4. InN nanocolumns

4.1. InN nanocolumns grown on different substrates (Si(111), Si(001) and GaN$(11\bar{2}0)$ templates on *r*-plane sapphire) and different orientations have been characterized by inelastic light scattering. High crystalline quality is evidenced in all cases by the narrow $E_2$ mode observed.

4.2. The dependence of the Raman intensities on the scattering configuration measured in the different nanocolumns is understood assuming that the light propagation inside the nanocolumns is mostly perpendicular to their growth direction eventhough the nominal scattering direction is set parallel to it. The evidence is given by the observed vibrational modes in the Raman spectra of the nanocolumnar samples compared with the compact layer.

4.3. The presence of an electron accumulation layer at the lateral non-polar surfaces of the InN nanocolumns grown on silicon substrates has been demonstrated by the appearance of the $E_1$(LO) phonon-plasmon coupled mode $L^-$. The electron concentration at the surface can be estimated by the frequency of the $L^-$ coupled mode.

4.4. The $L^-$ intensity, originating from the surface electron accumulation layer, compared with the uncoupled $E_1$(LO) phonon, coming from the inner part of the nanocolumns, is found to increase as the fourth power of the excitation energy, revealing the strong elastic scattering that occur in the nanocolumnar samples.

4.5. The $L^-/E_1$(LO) intensity ratio also depends on the average diameter of the nanocolumns. It decreases as the nanocolumn diameter increases for an excitation wavelength of 632.8 nm. However, the opposite trend is observed for 514.5 and 457.9 nm excitation wavelengths. A competition between the surface to volume ratio contribution and the size- and wavelength-dependent elastic scattering qualitatively explains these different dependences.

4.6. A new preparation method of TEM specimens which fulfills the requirements for high resolution has been performed for plan-view imaging of nanocolumnar samples. An $In_2O_3$ surrounding layer of few nanometers thickness is observed in the plan-view HR-TEM images of the InN nanocolumns grown on silicon substrates, which influences the surface electron density.

4.7. The electron concentration at the surface has been shown to vary upon chemical treatment. By the immersion in HCl acid, the $In_2O_3$ layer is removed and the electron density increases as a result of the stronger band bending in InN surfaces than in $In_2O_3$ ones. The subsequent oxidation of the surfaces leads again to a reduction of the electron concentration.

4.8. The main crystallographic axes of the InN nanocolumns grown on *a*-plane GaN templates have been determined by the polarization dependence Raman spectra, confirming the *a*-plane orientation of these nanocolumns.

# References


[1] D. Bimberg, M. Grundmann and N.N. Ledentsov, *Quantum Dot Heterostructures*, John Wiley & Sons 1999.

[2] L. Jacak, P. Hawrylak and A. Wójs, *Quantum Dots*, Springer-Verlag Berlin Heidelberg 1998.

[3] D. Gammon and D.G. Steel, *Physics Today* October 36 (2002).

[4] M. Abbarchi, C.A. Mastrandrea, A. Vinattieri, S. Sanguinetti, T. Mano, T. Kuroda, N. Koguchi, K. Sakoda and M. Gurioli*, Phys. Rev. B* **79,** 085308 (2009).

[5] M. Bayer, M. Korkusinski, P. Hawrylak, T. Gutbrod, M. Michel and A. Forchel, *Phys. Rev. Lett.* **90,** 186801 (2003).

[6] N.A.J.M. Kleemans, I.M.A. Bominaar-Silkens, V.M. Fomin, V.N. Gladilin, D. Granados, A.G. Taboada, J.M. García, P. Offermans, U. Zeitler, P.C.M. Christianen, J.C. Maan, J.T. Devreese and P.M. Koenraad, *Phys. Rev. Lett.* **99,** 146808 (2007).

[7] K. Vahala, *Optical Microcavities*, World Scientific Publishing 2004.

[8] M. Fox, *Quantum Optics, An Introduction*, Oxford University Press 2006.

[9] Y. Yamamoto, F. Tassone and H. Cao, *Semiconductor Cavity Quantum Electrodynamics*, Springer-Verlag Berlin Heidelberg 2000.

[10] Y. Yamamoto and A. Imamoğlu, *Mesoscopic Quatum Optics*, John Wiley & Sons 1999.

[11] C.C. Gerry and P.L. Knight, *Introductory Quantum Optics*, Cambridge University Press 2005.

[12] A.J. Bennet, D.C. Unitt, P. See, A.J. Shields, P. Atkinson, K. Cooper and D.A. Ritchie, *Appl. Phys. Lett.* **86,** 181102 (2005).

[13] E.M. Purcell, *Phys. Rev. B* **69**, 681 (1946).

[14] D. Englund, D. Fattal, E. Waks, G. Solomon, B. Zhang, T. Nakaoka, Y. Arakawa, Y. Yamamoto and J. Vučković, *Phys. Rev. Lett.* **95,** 013904 (2005).

[15] K. Hennessy, A. Badolato, M. Winger, D. Gerace, M. Atatüre, S. Gulde, S. Fält, E.L. Hu and A. Imamoğlu, *Nature* **445**, 896 (2007).

[16] J.P. Reithmaier, G. Sek, A. Löffler, C. Hofmann, S. Kuhn, S. Reitzenstein, L.V. Keldysh, V.D. Kulakovskii, T.L. Reinecke and A. Forchel, *Nature* **432**, 197 (2004).

[17] T. Yoshie, A. Scherer, J. Hendrickson, G. Khitrova, H.M. Gibbs, G. Rupper, C. Ell, O. B. Shchekin and D.G. Deppe, *Nature* **432**, 200 (2004).

[18] G. Burkard and A. Imamoğlu, *Phys. Rev. B* **74,** 041307(R) (2006).

[19] E. del Valle, *Phys. Rev. A* **81,** 053811 (2010).

[20] A. Imamoğlu, D.D. Awschalom, G. Burkard, D.P. DiVincenzo, D. Loss, M. Sherwin and A. Small, *Phys. Rev. Lett.* **83,** 4204 (1999).

[21] A. Imamoğlu, S. Fält, J. Dreiser, G. Fernández, M. Atatüre, K. Hennessy, A. Badolato and D. Gerace, *J. Appl. Phys.* **101**, 081602 (2007).

[22] H. Altug and J. Vuckovic, *Appl. Phys. Lett.* **84,** 161 (2004).

[23] S. Vignolini, F. Intonti, M. Zani, F. Riboli, D.S. Wiersma, L.H. Li, L. Balet, M. Francardi, A. Gerardino, A. Fiore and M. Gurioli, *Appl. Phys. Lett.* **94,** 151103 (2009).

[24] A. Mohan, M. Felici, P. Gallo, B. Dwir, A. Rudra, J. Faist and E. Kapon, *Nature Photonics* **4,** 302 (2010).

[25] L. Besombes, K. Kheng and D. Martrou, *Phys. Rev. Lett.* **85,** 425 (2000).

[26] T. Jennewein, C. Simon, G. Weihs, H. Weinfurter and A.Zeilinger, *Phys. Rev. Lett.* **84,** 4729 (2000).

[27] E. Knill, R. Laflamme and G.J. Milburn, *Nature* **409**, 46 (2001).

[28] A. Daraei, D. Sanvitto, J.A. Timpson, A.M. Fox, D.M. Whittaker, M.S. Skolnick, P.S. S. Guimarães, H. Vinck, A. Tahraoui, P.W. Fry, S.L. Liew and M. Hopkinson, *J. Appl. Phys.* **102**, 043105 (2007).

[29] D.C. Unitt, A.J. Bennett, P. Atkinson, D.A. Ritchie and A.J. Shields, *Phys. Rev. B* **72,** 033318 (2005).

[30] R. Oulton, B.D. Jones, S. Lam, A.R.A. Chalcraft, D. Szymanski, D. O'Brien, T.F. Krauss, D. Sanvitto, A.M. Fox, D.M. Whittaker, M. Hopkinson and M.S. Skolnick, *Opt. Express* **15**, 17221 (2007).

[31] W.H. Chang, W.Y. Chen, H.S. Chang, T.M. Hsu, T.P. Hsieh and J.I. Chyi, *J. Appl. Phys.* **98**, 034306 (2005).

[32] M.A. Sánchez-García, J. Grandal, E. Calleja, S. Lazić, J.M. Calleja and A. Trampert, *phys. stat. sol. (b)* **243,** 1490 (2006).

[33] J. Grandal, M.A. Sánchez-García, E. Calleja, E. Luna and A. Trampert, *Appl. Phys. Lett.* **91**, 021902 (2007).

[34] J. Grandal and M.A. Sánchez-García, *J. Crys. Growth* **278,** 373 (2005).

[35] V.Y. Davydov, A.A. Klochikhin, V.V. Emtsev, D.A. Kurdyukov, S.V. Ivanov, V.A. Vekshin, F. Bechstedt, J. Furthmüller, J. Aderhold, J. Graul, A.V. Mudryi, H. Harima, A. Hashimoto, A. Yamamoto and E.E. Haller, *phys. stat. sol. (b)* **234,** 787 (2002).

[36] P.D.C. King, T.D. Veal, C.F. McConville, F. Fuchs, J. Furthmüller, F. Bechstedt, P. Schley, R. Goldhahn, J. Schörmann, D.J. As, K. Lischka, D. Muto, H. Naoi, Y. Nanishi, H. Lu and W.J. Schaff, *Appl. Phys. Lett.* **91**, 092101 (2007).

[37] M.A. Sánchez-García, E. Calleja, E. Monroy, F.J. Sanchez, F. Calle, E. Muñoz and R. Beresford, *J. Crys. Growth* **183,** 23 (1998).

[38] S. Ishizawa, K. Kishino and A. Kikuchi, *Appl. Phys. Express* **1,** 015006 (2008).

[39] J. Ristić, E. calleja, M.A. Sánchez-García, J.M. Ulloa, J. Sánchez-Páramo, J.M. Calleja, U. Jahn, A. Trampert and K.H. Ploog, *Phys. Rev. B* **68**, 125305 (2003).

[40] A. Kikuchi, M. Kawai, M. Tada and K. Kishino, *Jpn. J. Appl. Phys.* **43,** L1524 (2004).

[41] P. Michler, *Single Semiconductor Quantum Dots*, Springer-Verlag Berlin Heidelberg 2009.

[42] M. Bayer, O. Stern, P. Hawrylak, S. Fafard and A. Forchel, *Nature* **405**, 923 (2000).

[43] G.A. Narvaez, G. Bester and A. Zunger, *J. Appl. Phys.* **98**, 043708 (2005).

[44] S. Rodt, A. Schliwa, K. Pötschke, F. Guffarth and D. Bimberg, *Phys. Rev. B* **71,** 155325 (2005).

[45] D. Sarkar, H.P. van der Meulen, J.M. Calleja, J.M. Becker, R.J. Haug and K. Pierz, *J. Appl. Phys.* **100,** 023109 (2006).

[46] K. Brunner, G. Abstreiter, G. Böhm, G. Tränkle and G. Weimann, *Phys. Rev. Lett.* **73,** 1138 (1994).

[47] G.A. Narvaez, G. Bester and A. Zunger, *Phys. Rev. B* **72,** 245318 (2005).

[48] U.W. Pohl, R. Seguin, S. Rodt, A. Schliwa, K. Pötschke and D. Bimberg, *Physica E* **35,** 285 (2006).

[49] D. Granados and J.M. García, *Appl. Phys. Lett.* **82,** 2401 (2003).

[50] R. J. Warburton, C. Schäflein, D. Haft, F. Bickel, A. Lorke, K. Karrai, J.M. Garcia, W. Schoenfeld and P.M. Petroff, *Nature* **405,** 926 (2000).

[51] B. Alén, J. Martínez-Pastor, D. Granados and J.M. García, *Phys. Rev. B* **72,** 155331 (2005).

[52] S.S. Li and J.B. Xia, *J. Appl. Phys.* **89,** 3434 (2001).

[53] K.J. Vahala, *Nature* 424, 839 (2003).

[54] E. Peter, P. Senellart, D. Martrou, A. Lemaître, J. Hours, J.M. Gérard and J. Bloch, *Phys. Rev. Lett.* **95,** 067401 (2005).

[55] B. Gayral, J.M. Gérard, A. Lemaître, C. Dupuis, L. Manin and J.L. Peluoard, *Appl. Phys. Lett.* **75,** 1908 (1999).

[56] J.D. Joannopoulos, R.D. Meade and J.N. Winn, *Photonic Crystals: Molding the Flow of Light*, Princeton University Press 2008.

[57] K. Busch, S. Lölkes, R.B. Wehrspohn and H. Föll, *Photonic Crystals: Advances in design, fabrication and characterization*, WILEY-VCH Verlag, 2004.

[58] A. Badolato, K. Hennesy, M. Atatüre, J. Dreiser, E. Hu, P.M. Petroff and A. Imamoğlu, *Science* **308,** 1158 (2005).

[59] A. Tandaechanurat, S. Iwamoto, M. Nomura, N. Kumagai and Y. Arakawa, *Opt. Express* **16,** 448 (2008).

[60] R. Coccioli, M. Boroditsky, K.W. Kim, Y. Rahmat-Samii and E. Yablonovitch, *IEE Proc. Optoelectron.* 145, 391 (1998).

[61] Y. Akahane, T. Asano, B.S. Song and S. Noda, *Nature* **425**, 944 (2003).

[62] H. Mabuchi and A.C. Doherty, *Science* 298, 1372 (2002) and references therein.

[63] S. Reitzenstein, C. Hofmann, A. Löffler, A. Kubanek, J.P. Reithmaier, M. Kamp, V.D. Kulakovskii, L.V. Reinecke and A. Forchel, *phys. stat. sol. (b)* **10**, 2224 (2006).

[64] D. Press, S. Götzinger, S. Reitzenstein, C. Hofmann, A. Löffler, M. Kamp, A. Forchel and Y. Yamamoto, *Phys. Rev. Lett.* **98**, 117402 (2007).

[65] M. Winger, A. Badolato, K.J. Hennesy, E.L. Hu and A. Imamoğlu, *Phys. Rev. Lett.* **101**, 226808 (2008).

[66] Y. Ota, M. Shirane, M. Nomura, N. Kumagai, S. Ishida, S. Iwamoto, S. Yorozu and Y. Arakawa, *Appl. Phys. Lett.* **94**, 033102 (2009).

[67] S. Münch, S. Reitzenstein, P. Franeck, A. Löffler, T. Heindel, S. Höfling, L. Worschech and A. Forchel, *Opt. Express* **17**, 12821 (2009).

[68] F.P. Laussy, E. del Valle and C. Tejedor, *Phys. Rev. Lett.* **101,** 083601 (2008).

[69] A. Laucht, N. Hauke, J.M. Villas-Bôas, F. Hofbauer, G. Böhm, M. Kaniber and J.J. Finley, *Phys. Rev. Lett.* **103,** 087405 (2009).

[70] J. Suffczyński, A. Dousse, K. Gauthron, A. Lemaître, I. Sagnes, L. Lanco, J. Bloch, P. Voisin and P. Senellart, *Phys. Rev. Lett.* **103,** 027401 (2009).

[71] A. Dousse, J. Suffczyński, R. Braive, A. Miard, A. Lemaître, I. Sagnes, L. Lanco, J. Bloch, P. Voisin and P. Senellart, *Appl. Phys. Lett.* **94**, 121102 (2009).

[72] M. Kaniber, A. Laucht, A. Neumann, J.M. Villas-Bôas, M. Bichler, M.C. Amann and J.J. Finley, *Phys. Rev. B* **77** 161303(R) (2008).

[73] S. Ates, S.M. Ulrich, A. Ulhaq, S. Reitzenstein, A. Löffler, S. Höfling, A. Forchel and P. Michler, *cond-mat* arXiv:0902.3455v2 (2009).

[74] Y. Ota, S. Iwamoto, N. Kumagai and Y. Arakawa, *cond-mat* arXiv:0908.0788 (2009).

[75] U. Hohenester, A. Laucht, M. Kaniber, N. Hauke, A. Neumann, A. Mohtashami, M. Seliger, M. Bichler and J.J. Finley, *Phys. Rev. B* **80** 201311(R) (2009).

[76] M. Winger, PhD dissertation, Eidgenössische Technische Hochschule (ETH), Zürich (2009).

[77] M. Winger, T. Volz, G. Tarel, S. Portolan, A. Badolato, K.J. Hennesy, E.L. Hu, A. Beveratos, J. Finley, V. Savona and A. Imamoğlu, *Phys. Rev. Lett.* **103,** 207403 (2009).

[78] K. Karrai, R.J. Warburton, C. Schulhauser, A. Högele, B. Urbaszek, E.J. McGhee, A.O. Govorov, J.M. García, B.D. Gerardot and P.M. Petroff, *Nature* **427**, 135 (2004).

[79] O. Gywat, F. Meier, D. Loss and D.D. Awschalom, *Phys. Rev. B* **73**, 125336 (2006).

[80] S Reitzenstein, A. Löffler, A. Kubanek, M. Kamp, J.P. Reithmaier, A. Forchel, V.D. Kulakovskii, L.V. Keldysh, I.V. Ponomarev and T.L. Reinecke, *Opt. Lett.* **31,** 1738 (2006).

[81] H.J. Krenner, M. Sabathil, E.C. Clark A. Kress, D. Schuh, M. Bichler, G. Abstreiter and J.J. Finley, *Phys. Rev. Lett.* **94,** 057402 (2005).

[82] H. Kim, S.M. Thon, P.M. Petroff and D. Bouwmeester, *Appl. Phys. Lett.* **95**, 243107 (2009).

[83] A. Laucht, J.M. Villas-Bôas, S. Stobbe, N. Hauke, F. Hofbauer, G. Böhm, P. Lodahl, M. Kaniber and J.J. Finley, *cond-mat* arXiv:0912.3685v1 (2009).

[84] H. Morkoç, *Handbook of Nitride Semiconductor and Devices, Vol. 1: Materials Properties, Physics and Growth*, WILEY-VCH Verlag Weinheim 2008.

[85] F. Bernardini, V. Fiorentini and D. Vanderbilt, *Phys. Rev. B* **56,** R10024 (1997).

[86] T.D. Veal, C.F. McConville and W.J. Schaff, Indium Nitride and Related Alloys, Taylor and Francis Group 2010.

[87] T.L. Tansley and C.P. Foley, *J. Appl. Phys.* **59**, 3241 (1986).

[88] W. Walukiewicz, J.W. Ager III, K.M. Yu, Z. Liliental-Weber, J. Wu, S.X. Li, R.E. Jones and J.D. Denlinger, *J. Phys. D* **39,** R83 (2006).

[89] P.D.C. King, T.D. Veal, P.H. Jefferson, S.A. Hatfield, L.F.J. Piper, C.F. McConville, F. Fuchs, J. Furthmüller, F. Bechstedt, H. Lu and W.J. Schaff, *Phys. Rev. B* **77,** 045316 (2008).

[90] J. Wu, W. Walukiewicz, K.M. Yu, J.W. Ager III, E.E. Haller, H. Lu and W.J. Schaff, *Phys. Rev. B* **66,** 201403 (2002).

[91] J. Wu, W. Walukiewicz, S.X. Li, R. Armitage, J.C. Ho, E.R. Weber, E.E. Haller, H. Lu, W.J. Schaff, A- Barcz and R. Jakiela, *Appl. Phys. Lett.* **84**, 2805 (2004).

[92] H. Lu, W.J. Schaff, L.F. Eastman and C.E. Stutz, *Appl. Phys. Lett.* **82**, 1736 (2003).

[93] K.A. Rickert, A.B. Ellis, F.J. Himpsel, H. Lu, W. Schaff, J.M. Redwing, F. Dwikusuma and T.F. Kuech, *Appl. Phys. Lett.* **82**, 3254 (2003).

[94] I. Mahboob, T.D. Veal, C.F. McConville, H. Lu and W.J. Schaff, *Phys. Rev. Lett.* **92,** 036804 (2004).

[95] L. Colakerol, T.D. Veal, H.K. Jeong, L. Plucinski, A. DeMasi, T. Learmonth, P.A. Glans, S. Wang, Y. Zhang, L.F.J. Piper, P.H. Jefferson, A. Fedorov, T.C. Chen, T.D. Moustakas, C.F. McConville and K.E. Smith, *Phys. Rev. Lett.* **97,** 237601 (2006).

[96] T. Hoffmann, V. Darakchieva, B. Monemar, H. Lu, W.J. Schaff and M. Schubert, *J. Electron. Mater.* **37,** 611 (2008).

[97] I. Mahboob, T.D. Veal, L.F.J. Piper, C.F. McConville, H. Lu, W.J. Schaff, J. Furthmüller and F. Bechstedt, *Phys. Rev. B* **69,** 201307 (2004).

[98] D. Segev and C.G. Van de Walle, *Europhys. Lett.* **76,** 305 (2006).

[99] D. Segev and C.G. Van de Walle, *J. Crys. Growth* **300,** 199 (2007).

[100] C.L. Wu, H.M. Lee, C.T. Kuo, C.H. Chen and S. Gwo, *Phys. Rev. Lett.* **101,** 106803 (2008).

[101] P.D.C. King, T.D. Veal, D.J. Payne, A. Bourlange, R.G. Egdell and C.F. McConville, *Phys. Rev. Lett.* **101,** 116808 (2008).

[102] E.A. Davis, S.F.J. Cox, R.L. Lichti and C.G. Van de Walle, *Appl. Phys. Lett.* **82**, 592 (2003).

[103] N.W. Ashcroft and N.D. Mermin, *Solid State Physics*, Thomson Learning 1976.

[104] C.A. Arguello, D.L. Rousseau and S.P.S. Porto, *Phys. Rev.* **181,** 1351 (1969).

[105] M.A. Stroscio and M. Dutta, *Phonons in Nanostructures*, Cambridge University Press 2004.

[106] I. Gorczyca, N.E. Christensen, E.L. Peltzer y Blancá and C.O. Rodriguez, *Phys. Rev. B* **51,** 11936 (1995).

[107] L. Bergman, D. Alexson, R.J. Nemanich, M. Dutta, M.A. Stroscio, C. Balkas and R.F. Davis, *MRS Internet J. Nitride Semicond. Res.* **4S1,** G6.65 (1999).

[108] C. Bungaro, K. Rapcewicz and J. Bernholc, *Phys. Rev. B* **61,** 6720 (2000).

[109] V.Y. Davydov, V.V. Emtsev, I.N. Goncharuk, A.N. Smirnov, V.D. Petrikov, V.V. Mamutin, V.A. Vekshin, S.V. Ivanov, M.B. Smirnov and T. Inushima, *Appl. Phys. Lett.* **75**, 3297 (1999).

[110] T. Inushima, T. Shiraishi and V.Y. Davydov, *Solid State Commun.* **110,** 491 (1999).

[111] G. Kaczmarczyk, A. Kaschner, S. Reich, A. Hoffmann, C. Thomsen, D.J. As, A.P. Lima, D. Schikora, K. Lischka, R. Averbeck and H. Riechert, *Appl. Phys. Lett.* **76,** 2122 (2000).

[112] J.S. Dyck, K. Kim, S. Limpijumnong, W.R.L. Lambrecht, K. Kash and J.C. Angus, *Solid State Commun.* **114,** 355 (2000).

[113] A. Kasic, M. Schubert, Y. Saito, Y. Nanishi and G. Wagner, *Phys. Rev. B* **65,** 115206 (2002).

[114] E. Burstein, A. Pinczuk and S. Iwasa, *Phys. Rev.* **157,** 611 (1967).

[115] F. Demangeot, C. Pinquier, J. Frandon, M. Gaio, O.Briot, B. Maleyre, S. Ruffenach and B. Gil, *Phys. Rev. B* **71,** 104305 (2005).

[116] H. Harima, S. Nakashima and T. Uemura, *J. Appl. Phys.* **78**, 1996 (1995).

[117] M.V. Klein, B.N. Ganguly and P.J. Colwell, *Phys. Rev. B* **6,** 2380 (1972).

[118] Y.M. Chang, C.T. Chuang, C.T. Chia, K.T. Tsen, H. Lu and W.J. Schaff, *Appl. Phys. Lett.* **85**, 5224 (2004).

[119] H. Harima, *J. Phys.: Condens. Matter* **14,** R967 (2002).

[120] M. Ramsteiner, O. Brandt and K.H. Ploog, *Phys. Rev. B* **58,** 1118 (1998).

[121] T. Kuykendall, P. Ulrich, S. Aloni and P. Yang, *Nature Materials* **6,** 951 (2007).

[122] J. Grandal, M.A. Sánchez-García, F. Calle and E. Calleja, *phys. stat. sol. (c)* **2,** 2289 (2005).

[123] H.Y. Chen, C.H. Shen, H.W. Lin, C.H. Chen, C.Y. Wu, S. Gwo, V.Y. Davydov and A.A. Klochikhin, *Thin Solid Films* **515,** 961 (2006).

[124] K. Xu and A. Yoshikawa, *Appl. Phys. Lett.* **83**, 251 (2003).

[125] X. Wang, S.B. Che, Y. Ishitani and A. Yoshikawa, *phys. stat. sol. (c)* **3,** 1561 (2006).

[126] J. Grandal, PhD dissertation, Universidad Politécnica de Madrid, 2009.

[127] Z.H. Lan, W.M. Wang, C.L. Sun, S.C. Shi, C.W. Hsu, T.T. Chen, K.H. Chen, C.C. Chen, Y.F. Chen and L.C.. Chen, *J. Crys. Growth* **269,** 87 (2004).

[128] J. Grandal, M.A. Sánchez-García, E. Calleja, E. Gallardo, J.M. Calleja, E. Luna, A. Trampert and U. Jahn, *Appl. Phys. Lett.* **94**, 221908 (2009).

[129] S. Lazić, E. Gallardo, J.M. Calleja, F. Agulló-Rueda, J. Grandal, M.A. Sánchez-García, E. Calleja, E. Luna and A. Trampert, *Phys. Rev. B* **76,** 205319 (2007).

[130] J. Segura-Ruiz, N. Garro, A. Cantarero, C. Denker, J. Malindretos and A. Rizzi, *Phys. Rev. B* **79,** 115305 (2009).

[131] S. Lazić, E. Gallardo, J.M. Calleja, F. Agulló-Rueda, J. Grandal, M.A. Sánchez-García, E. Calleja, *Physica E* **40,** 2087 (2008).

[132] S. Lazić, PhD dissertation, Universidad Autónoma de Madrid, 2008.

[133] R. Calarco and M. Marso, *Appl. Phys. A: Mater. Sci. Process.* **87,** 499 (2007).

[134] E. Calleja, J. Grandal, M.A. Sánchez-García, M. Niebelschütz, V. Cimalla and O. Ambacher, *Appl. Phys. Lett.* **90**, 262110 (2007).

[135] J. Segura-Ruiz, N. Garro, A. Cantarero, F. Iikawa, C. Denker, J. Malindretos and A. Rizzi, *phys. stat. sol. (c)* **6,** S553 (2009).

[136] P.Y. Yu and M. Cardona, *Fundamentals of Semiconductors: Physics and Material Properties*, Springer-Verlag Berlin Heidelberg 1999.

[137] C.F. Klingshirn, *Semiconductor Optics*, Springer-Verlag Berlin Heidelberg 1995.

[138] W. Becker, Advanced Time-Correlated Single Photon Counting Techniques, Springer-Verlag Berlin Heidelberg 2005.

[139] N.V. Tkachenko, *Optical Spectroscopy: Methods and Instrumentation*, Elsevier B.V. 2006.

[140] H. Abramczyk, *Introduction to Laser Spectroscopy*, Elsevier B.V. 2005.

[141] R. Loudon, The Quantum Theory of Light, Oxford University Press 2000.

[142] X.T. Zou and L. Mandel, *Phys. Rev. A* **41,** 475 (1990).

[143] H.J. Kimble, M. Dagenais and L. Mandel, *Phys. Rev. Lett.* **39,** 691 (1977).

[144] M. Cardona, Light Scattering in Solids II, Springer-Verlag Berlin Heidelberg 1982.

[145] W.H. Weber and R. Merlin, Raman Scattering in Materials Science, Springer-Verlag Berlin Heidelberg 2000.

[146] R. Loudon, *Advances in Physics* **50,** 813 (2001).

[147] R.M. Martin, *Phys. Rev. B* **4,** 3676 (1971).

[148] X.B. Zhang, T. Taliercio, S. Kolliakos and P. Lefebvre, *J. Phys.: Condens. Matter* **13,** 7053 (2001).

[149] M.O. Manasreh, *III-Nitride Semiconductors Optical Properties I*, Taylor & Francis 2002.

[150] S. Strauff, M.T. Rakher, I. Carmeli, K. Hennesy, C. Meier, A. Badolato, M.J.A. DeDood, P.M. Petroff, E.L. Hu, E.G. Gwinn and D. Bouwmeester, *Appl. Phys. Lett.* **88**, 043116 (2006).

[151] S. Mosor, J. Hendrickson, B. C. Richards, J. Sweet, G. Khitrova, H. M. Gibbs, T. Yoshie, A. Scherer, O. B. Shchekin and D. G. Deppe, *Appl. Phys. Lett.* **87**, 141105 (2005).

[152] E. Fuchs, H. Oppolzer and H. Rehme, *Particle Beam Microanalysis: Fundamentals, Methods and Applications*, Wiley and Sons Australia 1990.

[153] L. Reimer and H. Kohl, *Transmission Electron Microscopy*, Springer Series in Optical Science 2008.

[154] J.C.H. Spence, *High-Resolution Electron Microscopy*, Oxford University Press 2003.

[155] L. Weaver, *Microscopy Research and Technique* **36,** 368 (1997).

[156] Y. Liu, R. Wang, X. Guo and J. Dai, *Materials Characterization* **58,** 666 (2007).

[157] P. Offermans, P. M. Koenraad, J. H. Wolter, D. Granados, J. M. García, V. M. Fomin, V. N. Gladilin and J. T. Devreese, *Appl. Phys. Lett.* **87,** 131902 (2005).

[158] K. Hennessy, C. Högerle, E. Hu, A. Badolato and A. Imamoğlu, *Appl. Phys. Lett.* **89,** 041118 (2006).

[159] L.J. Martínez, PhD dissertation, Universidad Autónoma de Madrid (2009).

[160] P. Michler, A. Imamoglu, M.D. Mason, P.J. Carson, G.F. Strouse and S.K. Buratto, *Nature* **406,** 968 (2000).

[161] B. Lounis, H.A. Bechtel, D. Gerion, P. Alivisatos and W.E. Moerner, *Chem. Phys. Lett.* **329,** 399 (2000).

[162] D.V. Regelman, U. Mizrahi, D. Gershoni, E. Ehrenfreund, W.V. Schoenfeld and P.M. Petroff, *Phys. Rev. Lett.* **87,** 257401 (2001).

[163] V. Zwiller, H. Blom, P. Jonsson, N. Panev, S. Jeppesen, T. Tsegaye, E. Goobar, M.E. Pistol, L. Samuelson and G. Björk, *Appl. Phys. Lett.* **78,** 2476 (2001).

[164] A. Kiraz, S. Fälth, C. Becher, B. Gayral, W.V. Schoenfeld, P.M. Petroff, L. Zhang, E. Hu and A. Imamoğlu, *Phys. Rev. B* **65,** 161303(R) (2002).

[165] C. Santori, M. Pelton, G. Solomon, Y. Dale and Y. Yamamoto, *Phys. Rev. Lett.* **86,** 1502 (2001).

[166] S. Kimura, H. Kumano, M. Endo, I. Suemune, T. Yokoi, H. Sasakura, S. Adachi, S. Muto, H.Z. Song, S. Hirose and T. Usuki, *Jpn. J. Appl. Phys.* **44,** L793 (2005).

[167] M. Reischle, G.J. Beirne, W.M. Schulz, M. Eichfelder, R. Roβbach, M. Jetter and P. Michler, *Opt. Express* **16,** 12771 (2008).

[168] G. Sallen, A. Tribu, T. Aichele, R. André, L. Besombes, C. Bougerol, S. Tatarenko, K. Kheng and J.Ph. Poizat, *Phys. Rev. B* **80,** 085310 (2009).

[169] D. Sarkar, H.P. van der Meulen, J.M. Calleja, J.M. Meyer, R.J. Haug and K. Pierz, *Phys. Rev. B* **78,** 241305 (2008).

[170] E. Moreau, I. Robert, L. Manin, V. Thierry-Mieg, J.M. Gérard and I. Abram, *Phys. Rev. Lett.* **87,** 183601 (2001).

[171] M.H. Baier, A. Malko, E. Pelucchi, D.Y. Oberli and E. Kapon, *Phys. Rev. B* **73,** 205321 (2006).

[172] H. Thyrrestrup, L. Sapienza and P. Lodahl, *arXiv:* 1003.3346v1 (2010).

[173] M.E. Gaevski, W. Sun, J. Yang, V. Adivarahan, A. Sattu, I. Mokina, M. Shatalov, G. Simin and M.A. Khan, *phys. stat. sol. (a)* **203,** 1696 (2006).

[174] Z. Liliental-Weber, H. Lu, W.J. Schaff, O. Kryliouk, H.J. Park, J. Mangum and T. Anderson, *phys. stat. sol. (c)* **4,** 2469 (2007).

[175] Z. Liliental-Weber, M. Hawkridge, J. Mangum and O. Kryliouk, *phys. stat. sol. (c)* **5,** 1795 (2008).

[176] M. Born and E. Wolf, Principles of Optics, Pergamon Press 1980.

[177] D. González, J.G. Lozano, M. Herrera, N.D. Browning, S. Ruffenach, O. Briot and R. García, *J. Appl. Phys.* **105,** 013527 (2009).

[178] V. Cimalla, V. Lebedev, C.Y. Wang, M. Ali, G. Ecke, V.M. Polyakov, F. Schwierz, O. Ambacher, H. Lu and W.J. Schaff, *Appl. Phys. Lett.* **90,** 152106 (2007).

[179] V. Lebedev, C.Y. Wang, S. Hauguth, V. Polyakov, F. Schwierz, V. Cimalla, T. Kups, F.M. Morales, J.G. Lozano, D. González, M. Himmerlich, J.A. Schaefer, S. Krischok and O. Ambacher, *phys. stat. sol. (c)* **5,** 495 (2008).

[180] V.Y. Davydov, Y.E. Kitaev, I.N. Goncharuk, A.N. Smirnov, J. Graul, O. Semchinova, D. Uffmann, M.B. Smirnov, A.P. Mirgorodsky and R.A. Evarestov, *Phys. Rev. B* **58,** 12899 (1998).

[181] U. Haboeck, H. Siegle, A. Hoffmann and C. Thomsen, *phys. stat. sol. (c)* **0,** 1710 (2003).

# List of Publications

## Publications related with this Thesis:

1. "Phonon-plasmon coupling in electron surface accumulation layers in InN nanocolumns", S. Lazić, E. Gallardo, J.M. Calleja, F. Agulló-Rueda, J. Grandal, M.A. Sánchez-García, E. Calleja, E. Luna and A. Trampert, **Phys. Rev. B**, **76**, 205319 (2007).
2. "InN nanocolumns", J. Grandal, M. A. Sánchez-García, E. Calleja, S. Lazić, E. Gallardo, J. M. Calleja, E. Luna, A. Trampert, M. Niebelschütz, V. Cimalla and O. Ambacher, Book Chapter, **Indium Nitride and Related Alloys**, edited by T. D. Veal, C. F. McConville and W. J. Schaff, CRC Press, Taylor & Francis Group (2009).
3. "InN nanocolumns grown by plasma-assisted molecular beam epitaxy on A-plane GaN templates", J. Grandal, M. A. Sánchez-García, E. Calleja, E. Gallardo, J. M. Calleja, E. Luna, A. Trampert and U Jahn, **Appl. Phys. Lett. 94**, 221908 (2009).
4. "Single photon emission by semiconductor quantum rings in a photonic crystal", E. Gallardo, L.J. Martínez, A.K. Nowak, D. Sarkar, D.Sanvitto, H.P. van der Meulen, J.M. Calleja, I. Prieto, D. Granados, A.G. Taboada, J.M. García and P.A. Postigo, **J. Opt. Soc. Am. B 27**, A21-A24 (2010).
5. "Optical coupling of two distant InAs/GaAs quantum dots by a photonic-crystal microcavity", E. Gallardo, L.J. Martínez, A.K. Nowak, D. Sarkar, H.P. van der Meulen, J.M. Calleja, C. Tejedor, I. Prieto, D. Granados, A.G. Taboada, J.M. García and P.A. Postigo, **Phys. Rev. B 81,** 193301 (2010).
6. "Emission Polarization Control in Semiconductor Quantum Dots coupled to a Photonic Crystal Microcavity", E. Gallardo, L.J. Martínez, A.K. Nowak, H.P. van der Meulen, J.M. Calleja, C. Tejedor, I. Prieto, D. Granados, A.G. Taboada, J.M. García and P.A. Postigo, **Opt. Express 18,** 13301 (2010).

Conference proceedings:

7. "Raman scattering by longitudinal optical phonons in InN nanocolumns grown on Si(111) and Si(001) substrates", S. Lazić, E. Gallardo, J.M. Calleja, F. Agulló-Rueda, J. Grandal, M.A. Sánchez-García and E. Calleja, **Physica E:** Low-Dimensional Systems and Nanostructures **40**, 2087-2090 (2008).

8. "Raman scattering by coupled plasmon-LO phonons in InN nanocolumns", S. Lazić, E. Gallardo, J.M. Calleja, F. Agulló-Rueda, J. Grandal, M.A. Sánchez-García and E. Calleja, **phys. stat. sol. (c) 5**, No. 6, 2345-2348 (2008).
9. "Electron accumulation layers in InN nanocolumns studied by Raman scattering", E. Gallardo, S. Lazić, J.M. Calleja, F. Agulló-Rueda, J. Grandal, M.A. Sánchez-García and E. Calleja, **AIP Conf. Proc. 1199,** 325 (2010) - Proceedings of the 29th International Conference on the Physics of Semiconductors.
10. "Single photon emission and quantum ring-cavity coupling in InAs/GaAs quantum rings", E. Gallardo, L.J. Martínez, A.K. Nowak, D. Sarkar, D.Sanvitto, H.P. van der Meulen, J.M. Calleja, I. Prieto, A.R. Alija, D. Granados, A.G. Taboada and J.M. García, P.A. Postigo, **Journal of Physics:** Conference Series **210,** 012037 (2010) – Proceedings of the 11th International Conference on Optics of Excitons in Confined Systems.

## Other publications:

1. "Resonant Raman-active localized vibrational modes in $Al_yGa_{1-y}N_xAs_{1-x}$ alloys: Experiment and first-principles calculations", A. M. Teweldeberhan, G. Stenuit, S. Fahy, E. Gallardo, S. Lazić, J. M. Calleja, J. Miguel-Sánchez, M. Montes, A. Hierro, R. Gargallo-Caballero, A. Guzmán, and E. Muñoz, **Phys. Rev. B 77**, 155208 (2008).
2. "Resonant Raman study of local vibration modes in AlGaAsN layers", E. Gallardo, S. Lazić, J.M. Calleja, J. Miguel-Sánchez, M. Montes, A. Hierro, R. Gargallo-Caballero, A. Guzmán, E. Muñoz, A.M. Teweldeberhan and S. Fahy, **Physica E:** Low-Dimensional Systems and Nanostructures **40**, 2084-2086 (2008).
3. "Local vibration modes and nitrogen incorporation in AlGaAs:N layers", E. Gallardo, S. Lazić, J.M. Calleja, J. Miguel-Sánchez, M. Montes, A. Hierro, R. Gargallo-Caballero, A. Guzmán, E. Muñoz, A.M. Teweldeberhan and S. Fahy, **phys. stat. sol. (c) 5**, No. 6, 1562-1564 (2008).
4. "InN thermal effects in InP/(Ga,In)P quantum dot single-photon emitters", A. K. Nowak, E. Gallardo, D. Sarkar, H. P. van der Meulen, J. M. Calleja, J. M. Ripalda, L. González and Y. González, **Phys. Rev. B 80**, 161305(R) (2009).

5. "Old Silks Endowed with New Properties", G. R. Plaza, P. Corsini, E. Marsano, J. Pérez-Rigueiro, L. Biancotto, M. Elices, C. Riekel, F. Agulló-Rueda, E. Gallardo, J. M. Calleja and G. V. Guinea, **Macromolecules 42**, 8977 (2009).
6. "Temperature dependent single photon emission in InP/GaInP quantum dots", A. K. Nowak, E. Gallardo, D. Sarkar, D. Sanvitto, H. P. van der Meulen, J. M. Calleja, J. M. Ripalda, L. González and Y. González, **Physica E** (2010), doi:10.1016/j.physe.2010.02.025.